Implementation of the Lindbladian in Matrix Product States

Alexander Johannes de Bruyn

(5408490)

Thesis BSc Applied Mathematics &
BSc Applied Physics

Delft University of Technology
Delft, June 19, 2024

Supervisors:
Jos Thijssen (Applied Physics)
Neil Budko (Applied Mathematics)

Evaluation Committee:
Natalia Chepiga (Applied Physics)
Johan Dubbeldam (Applied Mathematics)

TU Delft

Abstract

In this thesis we implement the Lindblad equation in the matrix product state (MPS) formalism using an operator splitting method. We developed a second-order method based on a Trotter approximation and a third-order high-dimensional midpoint method and we proposed a new fourth-order method based on Duhamel's principle and a nested RK4 method, all of which preserve positivity and Hermiticity of the density operator. We simulated spin transport through an XXZ-Hamiltonian Heisenberg chain, for which we found the magnetisation profile and measured a spin current of 0.04-0.05. The results obtained are consistent with the existing literature. The extensive error analysis shows that the time step Δt is the main contributor to the error, if the bond dimension χ is set to at least 15. The third-order method is in general preferred to the second-order method, as only this method preserves trace. We also analysed the Hubbard model, including a spin orbit coupling, in order to propose a method for simulating the chiral induced spin selectivity (CISS) effect.

The codes used in this thesis can be found at `https://github.com/ajdebruyn/BEP`.

Table of Contents

1 Introduction

The chiral induced spin selectivity (CISS) effect is a fascinating and relatively recent discovery in the realm of quantum mechanics, where electron spin polarisation is achieved through the interaction with chiral molecules. This phenomenon has gained significant attention due to its potential applications in spintronics, quantum computing, and molecular electronics. Bloom et al. [4] have thoroughly reviewed the development of CISS and its applications.

CISS provides new insights into the interaction between electron spin and molecular chirality, or more specifically, the spin-orbit coupling in combination with quantum transport in chiral systems. It offers a mechanism for generating spin-polarised currents without the need for magnetic materials or external magnetic fields. This can lead to more efficient and compact spintronic devices, which are essential for next-generation data storage and data processing technologies. The ability to control electron spin states through chiral molecules could also contribute to the development of quantum bits (qubits) and quantum information processing, enhancing the performance of quantum computers. Many biomolecules, such as DNA and proteins, are chiral. Understanding CISS in these molecules could provide new insights into biological electron transfer processes, with potential implications for biochemistry, biophysics, and medicine.

Despite its promising potential, the theoretical understanding of the CISS effect involves complex many-body quantum interactions that require advanced methods for accurate modelling and simulation. Other studies have utilised numerous methods, such as perturbation theory [22], non-equilibrium Green's functions [47], tight-binding models [21], density functional theory [47], and Monte Carlo techniques [49]. In this thesis, we will propose a method that uses matrix product states (MPS) to simulate the CISS effect.

Matrix Product States (MPS's) have emerged as a powerful and versatile framework for the study of quantum many-body systems, particularly in low-dimensions. Originally developed in the context of the Density Matrix Renormalisation Group (DMRG) method, MPS has since also been known for their broader applicability in describing and simulating complex quantum states with high efficiency.

An MPS is particularly well-suited for representing quantum states in one-dimensional systems. It offers a compact and efficient representation by decomposing a large, entangled quantum state into a product of local tensors. Consequently, the MPS can capture the essential physics of a system with a manageable number of parameters, making them very efficient for numerical simulations. One of the key strengths of the MPS framework is its ability to accurately represent ground states and low-lying excited states of quantum systems, particularly those with short-range interactions. This capability makes the MPS a valuable tool in various fields, including condensed matter physics (where CISS is part of), quantum information theory, and statistical mechanics. Moreover, MPS algorithms have been developed for a range of applications, such as time evolution using time evolving

block decimation (TEBD) [70], finite-temperature simulations [67], and the study of open quantum systems [67].

Considering the CISS effect, we are faced with an open quantum system, since current flows through the molecule. Unlike closed quantum systems, which are isolated from any external influence, open quantum systems are more representative of practical scenarios where systems are subject to decoherence and dissipation due to interactions with external environments such as thermal baths, electromagnetic fields, or electron baths. The interactions with the environment can lead to an exchange of energy and information and cause the system to evolve in a non-unitary fashion, meaning the pure quantum states described by a wavefunction in closed systems must be generalised to mixed states described by a density operator, for which matrix product density operators (MPDO's) exist analogue to MPS. The dynamics of these mixed states provide a more accurate description of quantum systems in realistic settings.

To mathematically describe the time evolution of open quantum systems, we use the Lindblad equation, named after Göran Lindblad who derived it in 1976 [41], which provides a general framework for the time-evolution of the density operator of an open quantum system. This equation extends the Schrödinger equation to account for non-unitary processes, making it possible to model the effects of dissipation, which is necessary for e.g. the CISS effect. The Lindblad equation ensures the complete positivity and trace preservation of the density matrix, which is crucial for maintaining the physical structure of the quantum state over time.

In this thesis, we will focus on developing the Lindbladian time-operator for the vectorised MPDO (vMPDO), which has the same form as an MPS, and consider the implementation for the CISS effect. Earlier research regarding open systems and MPS has been conducted into, among other things, quantum trajectories [33][5], matrix product operators (MPO's) [13], locally purified tensor networks [33][71], diagonalisation methods [44], and quantum Monte Carlo approaches [76]. We will use operator splitting methods, conveniently utilising the locality of the operators. To our knowledge, this method is a new advance in this field, and the combination of MPS and the CISS effect has also not yet been studied before.

In chapter 2, we will explain the basics of quantum systems and lay the foundation for the rest of the thesis. We will focus on the density operator, spin chains, open quantum systems and the CISS effect. We will also introduce some numerical methods, including MPS, the main subject of chapter 3. In that chapter we will first discuss entanglement, introduce the Penrose graphical notation, and derive the MPS form. In the second half we will analyse the possible calculations with MPS, explore MPDO, introduce vectorisation (vMPDO) and discuss the time-evolution method TEBD. In chapter 4 we will look into numerical methods. We will discuss existing methods widely used for the density operator, focusing on operator splitting methods. For the second-order scheme, we use a Trotter approximation and for the fourth-order scheme, we use Duhamel's principle and Runge-Kutta 4, which could be swapped with another quadrature method for an even higher order scheme. In chapter 5, simulations for a Heisenberg chain will be carried out. We will analyse the results, including the magnetisation profile, current and trace. We are particularly interested in the non-equilibrium steady state of the system, because it provides information about the long term dynamics of the system. These dynamics are important when studying e.g. the CISS effect, or a spintronic device. There will also be a thorough error analysis, both for the stepsize and for the bond dimension, the truncation parameter of MPS. In the final chapter, chapter 6, a discussion of the obtained results and their implications for the research will be presented.

This thesis is written at the same time as Ates works on his thesis [1] for the degree of Master in Applied Physics at the TU Delft. In his work, Ates focuses on the CISS effect and implements the

results of this thesis regarding the dynamics of an open quantum system. We, in return, will make use of Ates' model to analyse the CISS effect.

2

Quantum Systems

This chapter reviews the foundational concepts of quantum mechanics, including the Schrödinger equation, density operator and quantum systems, both closed and open. We will introduce three numerical techniques to study these systems; density matrix renormalisation groups, matrix product states and quantum Monte Carlo. Finally, we will explain how the chiral induced spin selectivity effect fits into this framework.

2.1. Quantum Mechanics

This is only a short introduction to the subject. A more complete coverage can be found in the numerous textbooks on quantum mechanics, e.g. [48] or [25].

Schrödinger Equation

The *Schrödinger equation* [60] is the foundation of quantum mechanics: it describes the evolution of a wavefunction $|\psi\rangle$. The time-dependent Schrödinger equation is given by[1]

$$\mathrm{i}\frac{\partial|\psi\rangle}{\partial t} = \hat{H}|\psi\rangle\,, \tag{2.1}$$

where $\mathrm{i}^2 = -1$, $\hat{H}$ is the *Hamiltonian*, a Hermitian operator corresponding to the total energy of a system, and $|\phi\rangle$ is a vector in the *Hilbert space*. The time-independent Schrödinger equation is given by

$$\hat{H}|\psi\rangle = E|\psi\rangle\,, \tag{2.2}$$

where E is the energy of the system. Considering a time-independent Hamiltonian, the general solution to the time-dependent Schrödinger Equation is

$$|\psi(t)\rangle = e^{-\mathrm{i}t\hat{H}}|\psi(0)\rangle\,. \tag{2.3}$$

The Schrödinger equation is a linear differential equation, so a superposition of solutions is again a solution to the equation. Generalising this principle, we can choose to work in a basis of solutions to the time-independent Schrödinger equation, $\{|\psi_n\rangle\}$, to rewrite any wavefunction $|\psi\rangle$ as

$$|\psi\rangle = \sum_{n=1}^{\infty} c_n e^{-\mathrm{i}tE_n}|\psi_n\rangle\,. \tag{2.4}$$

[1] For convenience, we have taken the reduced Planck's constant equal to one in this thesis, i.e. $\hbar = 1$. Therefore, other literature might contain an extra factor $\hbar$ on the left side of 2.1.

The probability that a measurement of the energy yields E_n is equal to $|c_n|^2$. Note that in the case of a finite superposition, there exists a $N \in \mathbb{N}$, such that $c_n = 0$ for all $n > N$.

When considering electrons, or other particles, the so-called *spin* plays a crucial role in its dynamics.

Spin

Spin is an intrinsic form of angular momentum of elementary particles. Spin takes on integer and half-integer values; $s = 0, \frac{1}{2}, 1, \ldots$. The orientation of the spin along the z-axis ranges from $-s$ to s as $m_s = -s, -s+1, \ldots, s-1, s$, which is called the magnetic quantum number. The Higgs boson has spin 0, quarks and leptons, including electrons, have spin $\frac{1}{2}$, and photons, gluons and Z and W bosons have spin 1. In this thesis, we will focus on electrons, so spin $\frac{1}{2}$. For this spin, the magnetic quantum number m_s can be either $+\frac{1}{2}$ or $-\frac{1}{2}$, where $m_s = +\frac{1}{2}$ is associated with the spin-up state $|\uparrow\rangle$, and $m_s = -\frac{1}{2}$ with the spin-down state $|\downarrow\rangle$.

Spin is described by *spin operators*. Applying these operators to a quantum state gives information about the spin properties of the state. For spin $m_s = \frac{1}{2}$, the spin operators are represented using the *Pauli matrices*, which are defined as

$$\boldsymbol{\sigma}_x = \begin{pmatrix} 0 & 1 \\ 1 & 0 \end{pmatrix}, \qquad \boldsymbol{\sigma}_y = \begin{pmatrix} 0 & -\mathrm{i} \\ \mathrm{i} & 0 \end{pmatrix}, \qquad \boldsymbol{\sigma}_z = \begin{pmatrix} 1 & 0 \\ 0 & -1 \end{pmatrix}. \tag{2.5}$$

The spin operators $\hat{S}_x$, $\hat{S}_y$ and $\hat{S}_z$ are given by the Pauli matrices times $\frac{1}{2}$. All Pauli matrices, and thus also the spin operators, are Hermitian. The two eigenvalues of $\hat{S}_z$ are $\pm\frac{1}{2}$, corresponding to the eigenstates spin-up $|\uparrow\rangle$, and spin-down $|\downarrow\rangle$. In these two cases, the outcomes of the other two operators are undefined. The *ladder operators* $\boldsymbol{\sigma}_+$ and $\boldsymbol{\sigma}_-$ (or $\hat{S}_+$ and $\hat{S}_-$) raise and lower the spin eigenstates. They are given as

$$\boldsymbol{\sigma}_\pm = \tfrac{1}{2}\left(\boldsymbol{\sigma}_x \pm \mathrm{i}\boldsymbol{\sigma}_y\right), \qquad \boldsymbol{\sigma}_+ = \begin{pmatrix} 0 & 1 \\ 0 & 0 \end{pmatrix}, \qquad \boldsymbol{\sigma}_- = \begin{pmatrix} 0 & 0 \\ 1 & 0 \end{pmatrix}. \tag{2.6}$$

The raising operator $\boldsymbol{\sigma}_+$ raises the spin-down state $|\downarrow\rangle$ to spin-up $|\uparrow\rangle$, and, similarly, the lowering operator $\boldsymbol{\sigma}_-$ lowers the spin-up state $|\uparrow\rangle$ to spin-down $|\downarrow\rangle$.

The Pauli exclusion principle states that no two electrons can ever exist in the same state. This means that there are a maximum of two electrons per site. It is possible that such a fully occupied site costs more energy than if the two electrons occupied different sites, which would then be incorporated in the Hamiltonian as the *Coulomb interaction*.

Hilbert Space

The quantum states as described in this section are represented by vectors in a Hilbert space $\mathscr{H}$. The Hilbert space is a vector space with an inner product. Vectors in the Hilbert space are usually denoted by the *braket notation*; $|\psi\rangle$, with $|\psi\rangle^\dagger = \langle\psi|$. The inner product between two states is equal to $\langle\phi|\psi\rangle$. If $\{|\phi_j\rangle\}$ forms an orthonormal basis of $\mathscr{H}$, then any state $|\psi\rangle$ in $\mathscr{H}$ can be written as

$$|\psi\rangle = \sum_j c_j |\phi_j\rangle . \tag{2.7}$$

Note the similarity between this expression and (2.4). Again, $|c_j|^2$ denotes the probability to measure the state $|\psi_j\rangle$.

Suppose a system is divided into two parts, a and b. The Hilbert space of the total system $\mathscr{H}$ is then given by the *tensor product*, or *Kronecker product*, of the Hilbert spaces of a and b, $\mathscr{H} = \mathscr{H}_a \otimes \mathscr{H}_b$. The state $|\psi\rangle$ in the total system can be written as a Kronecker product of $|\alpha\rangle \in a$, and $|\beta\rangle \in b$, as

$$|\psi\rangle = |\alpha\rangle \otimes |\beta\rangle . \tag{2.8}$$

If an operator $\hat{A}$ acts on $|\alpha\rangle$ and $\hat{B}$ acts on $|\beta\rangle$, then

$$\left(\hat{A}\otimes\hat{B}\right)\left(|\alpha\rangle\otimes|\beta\rangle\right)=\hat{A}|\alpha\rangle\otimes\hat{B}|\beta\rangle\,. \tag{2.9}$$

The dimension of the total Hilbert space is equal to the product of the dimensions of the Hilbert spaces of the two parts. The dimension of the Hilbert space of particle with spin s is $d=2s+1$. Then the dimension of a spin chain (see section 2.3) containing L sites is equal to d^L, growing exponentially with the chain length.

2.2. Density Operator

The previous section summarised the quantum description of a closed system. The state of such a system is given by the wavefunction $|\psi\rangle$. Now we describe a quantum system in contact with an external environment, this is called an *open system*. We can obtain a description for this by first considering a closed universe U consisting of the system S and the environment E, where S and E are coupled, see figure 2.1. It is our aim to find a suitable description of the state in the non-closed system S. The influence of the environment E on the system S cannot be described by a single state of the system S itself, but only by a set of states $|\psi_j\rangle$, each with probability p_j ($\sum_j p_j=1$). For convenience, we will restrict ourselves to using orthonormal states. Considering the system only, and not the environment, its state can either be mixed or pure. A pure state is just a single vector $|\psi\rangle$, while a mixed state can be described by a set of vectors $\{|\psi_j\rangle\}$. The *density operator* [48] describes this non-isolated system, capturing the influence of the environment. The density operator is defined as

$$\hat{\rho}=\sum_j p_j\,|\psi_j\rangle\langle\psi_j|\,. \tag{2.10}$$

In the case of a pure state, this simplifies to $\hat{\rho}=|\psi\rangle\langle\psi|$. For such a pure state, it holds that $\hat{\rho}^2=|\psi\rangle\langle\psi|\psi\rangle\langle\psi|=|\psi\rangle\langle\psi|=\hat{\rho}$, which is not the case for a mixed state, since $\hat{\rho}^2=\sum_j p_j^2|\psi_j\rangle\langle\psi_j|\neq\hat{\rho}$. However, if one p_j were equal to 1 and the rest equal to 0, then the inequality would become an equality, resulting in a pure state as discussed above. The condition $\hat{\rho}^2=\hat{\rho}$ can be used to distinguish between the pure and mixed states.

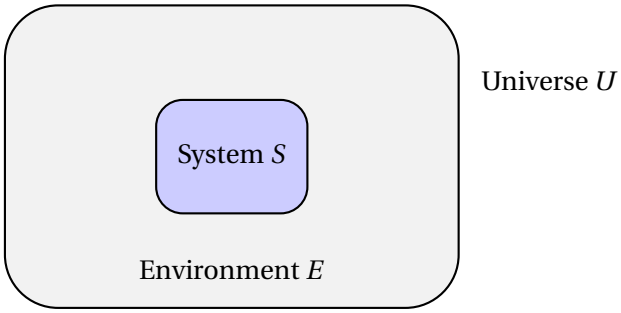

Figure 2.1: The universe U, consisting of the system S and its complement, the environment E.

We now introduce the *trace*, which gives the sum of the diagonal elements of an operator. The trace is defined as

$$\mathrm{Tr}\left(\hat{A}\right)=\sum_j\langle\chi_j|\,\hat{A}\,|\chi_j\rangle \tag{2.11}$$

where $\{\chi_j\}$ is a normalised basis of the system's Hilbert space. Note that the trace is a linear mapping, as $\mathrm{Tr}(p\hat{A}+q\hat{B})=p\mathrm{Tr}(\hat{A})+q\mathrm{Tr}(\hat{B})$. Other important properties are $\mathrm{Tr}(\hat{A}\hat{B})=\mathrm{Tr}(\hat{B}\hat{A})$ and $\mathrm{Tr}(|\chi\rangle\langle\phi|)=\langle\phi|\chi\rangle$. This can be used to show that the trace of $\hat{\rho}$ should be equal to one:

$$\mathrm{Tr}\left(\hat{\rho}\right)=\mathrm{Tr}\left(\sum_j p_j\,|\psi_j\rangle\langle\psi_j|\right)=\sum_j p_j\mathrm{Tr}\left(|\psi_j\rangle\langle\psi_j|\right)=\sum_j p_j\,\langle\psi_j|\psi_j\rangle=\sum_j p_j=1. \tag{2.12}$$

The *purity* is defined as $\gamma = \mathrm{Tr}(\hat{\rho}^2)$. For a pure state, we have $\gamma = \mathrm{Tr}(\hat{\rho}^2) = \mathrm{Tr}(\hat{\rho}) = 1$, and for a mixed state $\gamma = \mathrm{Tr}(\hat{\rho}^2) = \mathrm{Tr}\left(\sum_j p_j^2 |\psi_j\rangle\langle\psi_j|\right) = \sum_j p_j^2 \mathrm{Tr}\left(|\psi_j\rangle\langle\psi_j|\right) = \sum_j p_j^2 < 1$. The purity is thus a measure of the degree in which a state is mixed.

The expectation value of an operator $\hat{O}$ can be computed using the trace by

$$\langle\hat{O}\rangle = \sum_j p_j \langle\psi_j|\hat{O}|\psi_j\rangle = \mathrm{Tr}\left(\sum_j p_j |\psi_j\rangle\langle\psi_j|\hat{O}\right) = \mathrm{Tr}(\hat{\rho}\hat{O}). \tag{2.13}$$

Recall the universe U, system S and environment E from the start of this section. We want to arrive at the density operator $\hat{\rho}_S$ of the system S. For this purpose, the *partial trace* can be used to from the density operator of U, $\hat{\rho}^U$, which is given as $|\xi\rangle\langle\xi|$, as U is a closed system. Suppose that the normalised bases of S and E are $\{|\psi_j\rangle\}$ and $\{|\eta_j\rangle\}$, respectively. To calculate $\hat{\rho}^S$ for any $|\xi\rangle$ in U, the partial trace of $\hat{\rho}^U$ is taken over E:

$$\mathrm{Tr}_E\left(\hat{\rho}^U\right) = \sum_j \langle\eta_j|\hat{\rho}^U|\eta_j\rangle\,. \tag{2.14}$$

It can be shown that the density operator $\hat{\rho}$ is *Hermitian*, that is $\hat{\rho} = \hat{\rho}^\dagger$:

$$\hat{\rho}^\dagger = \left(\sum_j p_j |\psi_j\rangle\langle\psi_j|\right)^\dagger = \sum_j p_j \langle\psi_j|^\dagger |\psi_j\rangle^\dagger = \sum_j p_j |\psi_j\rangle\langle\psi_j| = \hat{\rho}. \tag{2.15}$$

The probability that a measurement of the system yields the state $|\phi\rangle$ is given by $\langle\phi|\hat{\rho}|\phi\rangle$. When working this out, we arrive at a restriction for the expectation value of $\hat{\rho}$:

$$\langle\phi|\hat{\rho}|\phi\rangle = \sum_j p_j \langle\phi|\psi_j\rangle\langle\psi_j|\phi\rangle = \sum_j p_j |\langle\phi|\psi_j\rangle|^2, \tag{2.16a}$$

$$0 \leq \sum_j p_j |\langle\phi|\psi_j\rangle|^2 \leq 1, \tag{2.16b}$$

$$0 \leq \langle\phi|\hat{\rho}|\phi\rangle \leq 1, \tag{2.16c}$$

for any $|\phi\rangle$. The positivity of all the terms in the sum in equation 2.16b results in the first inequality. The second inequality is a direct consequence of $\sum_j p_j = 1$ in combination with weights $|\langle\phi|\psi_j\rangle|^2$ being less than or equal to one. Finally, from equation 2.16c, we can conclude that the density operator $\hat{\rho}$ is *positive semi-definite*. In the following parts, this property will also be referred to as the *positivity* of $\hat{\rho}$.

In this subsection, we have come across the definition of the density operator $\hat{\rho}$, the (partial) trace, and three important properties of $\hat{\rho}$. These are

1. $\mathrm{Tr}\left(\hat{\rho}\right) = 1$,
2. $\hat{\rho}$ is Hermitian,
3. $\hat{\rho}$ is positive semi-definite.

2.3. Spin Chains

Originally designed for magnetic systems (see e.g. [28]), a *spin chain* is a one dimensional model to study interacting spins. The spins are aligned along a lattice, for example, a straight line or a spiral (see section 2.6). The interactions between the spins are described by the Hamiltonian, which is the sum of the individual operators acting on each spin or neighbouring spin-pair. We will discuss two different models, the *Heisenberg model* and the *Hubbard model*, and the *Jordan-Wigner transformation*, which couples the two models. Finally, we will treat helical chains and the *spin-orbit coupling*.

The Heisenberg model [28] consists of an interaction term between neighbouring spins and a term that represents an external magnetic field. The Hamiltonian of the standard Heisenberg model is given by

$$\hat{H} = J \sum_{i=1}^{L-1} \mathbf{S}_j \cdot \mathbf{S}_{j+1} - h \sum_{j=1}^{L} \mathbf{S}_j, \tag{2.17}$$

where $\mathbf{S}_j$ is the set of spin operators at site j, L is the length of the chain, J is the coupling constant, and h is the strength of the external magnetic field. The coupling constant J is not necessarily the same for $\hat{S}_j^X$, $\hat{S}_j^Y$, and $\hat{S}_j^Z$. For example, the XXZ-model has J_Z different from J_{XY} and is given by

$$\hat{H} = \sum_{j=1}^{L-1} \left[J_{XY} \left(\hat{S}_j^X \hat{S}_{j+1}^X + \hat{S}_j^Y \hat{S}_{j+1}^Y \right) + J_Z \hat{S}_j^Z \hat{S}_{j+1}^Z \right] - h \sum_{j=1}^{L} \hat{S}_j^Z, \tag{2.18}$$

where the external magnetic field is in the positive z-direction. The *anisotropy parameter* $\Delta = J_Z / J_{XY}$ determines the strength of the coupling constant along the z-direction relative to the x and y direction. When $\Delta = 1$, the XXZ-Heisenberg model reduces to the isotropic XXX Heisenberg model, where interactions are the same in all directions. The XXZ-Heisenberg Hamiltonian including the anisotropy parameter Δ becomes

$$\hat{H} = \sum_{j=1}^{L-1} J_{XY} \left(\hat{S}_j^X \hat{S}_{j+1}^X + \hat{S}_j^Y \hat{S}_{j+1}^Y + \Delta \hat{S}_j^Z \hat{S}_{j+1}^Z \right) - h \sum_{j=1}^{L} \hat{S}_j^Z. \tag{2.19}$$

Note that $\hat{S}_j$ and $\hat{S}_{j+1}$ act at two different sites. As discussed in section (2.1), we should take the Kronecker product between the two single-site operators to compute the two-site operator. Furthermore, for all other sites, we multiply by $\mathbb{I}$;

$$\mathbf{S}_j \mathbf{S}_{j+1} \rightarrow \left(\bigotimes_{\alpha=1}^{j-1} \mathbb{I} \right) \otimes \mathbf{S} \otimes \mathbf{S} \otimes \left(\bigotimes_{\alpha=j+2}^{L} \mathbb{I} \right), \tag{2.20a}$$

$$\mathbf{S}_j \rightarrow \left(\bigotimes_{\alpha=1}^{j-1} \mathbb{I} \right) \otimes \mathbf{S} \otimes \left(\bigotimes_{\alpha=j+1}^{L} \mathbb{I} \right). \tag{2.20b}$$

The linear Heisenberg model can be solved exactly by the *Bethe ansatz* [2] by constructing wavefunctions for magnons, solving the Bethe equations, and calculating the corresponding energy spectrum. An introduction to the Bethe ansatz can be found in [35] and [36].

The Hubbard model [31] is based on the *tight-binding model* and is used to describe the behaviour of interacting electrons in a lattice, such as a 1D chain. The model considers electrons moving through the chain, unlike the Heisenberg model, which considers a system of spins fixed at the lattice sites. The Hamiltonian of the Hubbard model consists of two terms: the hopping energy term and the Coulomb repulsion term. The hopping term describes the kinetic energy, and the Coulomb term represents the energy cost of having two electrons[2] on the same site. The Hamiltonian is given as

$$\hat{H} = -t \sum_{j=1}^{L-1} \sum_{\sigma} \left(\hat{c}_{j\sigma}^\dagger \hat{c}_{(j+1)\sigma} + \hat{c}_{(j+1)\sigma}^\dagger \hat{c}_{j\sigma} \right) + U \sum_{j=1}^{L} \hat{n}_{j\uparrow} \hat{n}_{j\downarrow}, \qquad \hat{n}_{j\sigma} = \hat{c}_{j\sigma}^\dagger \hat{c}_{j\sigma}, \tag{2.21}$$

where t is the hopping parameter, U the on-site Coulomb repulsion, $\hat{c}_{j\sigma}^\dagger$ the creation operator, $\hat{c}_{j\sigma}$ the annihilation operator, and $\hat{n}_{j\sigma}$ the number operator, for spin σ and site j. The combination $\hat{c}_{j\sigma}^\dagger \hat{c}_{(j+1)\sigma}$ creates an electron at site j and annihilates one at site j+1, effectively moving an electron one site down. The hermitian conjugate does the opposite and moves the electron one site up. See figure B.1 for a schematic overview of the application of the Hubbard Hamiltonian.

[2] Note that the two electrons need to have opposite spin. For details, see section 2.1.

The Jordan-Wigner transformation [34] is a method to map spin operators onto creation and annihilation operators. The transformation allows us to solve a Hubbard model by converting it to a Heisenberg model – it is given by

$$\sigma_j^+ = \exp\left(-\mathrm{i}\pi \sum_{k=1}^{j-1} \hat{c}_k^\dagger \hat{c}_k\right) \hat{c}_j^\dagger, \tag{2.22a}$$

$$\sigma_j^- = \exp\left(+\mathrm{i}\pi \sum_{k=1}^{j-1} \hat{c}_k^\dagger \hat{c}_k\right) \hat{c}_j, \tag{2.22b}$$

$$\sigma_j^z = 2\hat{c}_j^\dagger \hat{c}_j - 1. \tag{2.22c}$$

The exponential factor $\exp\left(\mathrm{i}\pi \sum_{k=1}^{j-1} \hat{c}_k^\dagger \hat{c}_k\right)$ ensures the correct anti-commutation relations for the creation and annihilation operators and commutation relations for the spin operators. There also exists an inverse transformation which maps the Heisenberg onto the Hubbard model, which is given by

$$\hat{c}_j^\dagger = \exp\left(+\mathrm{i}\pi \sum_{k=1}^{j-1} \sigma_k^+ \sigma_k^-\right) \sigma_j^+, \tag{2.23a}$$

$$\hat{c}_j = \exp\left(-\mathrm{i}\pi \sum_{k=1}^{j-1} \sigma_k^+ \sigma_k^-\right) \sigma_j^-. \tag{2.23b}$$

The Jordan-Wigner transformation makes it possible to solve some problem exactly, such as the XY-Hamiltonian. Other systems also benefit from this transformation, as it is in some cases easier to simulate a Hubbard model, when studying spin problems. Transforming spin Hamiltonians into equivalent fermionic Hamiltonians makes it possible to study spin systems using techniques developed for fermionic systems, and vice versa.

2.4. Numerical Methods for Many-Body Quantum Systems

The study of many-body quantum systems, such as the quantum chains in the previous section, poses significant computational challenges due to to the exponential growth of the total Hilbert space with the number of sites. As a result, solving the Schrödinger equation, and Lindblad equation, which we will discuss in the next section, exactly becomes infeasible for large systems. Numerical methods are necessary to approximate the behaviour of these systems. Among the various approaches, three are particularly interesting in this study for their effectiveness and applicability: *density matrix renormalisation group* (DMRG), *matrix product state* (MPS), and *quantum Monte Carlo* (QMC).

Density Matrix Renormalisation Groups

In 1992, White and Noack [72][73] designed DMRG as a model to determine the spectrum of the spin-zero ground state. It has since been extended and adapted for various complex many-body systems. The key idea behind DMRG is to iteratively optimise a reduced density matrix to find the ground state of the system. A thorough coverage of DMRG can be found in [64], [58] or [59].

Infinite DMRG is an approach designed for studying systems in the thermodynamic limit, where the system size is considered to be infinitely large. This method is particularly useful for exploring the bulk properties of systems without the influence of finite-size effects. Finite DMRG, which we will consider in this thesis, is designed for studying finite-size systems, where the focus is on accurately capturing the ground state properties and possibly the excited states of a system with specific boundary conditions. The finite DMRG algorithm proceeds through the following steps:

1. **Initialisation:** Start with a small system and divide it into two blocks: the system block and the environment block. Initially, these blocks may consist of a single site each. Calculate the wavefunction for this small system.

2. **Truncation:** Construct the reduced density matrix $\hat{\rho}_S$ for the system block by tracing out the degrees of freedom of the environment block. Retain the most significant eigenstates of $\hat{\rho}_S$, truncating the less significant ones to keep the computational cost manageable. Reduce the Hamiltonian of S to a smaller size using the significant eigenstates.

3. **Growth:** Iteratively grow the system block by adding one site at a time and perform step 2. Stop when the universe U has the desired length L.

4. **Sweep 1:** Start with S as the left half and E as the right half of U. Similarly to step 2, reduce the Hamiltonian of S. Transfer two sites from E to S. Repeat until E has size 3 or smaller.

5. **Sweep 2:** Now, perform a sweep where the role of the system and environment blocks is interchanged, i.e. reducing S and growing E. The matrices computed before are used for S. Stop when S has size 3 or smaller

6. **Iterations:** Continue sweeping back en forth until converge is achieved, i.e. until the ground state energy and wavefunction stabilise.

The infinite DMRG algorithm stays in step 3 resulting in infinite iterations. Step 4 through 6 appear only in the finite DMRG algorithm.

DMRG is particularly powerful for studying one-dimensional quantum systems, and typical applications of DMRG include spin chains, such as the Heisenberg and Ising model, and strongly correlated systems, such as the Hubbard model and other systems with strong electron-electron interactions. The method has high accuracy, efficiency and flexibility. By truncating the less significant components of the reduced density matrix, DMRG efficiently handles large system sizes that would not be feasible with exact diagonalisation methods. On top of that, the method can be adapted to different Hamiltonians and boundary conditions, making it versatile for different types of quantum systems. However, the efficiency decreases for 2D and higher dimensional systems, due to larger entanglement, and for obtaining excited states.

Matrix Product States

MPS's are a class of tensor network states that provide a compact representation of quantum states, especially for 1D systems, although similar methods, such as projected entangled pair states (PEPS) [65], exist for higher dimensions. The MPS framework naturally arises from the DMRG algorithm, which is essentially a method to variationally optimise the parameters of an MPS to find the ground state of a quantum system. Chapter 3 covers MPS and its applications, and detailed insights into MPS are also available in [50], [59] or [69]. In this section we cover the qualitative aspects of MPS and compare it to other methods, whereas in chapter 3 we will construct the MPS.

As its name suggests, an MPS expresses the wavefunction $|\psi\rangle$ of a quantum system as a product of matrices. For a 1D system with L sites, each basis state $|i_1 i_2 \dots i_L\rangle$ of the Hilbert space is associated with a corresponding matrix product:

$$|\psi\rangle = \sum_{i_1, i_2, \dots, i_L} \mathbf{A}^{(1)i_1} \mathbf{A}^{(2)i_2} \dots \mathbf{A}^{(L)i_L} |i_1 i_2 \dots i_L\rangle, \tag{2.24}$$

where $\mathbf{A}^{(k)i_k}$ are the matrices, and the indices i_k run over the local basis states at site k. In the case of a spin chain, these indices are the spins σ_k. The maximum allowed dimension of the matrices $\mathbf{A}^{(k)i_k}$ is referred to as the *bond dimension* χ, and it determines the level of entanglement that the

MPS can capture, i.e. its accuracy. Limiting the bond dimension allows for more efficient numerical calculations. Finding an optimal balance between efficiency and accuracy of MPS is very important.

Time-evolution of MPS is possible by implementing methods like *time-evolving block decimation* (TEBD), which will be discussed in section 3.5. TEBD applies a sequence of two-site Hamiltonian (section 2.3) or Lindbladian (section 2.5) time-operators to the MPS, followed by a singular value decomposition and truncation to restrict the matrix dimensions to the bond dimension χ.

MPS's provide insights into entanglement properties and can easily be implemented in e.g. Ising, Heisenberg and Hubbard models. MPS methods are highly versatile and provide an efficient representation of quantum states with limited entanglement, significantly reducing the computational cost required compared to a full Hilbert space of size d^L.

Similarly as to matrix product states, we can construct *matrix product operators*. However, each tensor in an MPO represents an operator instead of a state. MPO's are particularly useful for large Hamiltonians that do not consist of many two-site operators, and for density operators. They are widely used in numerical methods for simulating quantum systems, such as DMRG.

Quantum Monte Carlo

QMC refers to a family of stochastic methods that can provide accurate solutions for a variety of systems by using statistical sampling techniques. The primary idea is to represent the properties of the system using a set of random samples, which are then used to calculate the observables. There are several variants of QMC, each suited for different types of problems and conditions. The most prominent ones include variational Monte Carlo, diffusion Monte Carlo and path integral Monte Carlo. Thijssen [64] provides an in-depth analysis of these three methods.

Variational Monte Carlo [40][23] uses a trial wavefunction with variational parameters. According to the square of the wavefunction, it samples different configurations. The parameters are optimised by minimising the energy expectation value. *Diffusion Monte Carlo* [55] uses Green's function and can give exact results. The method projects out the ground state from an initial trial wavefunction by evolving the system in imaginary time. *Path integral Monte Carlo* [29] uses Feynman's path integral formulation to sample imaginary-time paths. The quantum partition function is represented as a sum over all possible paths, allowing for the calculation of finite-temperature properties.

Although each method has a slightly different approach, the general steps of a QMC simulation include:

1. **Initialisation:** Choose an initial set of configurations, often randomly or based on a trial wavefunction, and initialise the relevant parameters and distributions.

2. **Sampling:** Use Markov Chain Monte Carlo (MCMC) methods to generate a sequence of configurations.

3. **Measurement:** Compute physical observables by averaging over the sampled configurations and estimate errors.

4. **Optimisation:** Adjust the variational parameters to minimise the energy expectation value. Iterate steps 2, 3 and 4 until convergence.

QMC methods are even more versatile than DMRG and MPS. They can be applied to various quantum many-body problems, ranging from condensed matter physics, to quantum chemistry, and lattice problems like spin chains. QMC is also highly accurate, especially for ground state properties, sometimes even serving as a benchmark for other numerical methods.

For fermionic systems, QMC suffers from the *fermion sign problem*, where the cancellation of positive and negative contributions leads to an exponential growth in statistical error [42]. This limits

the applicability of QMC to fermionic systems at low temperatures and with large size. QMC methods are also computationally intensive, especially for large systems.

Each method – MPS, DMRG, and QMC – has distinct advantages and is best suited for specific types of problems. MPS and DMRG excel in 1D systems and offer deep insights into entanglement properties. QMC is highly versatile and powerful for a wide range of systems, including higher-dimensional systems, although it faces challenges like the fermion sign problem. That, and because QMC is less efficient, is the reason we choose to study MPS in this paper, while using DMRG to find the ground state of our system.

2.5. Lindblad Equation

An open quantum system is a quantum system that interacts with its external environment, as we already discussed in section 2.2. Unlike closed quantum systems, which are isolated and evolve according to the Schrödinger equation, open quantum systems exchange energy, particles, or information with their surroundings. This interaction leads to various phenomena, such as *decoherence* and *dissipation*. Although only the open quantum system S is the primary system of interest, and we do not know much about the behaviour outside of S, this system S is part of a larger universe U, which we have to take into account, see figure 2.1. The other part of the universe is the environment E, which consists of all external degrees of freedom interacting with the system.

The state of the open quantum system is described by the reduced density operator $\hat{\rho}_S$. Recall from (2.14) that $\hat{\rho}_S$ is obtained by tracing out the environmental degrees of freedom from $\hat{\rho}_U$. The reduced density operator provides a complete statistical description of the system's state and its time-evolution is therefore of particular interest to us. To determine the dynamics of S, we assume that the effect of the environment is *Markovian*, or local in time. The evolution of the system depends only on its current state, not on its history. When considering numerical methods, this assumption is allowed when the relaxation time of the environment is smaller than the time step of said numerical method.

The *Redfield equation* [54][7] is an equation used to describe the evolution of the reduced density matrix, where the interactions with the environment are weak. It is derived from the second-order perturbation theory in the system-environment coupling. The Hamiltonian we consider for the Redfield equation is $\hat{H}_U = \hat{H}_S + \hat{H}_E + \hat{H}_I$, where $\hat{H}_{U/S/E}$ is the Hamiltonian of $U/S/E$ and $\hat{H}_I$ is the interaction Hamiltonian. A second important assumption is the so-called Born approximation, which states that $\hat{\rho}_U$ can be written as $\hat{\rho}_S(t) \otimes \hat{\rho}_E$. A major limitation of the Born approximation is that it is only justified when there is no initial entanglement, i.e. the initial interaction between S and E is weak.

Recall that any wavefunction of a closed system satisfies (2.3). From this we directly find the time evolution of the density operator $\hat{\rho} = \sum_j p_j |\psi_j\rangle \langle\psi_j|$ of any system:

$$\hat{\rho}(t) = e^{-\mathrm{i}t\hat{H}} \hat{\rho}(0) e^{\mathrm{i}t\hat{H}}. \tag{2.25}$$

The time derivative of (2.25) yields the differential equation for $\hat{\rho}$, the *Von Neumann equation*,

$$\mathrm{i}\dot{\hat{\rho}}(t) = \left[\hat{H}, \hat{\rho}\right]. \tag{2.26}$$

The Redfield equation for the system S is obtained by tracing out the environment E from the von Neumann equation of the universe U. Finally, we apply the Markovian approximation, stating that $\hat{\rho}_S(\tau) \approx \hat{\rho}_S(t)$, to arrive at [7]

$$\frac{d\hat{\rho}_S}{dt} = -\int_0^t \mathrm{Tr}_E \left[\hat{H}_I(t), \left[\hat{H}_I(\tau), \hat{\rho}_S(t) \otimes \hat{\rho}_E\right]\right] d\tau. \tag{2.27}$$

The Redfield Equation is Markovian, but is not yet a master equation. We substitute $\tau = t - \tau$ in the integral in (2.27) and let the integral run from zero to infinity. This yields the *Born-Markov master equation* [6]:

$$\frac{d\hat{\rho}_S}{dt} = -\int_0^\infty \mathrm{Tr}_E\left[\hat{H}_I(t), \left[\hat{H}_I(t-\tau), \hat{\rho}_S(t)\otimes\hat{\rho}_E\right]\right] d\tau. \tag{2.28}$$

Thus, we see that in an open system S, there is an additional contribution arising from the unknown environment E. This contribution has to preserve the three requirements for a density operator (trace one, Hermitian, and positive semi-definite). Lindblad [41] showed that the only form possible for the additional contribution is given by the so-called *Lindblad equation*, which extends equation (2.26) with a *dissipation* $\mathscr{D}$ [6]:

$$\mathscr{D}\left[\hat{L}_i\right](\hat{\rho}) = \hat{L}_i\hat{\rho}\hat{L}_i^\dagger - \frac{1}{2}\left\{\hat{L}_i^\dagger\hat{L}_i, \hat{\rho}\right\}. \tag{2.29}$$

The time evolution of $\hat{\rho}$ is then given by the Lindblad equation:

$$\dot{\hat{\rho}} = \mathscr{L}(\hat{\rho}) = -\mathrm{i}\left[\hat{H}, \hat{\rho}\right] + \sum_i \gamma_i \mathscr{D}\left[\hat{L}_i\right](\hat{\rho}). \tag{2.30}$$

Here, $\{\hat{L}_i\}$ is the set of *Lindblad operators*. For a spin half-system we can define a basis of orthonormal operators $\{\hat{L}_i\}$ as

$$\left\{\tfrac{1}{\sqrt{2}}\mathbb{I}_2, \tfrac{1}{\sqrt{2}}\boldsymbol{\sigma}_X, \tfrac{1}{\sqrt{2}}\boldsymbol{\sigma}_Y, \tfrac{1}{\sqrt{2}}\boldsymbol{\sigma}_Z\right\} \tag{2.31}$$

or

$$\left\{\tfrac{1}{\sqrt{2}}\mathbb{I}_2, \boldsymbol{\sigma}_+, \boldsymbol{\sigma}_-, \tfrac{1}{\sqrt{2}}\boldsymbol{\sigma}_Z\right\}. \tag{2.32}$$

The factor γ_i is the *Lindblad decay rate* associated with each Lindblad operator $\hat{L}_i$. These decay rates quantify the strength of the interaction between the system and its environment, governing the rate at which the system loses coherence and energy to the environment. The Lindblad operators, along with their corresponding decay rates, describe the various dissipative processes experienced by the open quantum system. The Lindbladian $\mathscr{L}$ and dissipation $\mathscr{D}$ transform operators to operators and they are therefore called *superoperators*.

From the form of (2.30) and given that the dissipation superoperator is linear in $\hat{\rho}$, we see that the general solution to the Lindblad equation is

$$\hat{\rho}(t) = e^{t\mathscr{L}}\hat{\rho}(0). \tag{2.33}$$

We can use the Taylor series of the exponential to rewrite this expression in the following way, where we also define $\hat{\rho}(t) = \hat{\rho}_t$ and $\hat{\rho}(0) = \hat{\rho}_0$:

$$\hat{\rho}_t = \sum_{k=0}^{\infty} \frac{(t\mathscr{L})^k}{k!}\hat{\rho}_0, \tag{2.34}$$

where $\mathscr{L}^k(\hat{\rho}_0)$ denotes the result of applying $\mathscr{L}$ successively k times to $\hat{\rho}_0$.

It is important to note that the trace of $\mathscr{L}(\hat{\rho})$ vanishes:

$$\begin{aligned}\mathrm{Tr}\left(\mathscr{L}(\hat{\rho})\right) &= \mathrm{iTr}\left(\left[\hat{\rho}, \hat{H}\right]\right) + \sum_i \gamma_i \mathrm{Tr}\left(\mathscr{D}\left[\hat{L}_i\right](\hat{\rho})\right) \\ &= \mathrm{iTr}\left(\hat{\rho}\hat{H}\right) - \mathrm{iTr}\left(\hat{H}\hat{\rho}\right) + \sum_i \gamma_i \mathrm{Tr}\left(\hat{L}_i\hat{\rho}\hat{L}_i^\dagger\right) - \frac{1}{2}\mathrm{Tr}\left(\hat{L}_i^\dagger\hat{L}_i\hat{\rho}\right) - \frac{1}{2}\mathrm{Tr}\left(\hat{\rho}\hat{L}_i^\dagger\hat{L}_i\right) = 0\end{aligned} \tag{2.35}$$

The main subject of this research is to calculate the time evolution of $\hat{\rho}$ numerically. Essentially, it is almost impossible to further work out the expression (2.34) analytically. The individual terms in the sum of the dissipation do not commute, nor do the Hamiltonian and dissipation parts, so it is not possible to easily split the operator exponential. However, this is a very useful starting point to solve the Lindblad equation numerically. In chapter 4, we will look into different mathematical techniques to analyse the time evolution of the density operator accurately and efficiently.

2.6. Chiral Induced Spin Selectivity

Chiral molecules, characterised by their non-superimposable mirror images, exhibit interactions with electron spins due to their chiral structure and lack of inversion symmetry. This asymmetry leads to a spin-orbit coupling, causing a preferential orientation of spins during transport through these molecules. The CISS effect demonstrates that even in the absence of magnetic materials or external magnetic fields, significant spin polarisation can be achieved purely through molecular structure. In 1999, Ray et al. [53] discovered an asymmetry in photoelectron scattering of 10-20% for electron transport through an ordered film of chiral molecules, which was more than 100 times larger than what different studies before showed. In 2011, Göhler et al. [26] managed to find spin asymmetries exceeding 60%, and in 2020, Lu et al. [43] even demonstrated a spin-polarisation as high as 94%. Meanwhile, despite significant strides have been made in understanding and predicting aspects of CISS, physicists still struggle with the physical explanation of this phenomenon, as existent models can explain only a fraction of the experimental observations, except for some highly specific models.

The aim of this thesis is not to find the model that explains the CISS effect, but to determine a new approach to the problem, potentially more efficient and effective than existing models. For the CISS effect, we will implement a Hubbard model containing the spin-orbit coupling.

The *spin-orbit coupling* (SOC) is a fundamental interaction, arising from the interaction between the spin and momentum of an electron (or other particle). According to special relativity, the moving electron experiences an electric field as a magnetic field in its rest frame. This magnetic field interacts with the electron's spin, leading to an energy shift dependent on the spin orientation relative to the momentum of the electron. When an electron traverses a chiral molecule, intrinsic SOC causes asymmetric scattering depending on the spin orientation. This results in different transmission probabilities for spin-up and spin-down electrons, leading to spin-polarised currents. The efficiency of the spin polarisation is dependent on the SOC strength λ of the molecule. The SOC Hamiltonian can be expressed as

$$\hat{H}_{SOC} = \lambda \left(\mathbf{L}\cdot\mathbf{S}\right), \tag{2.36}$$

where $\mathbf{L}$ is the *orbital angular momentum*, and $\mathbf{S}$ is the spin operator. The orbital angular momentum is defined as the cross product of the position vector $\mathbf{r}$ and the momentum $\mathbf{p}$ of the electron: $\mathbf{L} = \mathbf{r}\times\mathbf{p}$. In a chiral molecule, this Hamiltonian term is of the type $\mathrm{i}\lambda\hat{c}_j^\dagger \mathbf{v}_j^{(k)}\cdot\boldsymbol{\sigma}\hat{c}_{j+2k}$, with $k=\pm1$, and at site j [20]. $\mathbf{v}_j^{(k)}$ characterises the chirality of the molecule and is given by $\hat{\mathbf{d}}_{j+k}\times\hat{\mathbf{d}}_{j+2k}$. The vector $\hat{\mathbf{d}}_{j+k} = \frac{\mathbf{r}_j-\mathbf{r}_{j+k}}{|\mathbf{r}_j-\mathbf{r}_{j+k}|}$ describes the direction of a link. The contribution of this specific SOC to the Hamiltonian is

$$\hat{H}_{SOC} = \lambda\sum_{j=0}^{L-2}\left(\mathrm{i}\hat{c}_j^\dagger \mathbf{v}_j^{(+1)}\cdot\boldsymbol{\sigma}\hat{c}_{j+2} + \mathrm{H.c.}\right), \tag{2.37}$$

In section 2.3, we discussed the general Hubbard model for a spin chain. The total Hubbard Hamiltonian including the SOC is now given as

$$\hat{H} = -t\sum_{j=1}^{L-1}\sum_{\sigma}\left(\hat{c}_{j\sigma}^\dagger\hat{c}_{(j+1)\sigma} + \hat{c}_{(j+1)\sigma}^\dagger\hat{c}_{j\sigma}\right) + U\sum_{j=1}^{L}\hat{n}_{j\uparrow}\hat{n}_{j\downarrow} + \lambda\sum_{j=0}^{L-2}\left(\mathrm{i}\hat{c}_j^\dagger\mathbf{v}_j^{(+1)}\cdot\boldsymbol{\sigma}\hat{c}_{j+2} + \mathrm{H.c.}\right). \tag{2.38}$$

See figure B.2 for a schematic overview of the application of this Hamiltonian. The Lindblad equation does not change for the inclusion of the SO coupling. Therefore, when further studying the time-evolution of the Lindbladian, we will not have to focus on or incorporate the SOC. At the end, we can easily insert the Hubbard SOC Hamiltonian into our model, to analyse the CISS effect. For this reason, we will not go further into the details of the CISS effect and the SOC. For readers interested in the CISS effect we recommend references [4], [19] and [52], and for readers interested in the spin-orbit coupling we recommend references [20] and [75].

3

Matrix Product States

This chapter is dedicated to determining the matrix product state of a wavefunction, exploring its applications, extending the method to density operators, and explaining how to apply time evolving block decimation, but first, let us start with an introduction into the subject.

3.1. Entanglement, Schmidt Decomposition and Area Law

Consider again a universe U, consisting of the system S and the environment E, see figure 2.1. The Hilbert space of the universe $\mathscr{H}_U$ is described by the Kronecker product of the Hilbert spaces of the two subspaces S and E; $\mathscr{H}_U = \mathscr{H}_S \bigotimes \mathscr{H}_E$. The states in U may be *entangled*, which means that the system S cannot be described independently of the environment, and thus it is not a pure state. In an entangled state, the properties of one particle are intrinsically linked to the properties of another particle, regardless of the distance between them. Note that entanglement goes beyond classical correlations and exhibits non-local properties.

For example, The state $|\phi\rangle = |00\rangle + |11\rangle$ represents a maximally entangled state of two qubits, both of which can exist in a superposition of $|0\rangle$ and $|1\rangle$ simultaneously. The state $|\phi\rangle$ is a superposition of two basis states; Either both qubits are in the state $|0\rangle$ or they are both in the state $|1\rangle$. These states are entangled because they cannot be expressed as a product of individual qubit states. The properties of one qubit are intrinsically linked to the properties of the other qubit, since if we measure the first qubit to be in the state $|0\rangle$, we instantly know that the second qubit will also be in the state $|0\rangle$, and vice versa.

Thus, for an entangled state it is no longer possible to write the wavefunction $|\psi\rangle$ in $\mathscr{H}_U$ as in (2.8). The entangled wavefunction can only be described by the so-called *Schmidt decomposition*:

$$|\psi\rangle = \sum_{i=1}^{N} \Lambda_i |\alpha_i\rangle \otimes |\beta_i\rangle , \tag{3.1}$$

where the Schmidt states $\{|\alpha_i\rangle\}$ and $\{|\beta_i\rangle\}$ are orthonormal states in $\mathscr{H}_S$ and $\mathscr{H}_E$, respectively. The non-negative values Λ_i are called the Schmidt values. The integer value N can range from 1 up to $N_{max} = \min(\dim S, \dim E)$. When $N = 1$, we can write the wavefunction as $|\psi\rangle = |\alpha\rangle \otimes |\beta\rangle$, and thus the state is not entangled. For maximal N, there is also maximal entanglement.

In section 2.2, the density operator $\hat{\rho} = \sum_j p_j |\psi_j\rangle \langle\psi_j|$ was discussed. This density matrix, combined with equation 3.1, can be used to compute the *entanglement entropy*, or *Von Neumann entropy*

$$\mathscr{S} = -\mathrm{Tr}(\hat{\rho} \ln \hat{\rho}) = -\sum_{i=1}^{N} \Lambda_i^2 \ln \Lambda_i^2 . \tag{3.2}$$

Now, when there is no entanglement ($N = 1$), $\Lambda_1 = 1$ and $\mathscr{S} = 0$, while for maximal entanglement, every $\Lambda_i = 1/\sqrt{N_{max}}$ and the Von Neumann entropy is equal to $\ln N_{max}$.

Typically, for general states in $\mathscr{H}_U$, just as for classical mechanics, the entropy scales with the volume of the system. However, it appears that for systems with a local, gapped Hamiltonian, this does not hold. In these systems, the ground state and low-energy excitations have correlations that decay rapidly with distance. Therefore, the entanglement between a system and its environment is primarily due to the degrees of freedom at the boundary of the region, rather than those deep inside it. This (see section 2.3) implies that the associated states close to the ground state do not follow a volume law, but rather an *area law* [18][27]. Thus, the entanglement entropy $\mathscr{S}_S$ of the system S is given as

$$\mathscr{S}_S \propto |\partial S|, \tag{3.3}$$

where $|\partial S|$ is the "area" of S. For a one-dimensional system, e.g. a spin chain, the entanglement entropy is constant, and independent of the length of the system.

The total Hilbert space consists predominantly of states that follow the volume law, and only a minor part that follows the area law. Finding the low-energy eigenstates numerically becomes much more efficient, as we can eliminate the largest part of the total Hilbert space. DMRG exploits this reduced subspace by iteratively optimising over states with limited entanglement. This makes them highly effective, especially for finding ground states of 1D systems. On top of that, MPS, which is the main topic of this chapter, also takes advantage of this principle, as low entanglement causes the Schmidt values to decrease rapidly in many systems. By truncating the Schmidt values, one can approximate the original state with a lower-rank state, leading to compression and efficient representation of quantum states. Recall, the original Hilbert space has dimension d^L, which for large L becomes too large to simulate the entire system.

The *singular value decomposition* (SVD) plays a crucial role in the efficient representation of quantum states regarding MPS. The SVD is a mathematical technique that factorises a given matrix $\mathbf{A}$ into three matrices:

$$\mathbf{A} = \mathbf{U}\mathbf{\Sigma}\mathbf{V}^\dagger, \tag{3.4}$$

where $\mathbf{U}$ and $\mathbf{V}$ are complex unitary matrices, and $\mathbf{\Sigma}$ is a rectangular diagonal matrix with the singular values on the diagonal. The singular values are real and non-negative. This factorisation is possible for all matrices $\mathbf{A}$. Often, to keep the MPS representation efficient, we truncate the small singular values in $\mathbf{\Sigma}$. The Schmidt decomposition and the SVD are inherently linked, as Schmidt values are the same as the singular values.

3.2. Matrix Product States

Before diving into the MPS representation, we should explain the widely used graphical notation first. The *tensor graphical notation*, or *Penrose graphical notation*, introduced by Penrose in 1971 [51], is a visual representation of (multi-)linear tensor networks, in which blocks are linked by lines. The boxes represent the tensors and the L lines connected to a box represent the L indices of the corresponding tensor. Contracting two tensors over one of their indices is visualised by connecting two lines of the corresponding boxes. An example considering matrices and vectors is visualised below[1].

[1] This and following figures in this chapter are from [63], and are reprinted with permission

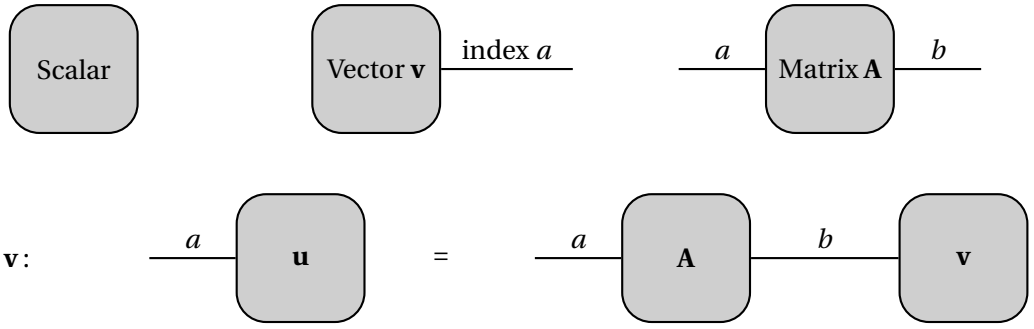

Tensors of higher order, e.g. the quantum state of a spin chain, are represented as

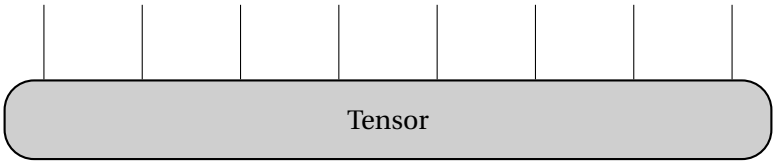

where this particular tensor is of order 8. Note that the number of unconnected indices denotes the order of a tensor; connecting all indices yields a constant. Now that we have explained the Penrose graphical notation, we can start exploring MPS.

In section 2.3 quantum chains were explained. Consider such a one-dimensional chain consisting of L sites, where on each site $j \in \{1,2,...,L\}$ there are d possible states $|\sigma_j\rangle$. Then any state of the system (in this case we define the chain as the system, as defined in section 2.2) can be described by

$$|\psi\rangle = \sum_{\sigma_1,...,\sigma_L} c_{\sigma_1...\sigma_L} |\sigma_1\sigma_2\cdots\sigma_L\rangle\,, \tag{3.5}$$

where, using the orthonormality of the states $|\sigma_j\rangle$, the coefficients $c_{\sigma_1...\sigma_L}$ can be found as

$$c_{\sigma_1...\sigma_L} = \langle\sigma_1\sigma_2...\sigma_L|\psi\rangle\,. \tag{3.6}$$

The concept of matrix product states is, as the name might already suggest, to write $c_{\sigma_1\cdots\sigma_L}$ as a product of matrices:

$$c_{\sigma_1...\sigma_L} = \prod_j \mathbf{A}^{[j]\sigma_j}, \tag{3.7}$$

where the first and last matrix, $\mathbf{A}^{[1]\sigma_1}$ and $\mathbf{A}^{[L]\sigma_L}$, are a row and column vector, respectively. The size of the matrices in the bulk are determined by the size of the neighbouring matrices. The size of a matrix increases or decreases by a factor of d, compared to the neighbouring matrix. The matrices in the bulk can therefore rapidly grow in size – up to $d^{L/2}$ in the middle –, which is highly undesirable. This is where a crucial element of MPS comes into play; we limit the number of rows and columns of the matrices to χ, the *bond dimension*, hoping that this preserves the three properties of $\hat{\rho}$. There are dL matrices, each of size at most $\chi \times \chi$. The resulting memory requirement cost is $\mathcal{O}\left(dL\chi^2\right)$, which can be much smaller than the original d^L, especially for large chains.

In the case $L = 8$, we can visualise these matrices as

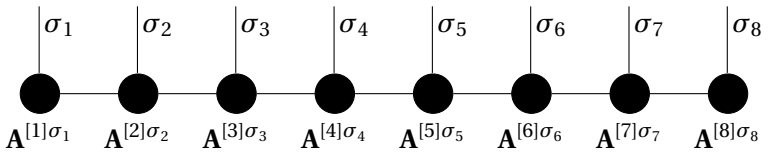

where each matrix is represented by a black dot and has a leg pointing upward, corresponding to the possible states at that site. The matrices are connected to their nearest neighbours, which represents a contraction over the so-called *bond indices*. It is also possible to construct MPS for periodic boundary conditions [16][68]. Then we should connect the first and last matrix via a horizontal leg as well. In this thesis, however, we will focus on 'open' chains.

Now, we will show how we can find the matrices $\mathbf{A}^{[j]\sigma_j}$. Details can be found in [59] or [50] – here we restrict ourselves to a brief description. The sizes of the matrices in the following part are not yet limited to the bond dimension χ described above. We will first derive the matrices and then after that, we will apply the bond dimension.

First, we view the coefficients $c_{\sigma_1\ldots\sigma_L}$ as elements of the matrix $\mathbf{C}$ of size $1 \times d^L$. $\mathbf{C}$ can be reshaped as a matrix of size $d \times d^{L-1}$, to which we can apply the singular value decomposition:

$$c_{\sigma_1\ldots\sigma_L} = C_{\sigma_1,(\sigma_2\ldots\sigma_L)} = \sum_{a_1} U_{\sigma_1,a_1}\Lambda_{a_1,a_1}V^{\dagger}_{a_1,(\sigma_2\ldots\sigma_L)}. \tag{3.8}$$

The element $C_{\sigma_1,(\sigma_2\ldots\sigma_L)}$ has two indices; σ_1 and $(\sigma_2\ldots\sigma_L)$. The bond index a_1 is a number that is equal to the maximum number of singular values of the decomposition and is equal to the smallest dimension of $\mathbf{C}$; in this case d. The maximum size of $\mathbf{U}$ is $d \times d$, but it can be smaller if some singular values are zero. Considering the desired result, equation 3.7, we define $U_{a_1,\sigma_1} = A^{\sigma_1}_{a_1}$ and $\Lambda_{a_1,a_1}V^{\dagger}_{a_1,(\sigma_2\ldots\sigma_L)} = C_{(a_1\sigma_2),(\sigma_3\ldots\sigma_L)}$, of size $d^2 \times d^{L-2}$. A second singular value decomposition, carried out in the same way as before, gives

$$c_{\sigma_1\ldots\sigma_L} = \sum_{a_1} A^{\sigma_1}_{a_1} C_{(a_1\sigma_2),(\sigma_3\ldots\sigma_L)} \tag{3.9a}$$

$$= \sum_{a_1,a_2} A^{\sigma_1}_{a_1} U_{(\sigma_2 a_1),a_2}\Lambda_{a_2,a_2}V^{\dagger}_{a_2,(\sigma_3\ldots\sigma_L)} \tag{3.9b}$$

$$= \sum_{a_1,a_2} A^{\sigma_1}_{a_1} A^{\sigma_2}_{a_1,a_2} C_{(a_2\sigma_3),(\sigma_4\ldots\sigma_L)}, \tag{3.9c}$$

where the last substitution (3.9c) is similar to the one carried out in the first step (3.9a). The maximum size of $A^{\sigma_2}_{a_1 a_2}$ is $d \times d^2$. Repeating this process would finally give

$$c_{\sigma_1\ldots\sigma_L} = \sum_{a_1,\ldots,a_{L-1}} A^{\sigma_1}_{a_1} A^{\sigma_2}_{a_1,a_2}\cdots A^{\sigma_{L-1}}_{a_{L-2},a_{L-1}} A^{\sigma_L}_{a_{L-1}}. \tag{3.10}$$

Finally, we substitute (3.10) back into (3.5) to find the MPS representation of $|\psi\rangle$ to be

$$|\psi\rangle = \sum_{\sigma_1,\ldots,\sigma_L}\sum_{a_1,\ldots,a_{L-1}} A^{\sigma_1}_{a_1} A^{\sigma_2}_{a_1,a_2}\cdots A^{\sigma_{L-1}}_{a_{L-2},a_{L-1}} A^{\sigma_L}_{a_{L-1}} |\sigma_1\sigma_2\cdots\sigma_L\rangle, \tag{3.11}$$

Again, for the case $L = 8$, the visual representation of the construction of the MPS according to the description above, will be as follows:

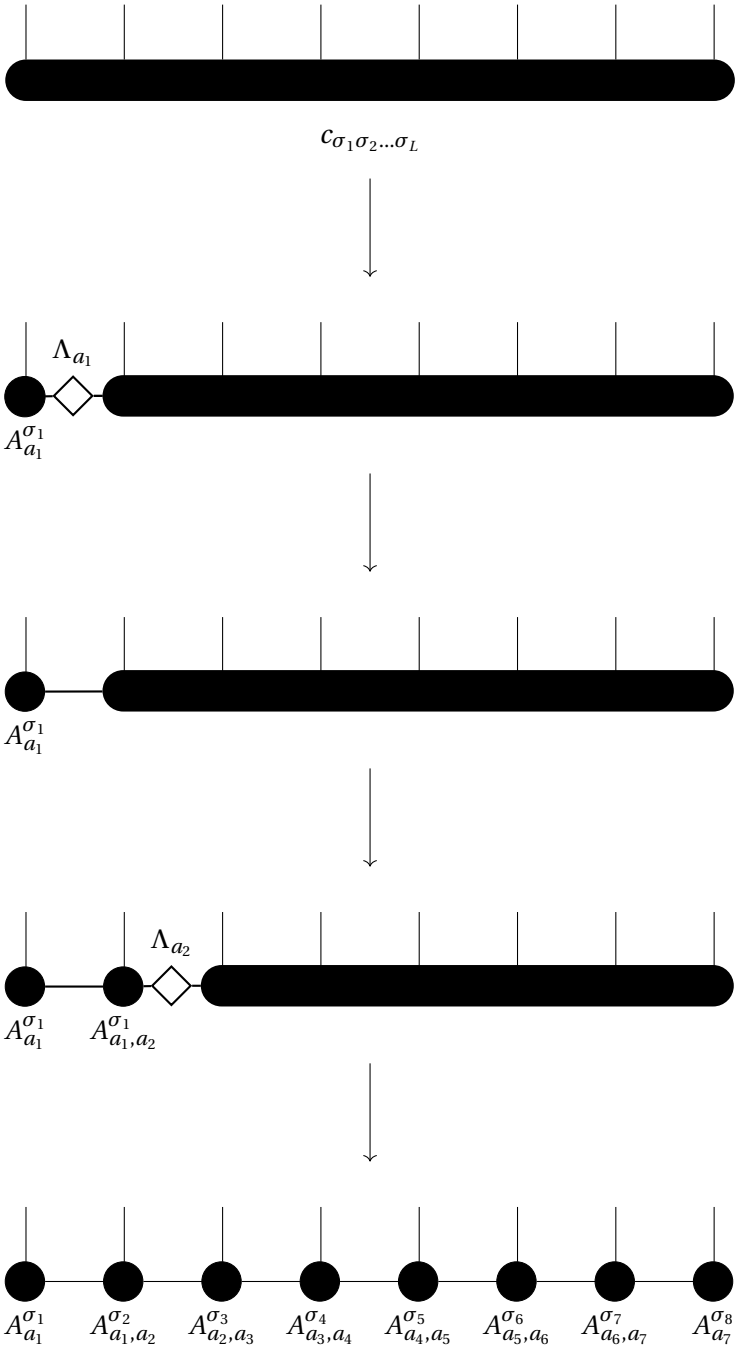

It can be seen that alternately, a singular value decomposition is applied and then the matrix Λ is absorbed in the right part. The vertical lines represent the indices σ_j and the horizontal lines the bond indices a_j. The bond indices will be bounded by the bond dimension χ in order to limit the numbers needed.

In some cases it might be favourable to leave the $\mathbf{\Lambda}$'s in the expression. Inserting unit matrices $\mathbb{I} = \mathbf{\Lambda}\mathbf{\Lambda}^{-1}$ between each pair in equation 3.10 makes it possible to restore them. The $\mathbf{\Lambda}^{-1}$'s are then absorbed by the $\mathbf{A}$'s and we call these new matrices $\mathbf{\Gamma}$:

$$c_{\sigma_1\ldots\sigma_L} = \sum_{a_1,\ldots,a_{L-1}} \Gamma^{\sigma_1}_{a_1}\Lambda_{a_1}\Gamma^{\sigma_2}_{a_1,a_2}\Lambda_{a_2}\Gamma^{\sigma_3}_{a_2,a_3}\cdots\Lambda_{a_{L-1}}\Gamma^{\sigma_L}_{a_{L-1}}. \tag{3.12}$$

This representation is called the *canonical form* [70]. Λ_{a_j,a_j} is replaced by Λ_{a_j} for convenience.

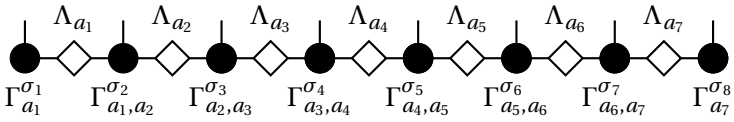

We discussed before that without restricting the bond indices, the dimensions of the matrices could increase up to $d^{L/2}$ halfway in the chain. The total number of matrix elements would then be larger than d^L, especially for long chains. Limiting the size of the matrices by the bond dimension χ is essential to make this work. Limiting the size is essentially the same as cutting of Λ_j after χ values, but it is only possible to omit these other values if they are sufficiently small. For a gapped system, these values do indeed decrease quickly. However, for non-gapped systems, e.g. Heisenberg chains, the values decrease significantly slower. It is possible to determine χ based on the values of Λ_j, but it might be simpler to state χ beforehand and check if it works. The truncation error caused by omitting values of Λ_j is [66]

$$\left||\psi\rangle - |\psi_{\text{trunc}}\rangle\right|^2 \leq 2\sum_{j=1}^{L-1}\epsilon_j(\chi) = 2\sum_{j=1}^{L-1}\sum_{i=\chi+1}^{N_j}\lambda_i^{[j]}, \tag{3.13}$$

where $\lambda_i^{[j]}$ is the i'th diagonal value of Λ_{a_j} at link j, and N_j is the size of Λ^{σ_j}. $\epsilon_j(\chi)$ is the sum of the omitted values at link j.

U_{a_1,σ_1}, and subsequently $A^{\sigma_1}_{a_1}$, are obtained using the singular value decomposition, so its column vectors are orthonormal, implying that

$$\sum_{a_1,\sigma_2}\left(A^{\sigma_2}\right)^\dagger_{a_2',a_1} A^{\sigma_2}_{a_1,a_2} = \delta_{a_2,a_2'}. \tag{3.14}$$

This can be generalised for each site j:

$$\sum_{\sigma_j}\mathbf{A}^{\sigma_j\dagger}\mathbf{A}^{\sigma_j} = \mathbb{I}. \tag{3.15}$$

This property is called *left normalisation* and it ensures that the states spanned by the MPS are orthonormal. This is crucial for many numerical algorithms, such as the Density Matrix Renormalisation Group (DMRG) and variational optimisation methods, as it simplifies the computations and improves numerical stability. If we were to construct the MPS starting at the right, then we would have *right normalisation*:

$$\sum_{\sigma_j}\mathbf{A}^{\sigma_j}\mathbf{A}^{\sigma_j\dagger} = \mathbb{I}. \tag{3.16}$$

If all matrices to the left (or right) of $\mathbf{A}^{\sigma_j}$ are left (or right) normalised, than the basis on that side of $\mathbf{A}^{\sigma_j}$ is orthonormal. In general, it is not possible that each matrix $\mathbf{A}^{\sigma_j}$ is both left and right normalised, which we aim for. However, there exist methods to transform an MPS to this form, including the SVD [45].

Instead of running over all sites at once as in (3.15) or (3.16), we can also choose to only continue up to a certain site j. The left normalisation principle implies that we can write the states on the j leftmost sites as

$$\begin{aligned}|\alpha_{a_j}\rangle &= \sum_{\sigma_1,\ldots,\sigma_j}\sum_{a_1,\ldots,a_j} A^{\sigma_1}_{a_1}A^{\sigma_2}_{a_1,a_2}\cdots A^{\sigma_j}_{a_{j-1},a_j}|\sigma_1\sigma_2\cdots\sigma_j\rangle \\ &= \sum_{\sigma_1,\ldots,\sigma_j}\sum_{a_1,\ldots,a_j}\Gamma^{\sigma_1}_{a_1}\Lambda_{a_1}\Gamma^{\sigma_2}_{a_1,a_2}\Lambda_{a_2}\Gamma^{\sigma_3}_{a_2,a_3}\cdots\Lambda_{a_{j-1}}\Gamma^{\sigma_j}_{a_{j-1},a_j}|\sigma_1\sigma_2\cdots\sigma_j\rangle,\end{aligned} \tag{3.17}$$

all of which are orthonormal. In the same way, it is possible to construct matrices $\mathbf{B}^{\sigma_i}$, starting at the right and working towards site $j+1$:

$$\begin{aligned}|\beta_{a_j}\rangle &= \sum_{\sigma_{j+1},\ldots,\sigma_L}\sum_{a_{j+1},\ldots,a_L} B^{\sigma_{j+1}}_{a_j,a_{j+1}}B^{\sigma_{j+2}}_{a_{j+1},a_{j+2}}\cdots B^{\sigma_L}_{a_{L-1}}|\sigma_{j+1}\sigma_{j+2}\cdots\sigma_L\rangle \\ &= \sum_{\sigma_{j+1},\ldots,\sigma_L}\sum_{a_{j+1},\ldots,a_L}\Gamma^{\sigma_{j+1}}_{a_j,a_{j+1}}\Lambda_{a_{j+1}}\Gamma^{\sigma_{j+2}}_{a_{j+1},a_{j+2}}\Lambda_{a_{j+2}}\Gamma^{\sigma_{j+3}}_{a_{j+2},a_{j+3}}\cdots\Lambda_{a_{L-1}}\Gamma^{\sigma_L}_{a_{L-1}}|\sigma_{j+1}\sigma_{j+2}\cdots\sigma_L\rangle.\end{aligned} \tag{3.18}$$

Combining the expressions for $|\alpha_{a_j}\rangle$ and $|\beta_{a_j}\rangle$, allows us to write $|\psi\rangle$ as

$$\begin{aligned}|\psi\rangle &= \sum_{\sigma_1,\ldots,\sigma_L}\sum_{a_1,\ldots,a_L}\Gamma^{\sigma_1}_{a_1}\Lambda_{a_1}\ldots\Lambda_{a_{j-1}}\Gamma^{\sigma_j}_{a_{j-1}a_j}\Lambda_{a_j}\Gamma^{\sigma_{j+1}}_{a_j a_{j+1}}\Lambda_{a_{j+1}}\ldots\Lambda_{a_{L-1}}\Gamma^{\sigma_L}_{a_{L-1}}|\sigma_1\sigma_2\cdots\sigma_L\rangle \\ &= \sum_{a_j}\Lambda_{a_j}|\alpha_{a_j}\rangle\otimes|\beta_{a_j}\rangle,\end{aligned} \tag{3.19}$$

which can be visualised as

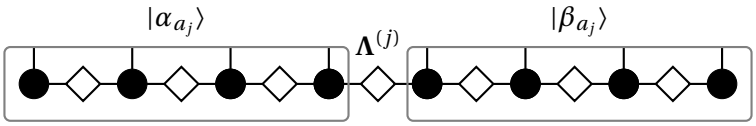

This is an important result, because it shows that for all j, $|\psi\rangle$ can be written as a product of a 'left' state and a 'right' state regarding site j. This form is essentially a Schmidt decomposition.

In this section, we have discussed how we can construct MPS in different forms and how this reduces the memory cost from $\mathcal{O}(d^L)$ to $\mathcal{O}(dL\chi^2)$. In the next section we will apply these expressions to problems involving operators.

3.3. Calculations with Matrix Product States

The expectation value of an operator $\hat{O}$ is given by $\langle\psi|\hat{O}|\psi\rangle$. The expectation value of a local operator acting on a single site $\hat{O}_j$ can then be computed as

$$\begin{aligned}\langle\psi|\hat{O}_j|\psi\rangle &= \sum_{\sigma_j,\sigma'_j}\sum_{\substack{a_{j-1},a_j,\\ a'_{j-1},a'_j}}\Lambda^\dagger_{a'_{j-1}}\Lambda_{a_{j-1}}\left(\Gamma^{\sigma_j}_{a_{j-1},a_j}\right)^\dagger\Gamma^{\sigma'_j}_{a_{j-1},a_j}\Lambda^\dagger_{a'_j}\Lambda_{a_j}\langle\alpha_{a'_{j-1}}|\alpha_{a_{j-1}}\rangle\langle\sigma_j|\hat{O}_j|\sigma'_j\rangle\langle\beta_{a'_j}|\beta_{a_j}\rangle \\ &= \sum_{\sigma_j,\sigma'_j}\sum_{a_{j-1},a_j}\left|\Lambda_{a_{j-1}}\right|^2\left(\Gamma^{\sigma_j}_{a_{j-1},a_j}\right)^\dagger\Gamma^{\sigma'_j}_{a_{j-1},a_j}\left|\Lambda_{a_j}\right|^2\langle\sigma_j|\hat{O}_j|\sigma'_j\rangle,\end{aligned} \tag{3.20}$$

where in the second equality we used the orthonormality of $|\alpha_{a_i}\rangle$ and $|\beta_{a_i}\rangle$. The second sum runs only over a_{j-1} and a_j, and not over all a_i, which is efficient as it only takes a CPU time scaling as $\mathcal{O}\left(d^2\chi^2\right)$.

Now we calculate matrix elements of a nearest neighbour two-site operator $\hat{O}_{j,j+1}$.
We first introduce the tensor $\Theta^{\sigma_j,\sigma_{j+1}}_{a_{j-1},a_{j+1}}$ as

$$\Theta^{\sigma_j,\sigma_{j+1}}_{a_{j-1},a_{j+1}} = \sum_{a_j}\Lambda_{a_{j-1}}\Gamma^{\sigma_j}_{a_{j-1},a_j}\Lambda_{a_j}\Gamma^{\sigma_j}_{a_j,a_{j+1}}\Lambda_{a_{j+1}}, \tag{3.21}$$

enabling us to write $|\psi\rangle$ more compactly as

$$\begin{aligned}|\psi\rangle &= \sum_{\sigma_j,\sigma_{j+1}}\sum_{a_{j-1},a_j,a_{j+1}}\Lambda_{a_{j-1}}\Gamma^{\sigma_j}_{a_{j-1},a_j}\Lambda_{a_j}\Gamma^{\sigma_j}_{a_j,a_{j+1}}\Lambda_{a_{j+1}}|\alpha_{a_{j-1}}\rangle|\sigma_j\sigma_{j+1}\rangle|\beta_{a_{j+1}}\rangle \\ &= \sum_{\sigma_j,\sigma_{j+1}}\sum_{a_{j-1},a_{j+1}}\Theta^{\sigma_j,\sigma_{j+1}}_{a_{j-1},a_{j+1}}|\alpha_{a_{j-1}}\rangle|\sigma_j\sigma_{j+1}\rangle|\beta_{a_{j+1}}\rangle.\end{aligned} \tag{3.22}$$

This $\Theta^{\sigma_j,\sigma_{j+1}}_{a_{j-1},a_{j+1}}$ now represents the two sites j and $j+1$ on which $\hat{O}_{j,j+1}$ is acting. Letting $\hat{O}_{j,j+1}$ act on $|\psi\rangle$ gives

$$\begin{aligned}\hat{O}_{j,j+1}|\psi\rangle &= \sum_{\sigma_j,\sigma_{j+1}}\sum_{a_{j-1},a_{j+1}}\Theta^{\sigma_j,\sigma_{j+1}}_{a_{j-1},a_{j+1}}\sum_{\sigma'_j,\sigma'_{j+1}}\langle\sigma'_j\sigma'_{j+1}|\hat{O}_{j,j+1}|\sigma_j\sigma_{j+1}\rangle|\alpha_{a_{j-1}}\rangle|\sigma'_j\sigma'_{j+1}\rangle|\beta_{a_{j+1}}\rangle \\ &= \sum_{\sigma'_j,\sigma'_{j+1}}\sum_{a_{j-1},a_{j+1}}\tilde{\Theta}^{\sigma'_j,\sigma'_{j+1}}_{a_{j-1},a_{j+1}}|\alpha_{a_{j-1}}\rangle|\sigma'_j\sigma'_{j+1}\rangle|\beta_{a_{j+1}}\rangle.\end{aligned} \tag{3.23}$$

This yields a similar expression as equation 3.22, but now with a new $\tilde{\Theta}^{\sigma'_j,\sigma'_{j+1}}_{a_{j-1},a_{j+1}}$:

$$\tilde{\Theta}^{\sigma'_j,\sigma'_{j+1}}_{a_{j-1},a_{j+1}} = \sum_{\sigma_j,\sigma_{j+1}} \Theta^{\sigma_j,\sigma_{j+1}}_{a_{j-1},a_{j+1}} \langle \sigma'_j \sigma'_{j+1} | \hat{O}_{j,j+1} | \sigma_j \sigma_{j+1} \rangle . \tag{3.24}$$

The number of steps needed for this update is $\mathcal{O}(d^4\chi^2)$. Now, after applying $\hat{O}_{j,j+1}$, the canonical form as in equation (3.22) should be restored. First, the tensor $\tilde{\Theta}^{\sigma'_j,\sigma'_{j+1}}_{a_{j-1},a_{j+1}}$ is reshaped to $\tilde{\Theta}_{(a_{j-1},a_{j+1})(\sigma'_j,\sigma'_{j+1})}$ and after that a singular value decomposition is applied:

$$\tilde{\Theta}^{\sigma'_j,\sigma'_{j+1}}_{a_{j-1},a_{j+1}} = \sum_{a_j} \tilde{U}^{\sigma'_j}_{a_{j-1},a_j} \tilde{\Lambda}_{a_j} \tilde{V}^{\sigma'_{j+1}}_{a_j,a_{j+1}} . \tag{3.25}$$

However, to recover the canonical form, the diagonal matrices Λ on the left and right are still missing in this expression. This problem can be resolved in a similar way as in (3.12), by multiplying with $\Lambda^{(j-1)}\left(\Lambda^{(j-1)}\right)^{-1}$ on the right-hand side and with $\left(\Lambda^{(j+1)}\right)^{-1}\Lambda^{(j+1)}$ on the left-hand side.

The orthonormality of $|\alpha_{a_j}\rangle$ and $|\beta_{a_{j+1}}\rangle$ makes calculating the expectation, using (3.22) and (3.23), quite easy. It turns out that the expectation of $\hat{O}_{j,j+1}$ is simply given by

$$\langle \psi | \hat{O}_{j,j+1} | \psi \rangle = \sum_{\sigma_j,\sigma_{j+1}} \sum_{a_{j-1},a_{j+1}} \Theta^{\sigma_j,\sigma_{j+1}}_{a_{j-1},a_{j+1}} \tilde{\Theta}^{\sigma_j,\sigma_{j+1}}_{a_{j-1},a_{j+1}} . \tag{3.26}$$

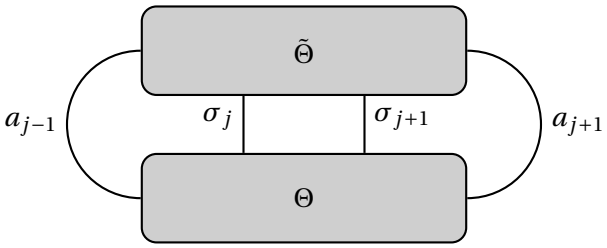

The dot product between two MPS's can be efficiently calculated in $\mathcal{O}(d\chi^3 L)$ steps. One might intuitively construct the full wavefunction and contract over its legs, but that would lead to $\mathcal{O}(d^L)$ steps in total. The efficient method is to start at the leftmost site and working towards the right, successively performing the contraction at each site.
Let $|\psi\rangle$ and $|\phi\rangle$ be

$$|\psi\rangle = \sum_{\sigma_1,\ldots,\sigma_L} \sum_{a_1,\ldots,a_L} \Gamma^{\sigma_1}_{a_1} \Lambda_{a_1} \cdots \Lambda_{a_{L-1}} \Gamma^{\sigma_L}_{a_{L-1}} |\sigma_1 \sigma_2 \cdots \sigma_L\rangle \text{ and} \tag{3.27a}$$

$$|\phi\rangle = \sum_{\sigma_1,\ldots,\sigma_L} \sum_{a_1,\ldots,a_L} \tilde{\Gamma}^{\sigma_1}_{a_1} \tilde{\Lambda}_{a_1} \cdots \tilde{\Lambda}_{a_{L-1}} \tilde{\Gamma}^{\sigma_L}_{a_{L-1}} |\sigma_1 \sigma_2 \cdots \sigma_L\rangle . \tag{3.27b}$$

The dot product $\langle\phi|\psi\rangle$ is constructed as

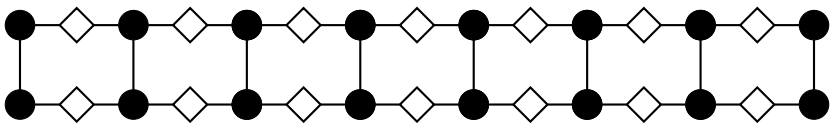

where the upper chain is $\langle\phi|$ and the lower chain is $|\psi\rangle$ and they are connected at each site by σ_j.

To compute the dot product, we first contract the leftmost pair at site $j = 1$, creating a tensor $\mathbf{M}^{[1]}$ with elements M_{a_1,a'_1}:

$$M_{a_1,a'_1} = \sum_{\sigma_1} \left(\tilde{\Gamma}^{\sigma_1}_{a'_1}\right)^\dagger \Gamma^{\sigma_1}_{a_1} \tilde{\Lambda}_{a'_1} \Lambda_{a_1} , \tag{3.28}$$

taking $\mathcal{O}(d\chi^2)$ steps. There is a summation over σ_1 and the tensor indices are a_1 and a_1'. Applying a similar contraction for site $j=2$, would result in a tensor with the same shape:

$$M_{a_2,a_2'} = \sum_{\sigma_2} \sum_{a_1,a_1'} M_{a_1,a_1'} \left(\tilde{\Gamma}^{\sigma_2}_{a_1',a_2'}\right)^\dagger \Gamma^{\sigma_2}_{a_1,a_2} \tilde{\Lambda}_{a_2'} \Lambda_{a_2}. \tag{3.29}$$

However, this operation would cost $\mathcal{O}(d\chi^4)$ steps. To reduce the number of steps to $\mathcal{O}(d\chi^3)$, we first evaluate

$$X^{\sigma_2}_{a_1',a_2} = \sum_{a_1} M_{a_1,a_1'} \Gamma^{\sigma_2}_{a_1,a_2} \tag{3.30}$$

and secondly

$$M_{a_2,a_2'} = \sum_{\sigma_2} \sum_{a_1'} X^{\sigma_2}_{a_1',a_2} \left(\tilde{\Gamma}^{\sigma_2}_{a_1',a_2'}\right)^\dagger \tilde{\Lambda}_{a_2'}, \Lambda_{a_2} \tag{3.31}$$

both of which only take $\mathcal{O}(d\chi^3)$ steps.

This process is repeated for the sites $j=2$ up to $L-1$. The last step at $j=L$ is simply

$$\langle\phi|\psi\rangle = \sum_{\sigma_L} \sum_{a_{L-1},a_{L-1}'} M_{a_{L-1},a_{L-1}'} \left(\tilde{\Gamma}^{\sigma_L}_{a_{L-1}'}\right)^\dagger \Gamma^{\sigma_L}_{a_{L-1}}, \tag{3.32}$$

taking $\mathcal{O}(d\chi^2)$ steps, just as the first step. Therefore, this process takes $\mathcal{O}(d\chi^3 L)$ steps in total.

3.4. Matrix Product Density Operators

In the previous section, we explained how the expectation of operators acting on one or two sites could be computed. There are also operators that act on more sites. These operators grow rapidly in size depending on the number of sites, so it is beneficial to establish a method similar to MPS for operators. It appears that a generalisation of MPS is sufficient to achieve this. The MPS expression was derived in section 3.2 as

$$\langle\sigma_1\sigma_2\cdots\sigma_L|\psi\rangle = \mathbf{A}^{\sigma_1}\mathbf{A}^{\sigma_2}\cdots\mathbf{A}^{\sigma_L}, \tag{3.33}$$

which can be generalised as

$$\langle\sigma_1\sigma_2\cdots\sigma_L|\,\hat{O}\,|\sigma_1'\sigma_2'\cdots\sigma_L'\rangle = \mathbf{W}^{\sigma_1.\sigma_1'}\mathbf{W}^{\sigma_2,\sigma_2'}\cdots\mathbf{W}^{\sigma_L,\sigma_L'}. \tag{3.34}$$

The matrices $\mathbf{W}^{\sigma_j,\sigma_j'}$ are similar to the matrices $\mathbf{A}^{\sigma_j}$ of MPS. The difference is, however, that unlike MPS, each $\mathbf{W}$ has two spin indices, σ and σ'. Orthonormality of the states $|\sigma_j\rangle$ allows us to write the operator as a matrix product:

$$\hat{O} = \sum_{\substack{\sigma_1,\ldots,\sigma_L,\\ \sigma_1',\ldots,\sigma_L'}} \mathbf{W}^{\sigma_1.\sigma_1'}\mathbf{W}^{\sigma_2,\sigma_2'}\cdots\mathbf{W}^{\sigma_L,\sigma_L'}\,|\sigma_1'\sigma_2'\cdots\sigma_L'\rangle\,\langle\sigma_1\sigma_2\cdots\sigma_L|\,, \tag{3.35}$$

which can also be written as

$$\hat{O} = \sum_{\substack{\sigma_1,\ldots,\sigma_L,\\ \sigma_1',\ldots,\sigma_L'}} c_{(\sigma_1\ldots\sigma_L)(\sigma_1'\ldots\sigma_L')}\,|\sigma_1'\sigma_2'\cdots\sigma_L'\rangle\,\langle\sigma_1\sigma_2\cdots\sigma_L| \tag{3.36a}$$

$$= \sum_{\substack{\sigma_1,\ldots,\sigma_L,\\ \sigma_1',\ldots,\sigma_L'}} c_{(\sigma_1\sigma_1')\ldots(\sigma_L\sigma_L')}\,|\sigma_1'\sigma_2'\cdots\sigma_L'\rangle\,\langle\sigma_1\sigma_2\cdots\sigma_L|\,. \tag{3.36b}$$

This representation is very similar to the MPS representation as in (3.7). The only difference are the extra legs of the tensor, σ_j', pointing upwards, which result from the extra set of spin indices σ'.

In section 2.5 we have seen that open quantum systems must be described by their density operator and not by a vector in the system's Hilbert space. Therefore, it is important that we derive an expression similar to MPS for density operators. The *matrix product density operator* (MPDO) [67] is defined as

$$\begin{aligned}\hat{\rho} &= \sum_{\substack{\sigma_1,\ldots,\sigma_L,\\ \sigma'_1,\ldots,\sigma'_L}} c_{(\sigma_1\sigma'_1)\ldots(\sigma_L\sigma'_L)} \left|\sigma_1\cdots\sigma_L\right\rangle \left\langle\sigma'_1\cdots\sigma'_L\right| \\ &= \sum_{\substack{\sigma_1,\ldots,\sigma_L,\\ \sigma'_1,\ldots,\sigma'_L}} \mathbf{M}^{\sigma_1,\sigma'_1}\ldots\mathbf{M}^{\sigma_L,\sigma'_L} \left|\sigma_1\cdots\sigma_L\right\rangle \left\langle\sigma'_1\cdots\sigma'_L\right| \\ &= \sum_{a_1,\ldots,a_{L-1}} \sum_{\substack{\sigma_1,\ldots,\sigma_L,\\ \sigma'_1,\ldots,\sigma'_L}} M^{\sigma_1,\sigma'_1}_{a_1} M^{\sigma_2,\sigma'_2}_{a_1,a_2}\ldots M^{\sigma_L,\sigma'_L}_{a_{L-1}} \left|\sigma_1\cdots\sigma_L\right\rangle \left\langle\sigma'_1\cdots\sigma'_L\right|,\end{aligned} \tag{3.37}$$

Given a density matrix $\hat{\rho} = \sum_j p_j \left|\psi_j\right\rangle \left\langle\psi_j\right|$, each pure state $\left|\psi_j\right\rangle$ can be described as an MPS according to (3.11). The outer product $\left|\psi_j\right\rangle \left\langle\psi_j\right|$ can be formed by taking the tensor product of the MPS representation of $\left|\psi_j\right\rangle$ with its Hermitian conjugate. This results in the following MPO:

$$\left|\psi_j\right\rangle \left\langle\psi_j\right| = \sum_{\substack{\sigma_1,\ldots,\sigma_L,\\ \sigma'_1,\ldots,\sigma'_L}} \left(\mathbf{A}^{\sigma_1(j)} \otimes \left(\mathbf{A}^{\sigma'_1(j)}\right)^\dagger\right)\left(\mathbf{A}^{\sigma_2(j)} \otimes \left(\mathbf{A}^{\sigma'_2(j)}\right)^\dagger\right)\cdots\left(\mathbf{A}^{\sigma_L(j)} \otimes \left(\mathbf{A}^{\sigma'_L(j)}\right)^\dagger\right)\left|\sigma_1\sigma_2\cdots\sigma_N\right\rangle \left\langle\sigma'_1\sigma'_2\cdots\sigma'_L\right|. \tag{3.38}$$

Computing this MPO for each $\left|\psi_j\right\rangle$ allows us to write the MPDO, differently than in (3.37), as

$$\begin{aligned}\hat{\rho} &= \sum_j p_j \left|\psi_j\right\rangle \left\langle\psi_j\right| \\ &= \sum_j \sum_{\substack{\sigma_1,\ldots,\sigma_L,\\ \sigma'_1,\ldots,\sigma'_L}} p_j \left(\mathbf{A}^{\sigma_1(j)} \otimes \left(\mathbf{A}^{\sigma'_1(j)}\right)^\dagger\right)\left(\mathbf{A}^{\sigma_2(j)} \otimes \left(\mathbf{A}^{\sigma'_2(j)}\right)^\dagger\right)\cdots\left(\mathbf{A}^{\sigma_L(j)} \otimes \left(\mathbf{A}^{\sigma'_L(j)}\right)^\dagger\right)\left|\sigma_1\sigma_2\cdots\sigma_N\right\rangle \left\langle\sigma'_1\sigma'_2\cdots\sigma'_L\right| \\ &= \sum_j \sum_{\substack{\sigma_1,\ldots,\sigma_L,\\ \sigma'_1,\ldots,\sigma'_L}} \sum_{\substack{a_1,\ldots,a_{L-1},\\ a'_1,\ldots,a'_{L-1}}} p_j \left(A^{\sigma_1(j)}_{a_1} \otimes \left(A^{\sigma'_1(j)}_{a'_1}\right)^\dagger\right)\left(A^{\sigma_2(j)}_{a_1,a_2} \otimes \left(A^{\sigma'_2(j)}_{a'_1,a'_2}\right)^\dagger\right)\cdots\left(A^{\sigma_L(j)}_{a_{L-1}} \otimes \left(\mathbf{A}^{\sigma'_L(j)}_{a'_{L-1}}\right)^\dagger\right) \\ &\qquad \cdot \left|\sigma_1\sigma_2\cdots\sigma_N\right\rangle \left\langle\sigma'_1\sigma'_2\cdots\sigma'_L\right|\end{aligned} \tag{3.39}$$

This expression is similar to (3.37), but includes a sum over j. For this reason, it is very difficult to express the matrices $\mathbf{M}^{\sigma_i,\sigma'_i}$ in terms of $\mathbf{A}^{\sigma_i(j)}$. However, for pure states the sum disappears, allowing us to write $\mathbf{M}^{\sigma_i,\sigma'_i}$ as

$$\mathbf{M}^{\sigma_i\sigma'_i} = \mathbf{A}^{\sigma_i}\left(\mathbf{A}^{\sigma'_i}\right)^\dagger = \mathbf{\Gamma}^{\sigma_i}\left(\mathbf{\Gamma}^{\sigma'_i}\right)^\dagger \left|\mathbf{\Lambda}^{[i]}\right|^2, \tag{3.40}$$

which is another way of stating $\hat{\rho} = \left|\psi\right\rangle \left\langle\psi\right|$, as we would expect, since the state is pure. Interesting to note is the similarity in notation between the outer product $\left|\psi\right\rangle \left\langle\psi\right|$, essentially as in (3.40), and the inner product $\left\langle\psi|\psi\right\rangle$, as in (3.28). For the inner product, we connect the legs σ_i and σ'_i, while for the outer product, they will remain. Therefore, the trace of the outer product should be equal to the inner product, which we already saw in section 2.2.

The MPDO representation can be made a column vector by concatenating its columns, essentially reshaping it to the same form as MPS. This *vectorisation* process can be convenient for numerical implementation. Gilchrist et al. [24] completed an extensive review of vectorisation in the context of quantum operations, which we used as the basis for this part. The new *vectorised density operator*

that will be denoted as $|\hat{\rho}\rangle\rangle$, is given by

$$|\hat{\rho}\rangle\rangle = \sum_j p_j \begin{bmatrix} \left(\psi_1^j\right)^* |\psi^j\rangle \\ \left(\psi_2^j\right)^* |\psi^j\rangle \\ \vdots \\ \left(\psi_N^j\right)^* |\psi^j\rangle \end{bmatrix} = \sum_j p_j \begin{bmatrix} \left(\psi_1^j\right)^* \psi_1^j \\ \left(\psi_1^j\right)^* \psi_2^j \\ \vdots \\ \left(\psi_1^j\right)^* \psi_N^j \\ \left(\psi_2^j\right)^* \psi_1^j \\ \vdots \end{bmatrix}, \tag{3.41}$$

with $N = 2^L$. The vectorised density operator can be described by a vectorised MPDO (vMPDO), which functions similar as a normal MPS. Note that it does not describe a wavefunction, but is just another way to write the density operator.

As discussed in section 2.5, time operations on $\hat{\rho}$ act both on the left and on the right side. However, vectorising $\hat{\rho}$ results in a column vector, on which operators can only act on one side, as $|\mathbf{A}\hat{\rho}\mathbf{B}\rangle\rangle = \mathbf{A}\otimes\mathbf{B}^{\mathrm{T}}|\hat{\rho}\rangle\rangle$. This property allows us to rewrite the Von Neumann equation (2.26) as

$$|\dot{\hat{\rho}}\rangle\rangle = -\mathrm{i}\left(\mathscr{H}\otimes\mathbb{I} - \mathbb{I}\otimes\mathscr{H}^{\mathrm{T}}\right)|\hat{\rho}\rangle\rangle \tag{3.42}$$

In a similar way, it is possible to determine the Lindblad superoperator $\mathscr{L}$ [44]:

$$\mathscr{L} = -\mathrm{i}\left(\mathscr{H}\otimes\mathbb{I} - \mathbb{I}\otimes\mathscr{H}^{\mathrm{T}}\right) + \sum_i \gamma_i \left(\hat{L}_i\otimes\hat{L}_i^* - \tfrac{1}{2}\hat{L}_i^\dagger\hat{L}_i\otimes\mathbb{I} - \tfrac{1}{2}\mathbb{I}\otimes\hat{L}_i^{\mathrm{T}}\hat{L}_i^*\right), \tag{3.43}$$

The general solution (2.33, 2.34) becomes

$$\begin{aligned} |\hat{\rho}(t)\rangle\rangle &= e^{t\mathscr{L}}|\hat{\rho}_0\rangle\rangle \\ &= \sum_{k=0}^{\infty}\frac{(t\mathscr{L})^k}{k!}|\hat{\rho}_0\rangle\rangle, \end{aligned} \tag{3.44}$$

with $\mathscr{L}$ as in (3.43).

In section 2.2 we stated three important properties of the density operator. In practice, it turns out that the first property, the trace being one, is in general not fulfilled, because the MPS method preserves the Euclidean norm, $\langle\langle\hat{\rho}|\hat{\rho}\rangle\rangle$, instead of the trace, $\langle\langle\mathbb{I}|\hat{\rho}\rangle\rangle$ [44]. In order to compute the expectation value of an operator $\hat{O}$, see equation (2.13), we should compensate for this:

$$\langle\hat{O}\rangle = \frac{\mathrm{Tr}\left(\hat{\rho}\hat{O}\right)}{\mathrm{Tr}(\hat{\rho})} = \frac{\langle\langle\mathbb{I}|\mathbb{I}\otimes\hat{O}|\hat{\rho}\rangle\rangle}{\langle\langle\mathbb{I}|\hat{\rho}\rangle\rangle}. \tag{3.45}$$

3.5. Time Evolving Block Decimation

In this section the time evolution of the quantum state $|\psi\rangle$ and of the density operator $\hat{\rho}$ will be treated, in the context of matrix product states and matrix product density operators, respectively.

The Schrödinger equation (2.1) governs the dynamics of quantum states, and the states evolve according to (2.3). This yields the time evolution operator $\hat{U} = e^{-\mathrm{i}t\hat{H}}$. The Hamiltonian is local, acting only between two neighbouring sites:

$$\hat{H} = \sum_{j=1}^{L-1}\hat{h}(\sigma_j,\sigma_{j+1}). \tag{3.46}$$

The couplings $\hat{h}$ for two neighbouring links do not commute, as they share a σ_j, but couplings between links two sites or more apart do commute. It is therefore useful to separate the Hamiltonian into an even and an odd part: $\hat{H} = \hat{H}_e + \hat{H}_o$, given by

$$\hat{H}_e = \sum_{j=1}^{N_e} \hat{h}(\sigma_{2j}, \sigma_{2j+1}), \text{ and} \tag{3.47a}$$

$$\hat{H}_o = \sum_{j=1}^{N_o} \hat{h}(\sigma_{2j-1}, \sigma_{2j}), \tag{3.47b}$$

where the terms within each of the two summations commute, but $\hat{H}_e$ does not commute with $\hat{H}_o$. In the case of even L, the upper bounds N_e and N_o are $L/2-1$ and $L/2$, respectively, whereas in the case of odd L, the upper bounds both are $(L-1)/2$.

Considering numerical time integration, which will be the main topic of chapter 4, we introduce the time step $\Delta t = \frac{t}{N}$, where N is the total number of steps. The time evolution operator can then be rewritten as

$$e^{-\mathrm{i}t\hat{H}} = \left(e^{-\mathrm{i}\Delta t\hat{H}}\right)^N, \tag{3.48}$$

Applying the Lie-Trotter-Suzuki approximation [12] to the time evolution operator $e^{-\mathrm{i}\Delta t\hat{H}}$ yields the *Time Evolution Block Decimation* (TEBD) method [70]. The second order approximation gives

$$e^{-\mathrm{i}\Delta t\hat{H}} = e^{-\mathrm{i}\Delta t(\hat{H}_e+\hat{H}_o)} = e^{-\frac{\mathrm{i}}{2}\Delta t\hat{H}_e} e^{-\mathrm{i}\Delta t\hat{H}_o} e^{-\frac{\mathrm{i}}{2}\Delta t\hat{H}_e} + \mathcal{O}(\Delta t^3), \tag{3.49}$$

Applying this successively, this can be visualised as

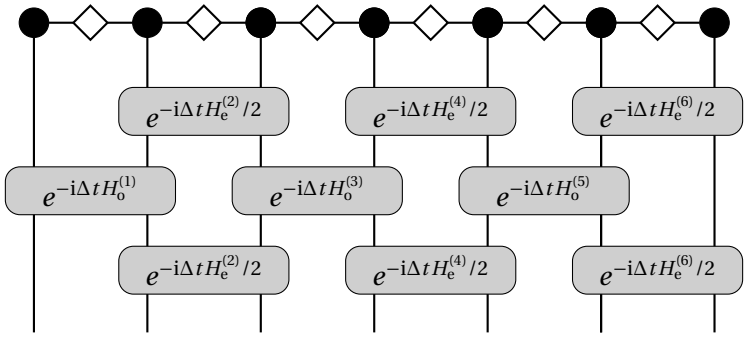

The time evolution operators for the even and odd links acting on $|\psi\rangle$ can be written as

$$\hat{T}_e|\psi\rangle = \prod_{j=1}^{N_e} e^{-\mathrm{i}\Delta t\hat{h}(\sigma_{2j},\sigma_{2j+1})}|\psi\rangle, \text{ and} \tag{3.50a}$$

$$\hat{T}_o|\psi\rangle = \prod_{j=1}^{N_o} e^{-\frac{\mathrm{i}}{2}\Delta t\hat{h}(\sigma_{2j-1},\sigma_{2j})}|\psi\rangle. \tag{3.50b}$$

Imaginary time evolution ($\tau = \mathrm{i}t$) can be used to determine the ground state of the system. For a gapped system, the energy of the ground state has a lower energy than that of all other states ($E_0 < E_j$). In (2.4) we already wrote $|\psi\rangle$ as a sum over different energy states $|\psi_j\rangle$ with energy E_j, which clearly illustrates that for imaginary time evolution only $|\psi_0\rangle$, the ground state with the lowest energy E_0, will remain. The contribution of the ground state will tend to zero slower than those of the excited states and will therefore survive for large τ:

$$\lim_{\tau\to\infty} e^{-\tau\hat{H}}|\psi\rangle \propto |\psi_0\rangle. \tag{3.51}$$

The imaginary time evolution operator is not unitary, and therefore the resulting state is not normalised. In this case, the norm decreases exponentially, but renormalisation corrects for this error.

We will now investigate the time evolution of the MPDO, which is similar to MPS. First, we will treat a closed system, and second, an open system.

The real time evolution of $\hat{\rho}$ in a closed system is given by (2.25). For a time step Δt this becomes

$$\hat{\rho}(t+\Delta t) = e^{-\mathrm{i}\Delta t\hat{H}}\hat{\rho}(t)e^{\mathrm{i}\Delta t\hat{H}}. \tag{3.52}$$

Here, we can also apply TEBD in the same way as before concerning MPS, but now applying the method on both 'sides' of the MPDO. We use the same $\hat{H}_e$ and $\hat{H}_o$ as before, which results in a very similar second-order approximation scheme:

$$e^{-\mathrm{i}\Delta t\hat{H}}\hat{\rho}e^{\mathrm{i}\Delta t\hat{H}} = e^{-\frac{\mathrm{i}}{2}\Delta t\hat{H}_e}e^{-\mathrm{i}\Delta t\hat{H}_o}e^{-\frac{\mathrm{i}}{2}\Delta t\hat{H}_e}\hat{\rho}e^{\frac{\mathrm{i}}{2}\Delta t\hat{H}_e}e^{\mathrm{i}\Delta t\hat{H}_o}e^{\frac{\mathrm{i}}{2}\Delta t\hat{H}_e} + \mathcal{O}(\Delta t^3). \tag{3.53}$$

This can be visualised in a similar way as MPS. The operators on the left of $\hat{\rho}$ act on the lower legs exactly in the same way as considering MPS, and the operators to right of $\hat{\rho}$ now act on the upper legs of the MPDO. This gives the following time-evolution operators:

$$\mathcal{T}_{\mathrm{e},\lambda}(\hat{\rho}) = \prod_{j=1}^{N_e} e^{-\mathrm{i}\lambda\Delta t\hat{h}(\sigma_{2j},\sigma_{2j+1})}\hat{\rho}e^{\mathrm{i}\lambda\Delta t\hat{h}(\sigma'_{2j},\sigma'_{2j+1})} \text{ and} \tag{3.54a}$$

$$\mathcal{T}_{\mathrm{o},\lambda}(\hat{\rho}) = \prod_{j=1}^{N_o} e^{-\mathrm{i}\lambda\Delta t\hat{h}(\sigma_{2j-1},\sigma_{2j})}\hat{\rho}e^{\mathrm{i}\lambda\Delta t\hat{h}(\sigma'_{2j-1},\sigma'_{2j})}, \tag{3.54b}$$

with $\lambda = ½$, when an operator is separated into two, such as $e^{-\frac{\mathrm{i}}{2}\Delta t\hat{H}_e}$ in (3.53), and with $\lambda = ½$, if the operator is not separated.

In this thesis, we will consider the vectorised density operator as discussed in section 3.4. Therefore, we will not apply TEBD in the way described directly above, but as in (3.49), the MPS approach.

In section 2.5 we found the time evolution of $\hat{\rho}$ in an open quantum system, the general solution to the Lindblad equation. Introducing the time step Δt, this becomes

$$\hat{\rho}(t+\Delta t) = e^{\Delta t\mathscr{L}}\hat{\rho}(t), \tag{3.55}$$

where the Lindbladian superoperator $\mathscr{L}$ consists of a Hamiltonian part and a dissipative part. Note that the dissipation $\mathscr{D}$ in the system under consideration acts only on the single sites 1 and L, and recall that the Hamiltonian $\hat{H}$ is separated into a set of even and odd two-site operators $\hat{h}$. The dissipation can be trivially transformed into a two-site operator that commutes with the Hamiltonian part acting on the neighbouring link, by introducing the direct product with a unit operator. This allows us to merge the Hamiltonian at the first and last links with the dissipation. This way, the Lindbladian superoperator is transformed into a two-site operator that commutes with the neighbouring couplings $\hat{h}$. In the previous section, we discussed the vectorisation of the density operator. We now vectorise the superoperators $\mathscr{T}$ and $\mathscr{L}$ to set up the TEBD algorithm for the vectorised density operator. The vectorised $\mathscr{T}_{\mathrm{e},\lambda}$ is given as

$$\mathscr{T}_{\mathrm{e},\lambda}|\hat{\rho}\rangle\rangle = \prod_{j=1}^{N_e} e^{-\mathrm{i}\lambda\Delta t\hat{h}(\sigma_{2j},\sigma_{2j+1})} \otimes \left(e^{\mathrm{i}\lambda\Delta t\hat{h}(\sigma'_{2j},\sigma'_{2j+1})}\right)^T |\hat{\rho}\rangle\rangle, \tag{3.56}$$

with $\lambda = ½,1$. $\mathscr{T}_{\mathrm{o},\lambda}$ is constructed in a similar way, and the vectorised $\mathscr{L}$ is given as in (3.43). The new TEBD algorithm for an open quantum system for the vectorised density operator is visualised as

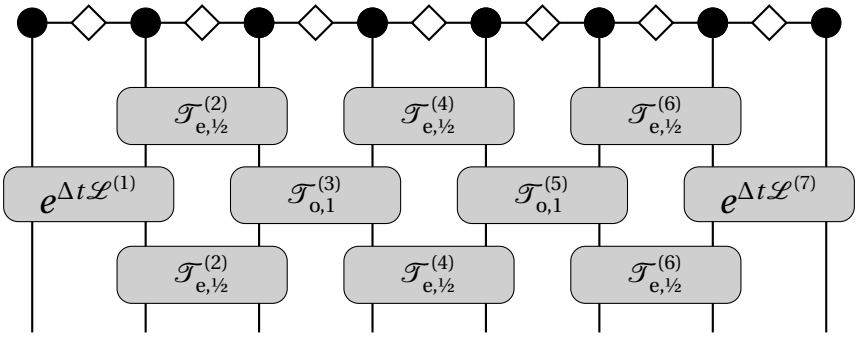

for even L, and

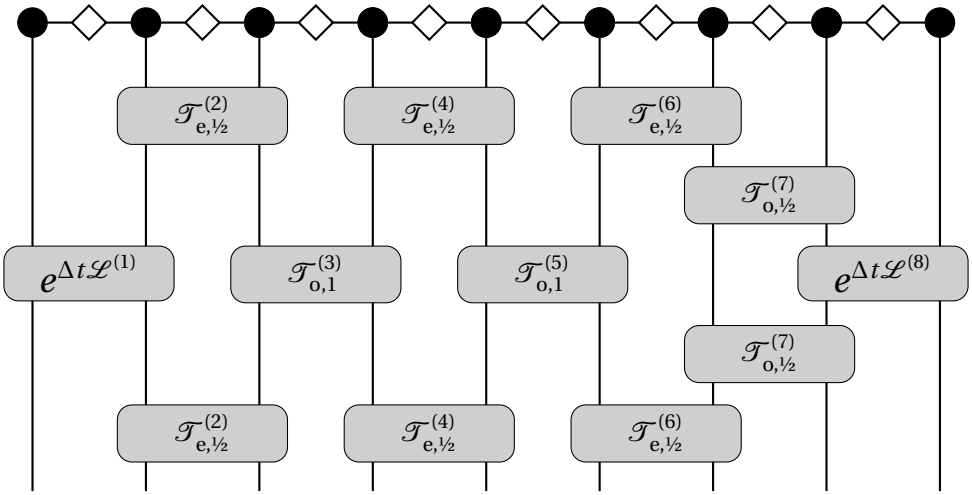

for odd L. The bulk of the system (links 2 through L-2/L-3) is the same as for a closed system considered before. TEBD is a consecutive process, which means that we apply the scheme above successively. For all steps except the first and the last, the bottom row of operators of the first step is equal to the top row of operators of the following step, as the Hamiltonian is time-independent. Therefore, we can combine these operators, reducing the computational cost significantly.

In this section we have discussed the application of TEBD in the context of MPS and (vectorised) MPDO. We divided the system into the bulk, consisting of solely the Hamiltonian part, and the two edges, which also include the dissipative terms. We can apply the Crank-Nicolson method [15] to all Hamiltonian parts, since it is a unitary operation, preserving the three properties of $\hat{\rho}$. However, for the Lindbladian superoperator, Crank-Nicolson is no longer unitary, due to the included dissipative terms. The approximation of the operator exponential $e^{\Delta t\mathcal{L}}$ will be the main topic of the next chapter.

4

Numerical Time Integration

In chapter 2 we discussed quantum systems and the Lindblad equation, and in chapter 3 we introduced the concepts of MPS and MPDO and their applications. Now we need to determine how we can solve the Lindblad equation in the context of MPDO. First, we will study general numerical solutions, and then, introduce the MPDO.

4.1. Numerical Schemes for the Density Operator

The main idea of this section is to find a suitable approximation method for $e^{\Delta t \mathscr{L}}$, which was discussed at the end of the previous chapter. We will consider multiple approaches that are known to be useful for similar problems. Cao and Lu [11] performed an extensive review, which we used as the foundation for this and the next section.

In section 2.2, we concluded that there are three important properties of the density operator that need to be satisfied. Those were

1. $\mathrm{Tr}\left(\hat{\rho}\right) = 1$,
2. $\hat{\rho}$ is Hermitian,
3. $\hat{\rho}$ is positive semi-definite.

Ideally, the numerical scheme conserves all three of these properties. However, as we discussed in section 3.4, the MPS/MPDO approach breaks the trace conservation as a consequence of the vectorisation procedure. We also explained that the non-unit trace can be compensated for in a straightforward way. This also holds for errors caused by numerical schemes. Therefore, the other properties will be prioritised. The positivity and trace of $\hat{\rho}$ can be difficult to preserve, as we shall see.

In section 2.5, we discussed the *Taylor series* of $e^{\Delta t \mathscr{L}}$, see equation (2.34). Cutting off this series above $k = M$ for some positive integer M, yields the following approximation for the exponential:

$$e^{\Delta t \mathscr{L}} = \sum_{k=0}^{M} \frac{(\Delta t \mathscr{L})^k}{k!} + \mathscr{O}(\Delta t^{M+1}). \tag{4.1}$$

This method preserves the trace (as $\mathrm{Tr}[\mathscr{L}(\hat{\rho})] = 0$, see (2.35)), however, not the positivity [56]. We present an example of the violation of the positive semi-definiteness for the (first-order) Euler method in appendix A.

The *Crank-Nicholson* (CN) method is a second-order *implicit* Runge-Kutta method. However, Bidégaray et al. [3] showed that the CN method does not preserve the positivity of $\hat{\rho}$ considering (2.26) for the dimension $d \geq 3$.

A method often used to approximate matrix and operator exponentials is the *Padé approximation* [46]. The (q, q)-Padé approximation is given by:

$$\mathscr{R}_q(\Delta t\mathscr{L}) = \left(\mathscr{N}_q(-\Delta t\mathscr{L})\right)^{-1}\mathscr{N}_q(\Delta t\mathscr{L}), \tag{4.2}$$

where

$$\mathscr{N}_q(\mathscr{A}) = \sum_{j=0}^{q}\frac{(2q-j)!q!}{2q!j!(q-j)!}\mathscr{A}^j. \tag{4.3}$$

The Padé approximation does, however, not preserve the positivity of the density operator, as it is similar to the CN method discussed above [11]. In addition, the computational and storage costs are high.

Operator splitting methods divide the Lindblad superoperator into two parts. The operator exponential $e^{\Delta t\mathscr{L}}\hat{\rho}$, see (2.30), is quite complicated, so splitting can be beneficial. We hope that by splitting $\mathscr{L}$, the two separate parts behave more nicely and can be approximated in an easier way. We will look into two different options in the next section.

The Kraus superoperator lets an operator $\mathscr{A}$ act to the right-hand side of $\hat{\rho}$, and its Hermitian conjugate to left-hand side of $\hat{\rho}$. It will be important in the next section and it is given by

$$\mathscr{K}\left[\mathscr{A}\right](\hat{\rho}) = \mathscr{A}\hat{\rho}\mathscr{A}^\dagger, \tag{4.4}$$

and the vectorisation of the Kraus superoperator is

$$\left|\mathscr{K}\left[\mathscr{A}\right](\hat{\rho})\right\rangle\!\rangle = \mathscr{A}\otimes\mathscr{A}^*\left|\hat{\rho}\right\rangle\!\rangle. \tag{4.5}$$

The Kraus representation is linear, positivity and trace-preserving and Hermitian [74], meaning all three properties of $\hat{\rho}$ are preserved. For this reason, the Kraus representation will be valuable in the next section. Although we cannot directly implement it to approximate $e^{\Delta t\mathscr{L}}$, it is be very useful for approximating other exponentials, for which we also need to preserve the three properties.

4.2. Operator Splitting Methods

The obvious choice would be to split the Lindblad superoperator into a Hamiltonian and a dissipative part as

$$\mathscr{L} = \mathscr{L}_H + \mathscr{L}_D, \tag{4.6a}$$

$$\mathscr{L}_H(\hat{\rho}) = \mathrm{i}\left[\hat{\rho}, \hat{H}\right], \qquad \mathscr{L}_D(\hat{\rho}) = \sum_i \gamma_i\left(\hat{L}_i\hat{\rho}\hat{L}_i^\dagger - \frac{1}{2}\left\{\hat{L}_i^\dagger\hat{L}_i, \hat{\rho}\right\}\right) \tag{4.6b}$$

The next step is to apply a splitting scheme for the operator exponential. Applying the second-order *Lie-Trotter-Suzuki approximation* gives

$$e^{\Delta t\mathscr{L}} = e^{\Delta t\mathscr{L}_D/2}e^{\Delta t\mathscr{L}_H}e^{\Delta t\mathscr{L}_D/2} + \mathscr{O}(\Delta t^3), \tag{4.7}$$

where $\mathscr{L}_H$ and $\mathscr{L}_D$ could in principle be interchanged, but such a change would not change anything fundamentally. For a time-dependent Lindblad superoperator, the order as in (4.7) leads to a slightly more efficient scheme. In this thesis, the Lindblad superoperator is time-independent, so the order does not matter. Therefore, we can choose to just use the expression given in (4.7).

A second splitting choice divides the Lindblad superoperator as

$$\mathscr{L} = \mathscr{L}_J + \mathscr{L}_L, \tag{4.8a}$$

$$\mathscr{L}_J(\hat{\rho}) = J\hat{\rho} + \hat{\rho}J^\dagger, \qquad \mathscr{L}_L(\hat{\rho}) = \sum_i \gamma_i\hat{L}_i\hat{\rho}\hat{L}_i^\dagger, \tag{4.8b}$$

where J is defined as

$$J = -\mathrm{i}H_{\text{eff}}, \qquad H_{\text{eff}} = H + \frac{1}{2\mathrm{i}}\sum_i \gamma_i \hat{L}_i^\dagger \hat{L}_i. \tag{4.9}$$

Here, we introduce the *effective Hamiltonian* H_{eff}, which contains some of the factors that were initially part of the dissipation, together with the original Hamiltonian H. It can be shown that $e^{\Delta t \mathscr{L}_J}$ preserves positivity [30]. The same argument holds for $\mathscr{L}_H$[1]. The superoperator $\mathscr{L}_L$ is a Kraus representation with Kraus operators L_i, which means that this superoperator is also positive. However, in general, $\mathscr{L}_D$ does not preserve positivity [11]. Therefore, we choose to continue to focus on the second splitting method (4.8). In a similar way as before (4.7), we can approximate $e^{\Delta t \mathscr{L}}$ in the context of the second splitting scheme as

$$e^{\Delta t \mathscr{L}} = e^{\Delta t \mathscr{L}_J/2} e^{\Delta t \mathscr{L}_L} e^{\Delta t \mathscr{L}_J/2} + \mathscr{O}(\Delta t^3). \tag{4.10}$$

We can interchange $\mathscr{L}_J$ and $\mathscr{L}_L$ in the same way as before. For a time-dependent Lindbladian superoperator, it is beneficial to use $\mathscr{L}_J$ as the inner term, but in as we use the time-independent superoperator in this thesis, the expression as in (4.10), as is widely used in other research.

As $\mathscr{L}_L$ has the Kraus representation form, a straightforward Taylor series truncation as defined in (4.1), can approximate $e^{\Delta t \mathscr{L}_L}$, while still preserving positivity. The other operator exponential, $e^{\Delta t \mathscr{L}_J}$, can be approximated similarly by the following Kraus representation:

$$e^{\Delta t \mathscr{L}_J} = \mathscr{K}\left[\sum_{\alpha=0}^{M} \frac{J^\alpha \Delta t^\alpha}{\alpha!}\right] + \mathscr{O}\left(\Delta t^{M+1}\right). \tag{4.11}$$

Since this is a Kraus representation, it preserves positivity, trace and Hermiticity of the density operator. Note that this splitting choice allows us to approximate $e^{\Delta t \mathscr{L}_J}$ and $e^{\Delta t \mathscr{L}_L}$ up to any order, while preserving all the desired properties. However, the chosen splitting scheme for $e^{\Delta t \mathscr{L}}$ imposes a limit to the order of the total approximation, in this case the maximum is second order. To achieve higher order approximation, a different scheme is needed. It has been shown that higher order Lie-Suzuki-Trotter schemes require negative time weights [62]. In the next section, we will study another approach suitable for higher order approximations, using *Duhamel's principle*, and then use quadrature methods for numerical integration.

4.3. Duhamel's Principle

We can apply Duhamel's principle to equation (3.55), where we regard $\mathscr{L}_L$ as the forcing term, as [39]

$$\hat{\rho}_{t+\Delta t} = e^{\Delta t \mathscr{L}} \hat{\rho}_t = e^{\Delta t \mathscr{L}_J} \hat{\rho}_t + \int_t^{t+\Delta t} e^{(t+\Delta t - s)\mathscr{L}_J} \mathscr{L}_L \hat{\rho}_s \, ds, \tag{4.12}$$

where we defined $\hat{\rho}_\nu = \hat{\rho}(\nu)$ for convenience. Iterating this equation gives [61]

$$\begin{aligned}
\hat{\rho}_{t+\Delta t} &= e^{\Delta t \mathscr{L}} \hat{\rho}_t \\
&= \sum_{m=0}^{\infty} \int_t^{t+\Delta t} \int_t^{s_m} \cdots \int_t^{s_2} e^{(t-s_m)(\mathscr{L}_J)} \mathscr{L}_L e^{(s_m - s_{m-1})\mathscr{L}_J} \mathscr{L}_L \cdots e^{(s_2-s_1)\mathscr{L}_J} \mathscr{L}_L e^{(s_1-t)\mathscr{L}_J} \hat{\rho}_t \mathrm{d}s_1 \ldots \mathrm{d}s_{m-1} \mathrm{d}s_m \\
&= \sum_{m=0}^{M} \int_t^{t+\Delta t} \int_t^{s_m} \cdots \int_t^{s_2} e^{(t-s_m)(\mathscr{L}_J)} \mathscr{L}_L e^{(s_m - s_{m-1})\mathscr{L}_J} \mathscr{L}_L \cdots e^{(s_2-s_1)\mathscr{L}_J} \mathscr{L}_L e^{(s_1-t)\mathscr{L}_J} \hat{\rho}_t \mathrm{d}s_1 \ldots \mathrm{d}s_{m-1} \mathrm{d}s_m \\
&\quad + \int_t^{t+\Delta t} \int_t^{s_{M+1}} \cdots \int_t^{s_2} e^{(t-s_{M+1})(\mathscr{L}_J)} \mathscr{L}_L e^{(s_{M+1} - s_M)\mathscr{L}_J} \mathscr{L}_L \cdots e^{(s_3-s_2)\mathscr{L}_J} \mathscr{L}_L e^{(s_2-s_1)\mathscr{L}_J} \hat{\rho}_{s_1} \mathrm{d}s_1 \ldots \mathrm{d}s_M \mathrm{d}s_{M+1}.
\end{aligned} \tag{4.13}$$

[1] Note that $\mathscr{L}_H$ multiplied by a factor is then also positivity preserving, e.g. (4.7) with factor $1/2$. The same holds for the other superoperators, for example $\mathscr{L}_J$, which will be discussed in (4.10).

Omitting the last term in (4.13) results in an approximation of $\hat{\rho}_{t+\Delta t}$ of order $\mathcal{O}(\Delta t^{M+1})$. For example, taking $M = 1$ yields the first order approximation

$$\begin{aligned}\hat{\rho}_{t+\Delta t} &= e^{\mathscr{L}_J \Delta t}\hat{\rho}(t) + \int_t^{t+\Delta t} e^{\mathscr{L}_J(t+\Delta t - s_1)}\mathscr{L}_L e^{\mathscr{L}_J(s_1-t)}\hat{\rho}_t \mathrm{d}s_1 \;\; + \;\; \mathcal{O}(\Delta t^2) \\ &= e^{\mathscr{L}_J \Delta t}\hat{\rho}(t) + \Delta t e^{\mathscr{L}_J \Delta t}\mathscr{L}_L \hat{\rho}_t \;\; + \;\; \mathcal{O}(\Delta t^2),\end{aligned} \tag{4.14}$$

where in the last expression we have approximated the integral to first order in Δt. It is our aim to find a second or higher order approximation scheme. For a second order scheme ($M = 2$), (4.13) reduces to

$$\begin{aligned}\hat{\rho}_{t+\Delta t} = e^{\mathscr{L}_J \Delta t}\hat{\rho}_t &+ \int_t^{t+\Delta t} e^{\mathscr{L}_J(t+\Delta t - s_1)}\mathscr{L}_L e^{\mathscr{L}_J(s_1-t)}\hat{\rho}_t \mathrm{d}s_1 \\ &+ \int_t^{t+\Delta t}\int_t^{s_2} e^{\mathscr{L}_J(t+\Delta t - s_2)}\mathscr{L}_L e^{\mathscr{L}_J(s_2-s_1)}\mathscr{L}_L e^{\mathscr{L}_J(s_1-t)}\hat{\rho}_t \mathrm{d}s_1 \mathrm{d}s_2 \;\; + \;\; \mathcal{O}(\Delta t^3).\end{aligned} \tag{4.15}$$

The second integral in the expression above becomes too complicated to approximate in a simple way. Therefore, for a second or higher order scheme ($M \geq 2$), we should further study approximation methods for the integral in (4.13). We start by approximating $e^{(t-s)\mathscr{L}_J}$ by a Kraus representation as

$$e^{(t-s)\mathscr{L}_J} = \mathscr{J}_m(t,s) + \mathcal{O}\left((t-s)^{m+1}\right), \qquad \mathscr{J}_m(t,s) := \mathscr{K}\left[\sum_{\alpha=0}^{m}\frac{J^\alpha (t-s)^\alpha}{\alpha!}\right]. \tag{4.16}$$

The sum of integrals in (4.13) is time-translation invariant. Therefore, performing a time-translation of $-t$, and substituting (4.16) into (4.13) gives

$$\begin{aligned}\hat{\rho}_{t+\Delta t} = \sum_{m=0}^{M}\int_0^{\Delta t}\int_0^{s_m}\cdots\int_0^{s_2} &\mathscr{J}_{M-m}(\Delta t, s_m)\mathscr{L}_L\mathscr{J}_{M-m}(s_m, s_{m-1})\mathscr{L}_L\cdots \\ &\mathscr{J}_{M-m}(s_2,s_1)\mathscr{L}_L\mathscr{J}_{M-m}(s_1,0)\hat{\rho}_t \mathrm{d}s_1\ldots\mathrm{d}s_{m-1}\mathrm{d}s_m \\ &+\mathcal{O}(\Delta t^{M+1}),\end{aligned} \tag{4.17}$$

Since (4.16) is in Kraus representation form, positivity is preserved. For convenience, we now introduce

$$\mathscr{F}_m^M(s_1,s_2,\ldots,s_m) = \mathscr{J}_{M-m}(\Delta t, s_m)\mathscr{L}_L\mathscr{J}_{M-m}(s_m,s_{m-1})\mathscr{L}_L\ldots\mathscr{J}_{M-m}(s_2,s_1)\mathscr{L}_L\mathscr{J}_{M-m}(s_1,0), \tag{4.18}$$

which contains all the terms inside the integral in (4.17). Substituting $\mathscr{F}_m^M$ back into (4.17) simplifies the expression as

$$\hat{\rho}_{t+\Delta t} = \sum_{m=0}^{M}\int_0^{\Delta t}\int_0^{s_m}\cdots\int_0^{s_2}\mathscr{F}_m^M(s_1,s_2,\ldots,s_m)\hat{\rho}_t \mathrm{d}s_1\ldots\mathrm{d}s_{m-1}\mathrm{d}s_m + \mathcal{O}(\Delta t^{M+1}) \tag{4.19}$$

Note that each of the operators contained in $\mathscr{F}_m^M(s_1,s_2,\ldots,s_m)$ act successively on the density operator. As each of these operators is in Kraus representation form, see (4.8b) and (4.16), $\mathscr{F}_m^M$ also is in Kraus representation form; positivity is conserved in (4.19).

4.4. High-dimensional Midpoint Method

In order to compute $\hat{\rho}(t+\Delta t)$ we need to apply quadrature methods to approximate the nested integral in (4.17). We are interested in methods of third or higher order, as we already have a convenient scheme for second-order approximation – see equation (4.10).

In the context of numerical methods, we can rewrite (4.19) as

$$y_{n+1} = \mathscr{A}_{\Delta t}^{(M)} y_n = \left[\sum_{m=0}^{M} \int_0^{\Delta t} \int_0^{s_m} \dots \int_0^{s_2} \mathscr{F}_m^M(s_1, s_2, \dots, s_m) \mathrm{d}s_1 \dots \mathrm{d}s_{m-1} \mathrm{d}s_m \right] y_n, \tag{4.20}$$

where $\mathscr{A}_{\Delta t}^M$ is an order-M scheme with time step Δt. As y_n (or $\hat{\rho}_0$) does not depend on $s_1 \dots s_M$, it allows us to take w_n out of the integral. The term with $m = 0$ contains zero integrals and can be approximated by $\mathscr{J}_n(t, s)$, an n'th order method. The other terms are more complex as they include multiple layers of dependencies, and solving them might be challenging.

However, the Lindbladian superoperator $\mathscr{L}$ in (2.30) does not depend on time, which means that solving the integral will be less complicated than using time-dependent Lindbladian operators. We propose two strategies for approximating the integral. The first is the midpoint method for high-dimensional integration as discussed in [11], and the second is the nested Runge-Kutta method, which we developed ourselves. In this section we will focus on the midpoint method and in the next section on the nested Runge-Kutta.

The general one-dimensional midpoint method is an explicit second-order time integration method, and is given as

$$y_{n+1} = \mathscr{A}_{\Delta t}^{(2,\mathrm{MP})} y_n = y_n + \Delta t f\left(t_{n+\frac{1}{2}}, y_n + \tfrac{\Delta t}{2} f(t_n, y_n)\right). \tag{4.21}$$

The specific implementation of this method for the single integral as in (4.14) can be found in [11]. For the nested integral, we use the high-dimensional midpoint method. This method is given as

$$\begin{aligned} \mathscr{A}_{\Delta t}^{(M)}(\hat{\rho}_{\Delta t}) = \mathscr{J}_M(\Delta t, 0)\hat{\rho}_0 + \Bigg(\sum_{m=1}^{M-1} \sum_{n=1}^{\min(m, N_m)} \sum_{1 \le k_1 < \dots < k_n = m} \sum_{1 \le j_1 < \dots < j_n \le N_m} \mathscr{F}_m^M(r_{j_n}, \dots, r_{j_1})\hat{\rho}_0 \\ \cdot \frac{(\Delta t / N_m)^m}{k_1!(k_2 - k_1)! \cdots (k_n - k_{n-1})!} \Bigg) + \mathscr{L}_L^M \hat{\rho}_0, \end{aligned} \tag{4.22}$$

where $N_m = \left\lceil (\Delta t)^{m-M} \right\rceil$, and $r_j = \left(j - \frac{1}{2}\right) \frac{\Delta t}{N_m}$, for $1 \le j \le N_m$. For more details on the derivation and error analysis of this method, we refer to [11]. This method preserves the Hermiticity and positivity, but not necessarily the trace. As discussed before, that is not a major issue and we can compensate for this. Since it preserves the other two properties, the method is suitable for approximating the time-evolution of $\hat{\rho}$.

The high-dimensional midpoint method is, however, not efficient for fourth or higher order approximations, as the computational cost is of the order $\mathscr{O}\left(M^{M+2}(N_1)^M\right) = \mathscr{O}\left(M^{M+2}(\Delta t)^{M(1-M)}\right)$. Especially for small Δt this increases quickly. The method might be useful for a third-order approximation, but is already too inefficient for fourth-order approximations. We would like to develop a different algorithm or method that can approximate the nested integral more efficiently, while preserving the positivity and Hermiticity of the density operator. In the next section we will study such a method; nested Runge-Kutta.

4.5. Nested Runge-Kutta Methods

Another fourth-order method we can use to approximate the integral in (4.20) is fourth-order Runge-Kutta (RK4), which can be both implicit and explicit. Since $\mathscr{F}_m^M$ is in Kraus representation form, any resulting RK scheme will be in Kraus representation form as well. Therefore, the method will preserve trace, Hermiticity and positivity. Sandretto and Chapoutot [57] provide a coverage of different RK schemes and their implementation.

Implementing Runge-Kutta for (4.20), however, is not straightforward, as a consequence of the nested integral. Regular RK schemes only solve a single integral and should be modified for nested integrals. We propose a recursive algorithm that can solve nested integrals, using the RK4 method, but which can also be adapted for higher order methods.

Explicit RK methods are relatively straightforward to implement compared to implicit methods. The computation at each stage depends only on previously computed values and does not involve solving nonlinear equations. Explicit methods are also computationally efficient, in contrast to implicit methods, which may become a major issue, as the computational time of the implicit method can possibly overtake the computational time of the MPS. Explicit RK is versatile and can be applied to a wide range of non-stiff problems. Implicit methods are even more stable than explicit schemes and can achieve high accuracy. In general, however, the high accuracy will not weigh up against the increased computational costs[2]. In this study we are mostly interested in the long-term behaviour of the system, the non-equilibrium steady state. Therefore, we have chosen to implement the explicit RK4 method, which for a single integral in (4.20) is given by

$$\vec{w}_{n+1} = \left[\mathbb{I} + \frac{\mathbf{k}_1 + 2\mathbf{k}_2 + 2\mathbf{k}_3 + \mathbf{k}_4}{6}\right] \vec{w}_n, \tag{4.23a}$$

$$\mathbf{k}_1 = \Delta t f(t_n, \mathbb{I}), \tag{4.23b}$$

$$\mathbf{k}_2 = \Delta t f(t_n + \Delta t/2, \mathbb{I} + \mathbf{k}_1/2), \tag{4.23c}$$

$$\mathbf{k}_3 = \Delta t f(t_n + \Delta t/2, \mathbb{I} + \mathbf{k}_2/2), \tag{4.23d}$$

$$\mathbf{k}_4 = \Delta t f(t_n + \Delta t, \mathbb{I} + \mathbf{k}_3). \tag{4.23e}$$

The expression in (4.20) consists of multiple nested integrals, so a more advanced method is required. This is where the nested Runge-Kutta method comes into play. By recursively applying the RK4 method at each level of the integral, the nested Runge-Kutta scheme efficiently handles multi-level integration problems. Each stage of the RK4 in the outer loop calls another RK4 process for the next level, ensuring that the accuracy and stability properties of RK4 are preserved throughout the nested structure.

The algorithm start with setting up a normal RK4 approximation for the outer integral ranging from 0 to Δt. The weights $\mathbf{k}$ depend on the function f as in (4.23a), however, this f consists of all other unknown integrals. The technique we propose, solves the next integral in a similar way, and we use these approximations as inputs for the outer integral. We repeat this process for all integrals. The innermost RK4 scheme solves a standard integral as in (4.23a), with $f = \mathscr{F}_m^M(s_1, s_2, ..., s_m)$. As each stage of the nested integral depends on the approximation of all the inner integrals, this is a recursive method. The nested Runge-Kutta algorithm is given in algorithm 1. $n = 0$ and $s_0 = \Delta t$ should be taken as starting values. n increases with one for each stage of the integral. The total number of integrals in m, and the last one is over $\mathscr{F}_m^M(s_1, s_2, ..., s_m)$. Therefore, at $n = m - 1$, we do not call another RK4 stage, but instead approximate $\mathscr{F}_m^M(s_1, s_2, ..., s_m)$. Important to note is that the timestep for each single integral is different, and is denoted by s_n, depending on all the previous s_j.

[2] In some situations, the implicit method might be preferred. Namely, high accuracy for the start of the simulation might be beneficial for other studies focused on the short-term behaviour, as the system changes rapidly in this region.

Algorithm 1 RK4(n, s_n)

if $n < m$-1 **then**
  $\mathbf{k}_1 = s_n$ **RK4**$(n{+}1,\ 0)$
  $\mathbf{k}_2 = s_n$ **RK4**$(n{+}1,\ s_n/2) \cdot (\mathbb{I} + \mathbf{k}_1/2)$
  $\mathbf{k}_3 = s_n$ **RK4**$(n{+}1,\ s_n/2) \cdot (\mathbb{I} + \mathbf{k}_2/2)$
  $\mathbf{k}_4 = s_n$ **RK4**$(n{+}1,\ s_n) \cdot (\mathbb{I} + \mathbf{k}_3)$
else
  $\mathbf{k}_1 = s_n\, \mathscr{F}_m^M\ (0, s_n, ..., s_1)$
  $\mathbf{k}_2 = s_n\, \mathscr{F}_m^M (s_n/2, s_n, ..., s_1) \cdot (\mathbb{I} + \mathbf{k}_1/2)$
  $\mathbf{k}_3 = s_n\, \mathscr{F}_m^M (s_n/2, s_n, ..., s_1) \cdot (\mathbb{I} + \mathbf{k}_2/2)$
  $\mathbf{k}_4 = s_n\, \mathscr{F}_m^M (s_n, s_n, ..., s_1) \cdot (\mathbb{I} + \mathbf{k}_3)$
end if
return $\mathbb{I} + (\mathbf{k}_1 + 2\mathbf{k}_2 + 2\mathbf{k}_3 + \mathbf{k}_4)/6$

Because $\mathscr{F}_m^M(s_1, s_2, ..., s_m)$ is in Kraus representation form, the standard RK4 method for the innermost integral preserves trace, Hermiticity and positivity. By applying recursive RK4 schemes at each level of the nested integral, we ensure that these properties are also preserved for the total nested Runge-Kutta method. The computational cost of this scheme is of the order $\mathscr{O}(M^{M+1})$, which is considerably less than the computational cost of the high-dimensional midpoint method, which is of order $\mathscr{O}\left(M^{M+2}(\Delta t)^{M(1-M)}\right)$. Therefore, this method is preferred to the previous one.

In order to achieve higher than fourth-order approximation schemes, there exist other RK methods, both explicit and implicit. An explicit fifth-order scheme has been developed by Dormand and Prince [17], fifth- and sixth-order methods by Butcher [8][9], and a seventh-order method by Curtis [14]. Implicit higher order methods are NIRK [37], and Lobatto methods [38], which can be useful if higher accuracy is required. The algorithm we designed for RK4 can be easily adapted for higher order methods. The intermediate stages $\mathbf{k}_j$ can be replaced by the new stages and the order m can be increased.

5

Simulation Results

In this chapter, we present the results of the simulations of a linear Heisenberg model, using second-order and fourth-order methods. We explained the details of these models, and the coupling of the system to its environment using the Lindblad equation, in chapter 2. In chapter 3 we first derived the MPS notation for a wavefunction, and after that the vMPDO notation for a vectorised density operator. We also discussed the application quantum operators and the TEBD algorithm. In chapter 4 we reviewed several existing numerical methods for time evolution of the density operator and analysed the operator splitting method. We implemented a Trotter approximation for a second-order scheme and Duhamel's principle in combination with the high-dimensional midpoint method. All concepts of the previous chapters come together in this chapter when performing the simulations. The simulations are created in Python, using of the model developed by Ates [1] as the basis to build on. The Python model used in this thesis can be found at `https://github.com/ajdebruyn/BEP`.

The linear Heisenberg chain is described by the Heisenberg model in (2.19) applied to a linear spin chain of length L. We assume the system to be in absence of an external magnetic field ($h = 0$) and the interactions to be the same in all directions ($\Delta = 1$). Buča and Prosen [10] used exact numerical diagonalisation and Monte Carlo methods to analyse the XXZ-model between two leads, and we will compare our results to that study.

5.1. Second-Order Trotter Approximation

We consider a simulation with relatively large Δt and low χ, so the errors caused by these parameters are more obvious. In the appendix, figure B.3 shows a simulation with a smaller timestep, $\Delta t = 0.001$.

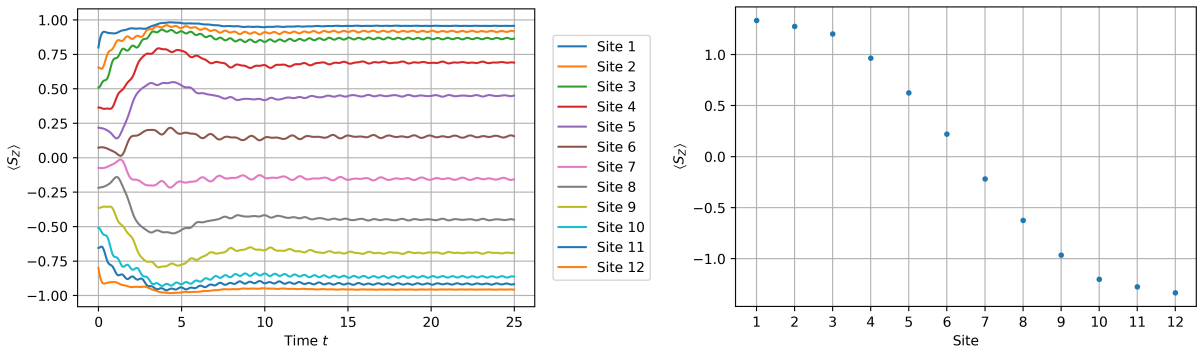

(a) Over the whole time integration period.

(b) For $t = 25$.

Figure 5.1: The expectation value of $\hat{S}_Z$ for each site. ($L = 12$, $\Delta t = 0.02$, $\chi = 15$, $\Delta = 1$)

In figure 5.1, we see the expectation value of $\hat{S}_Z$, or the magnetisation in the z-direction, of the XXZ-Heisenberg chain. Figure 5.1(a) demonstrates that the system settles around $t = 10$, but still shows small oscillations for larger t. We analyse the dependence on Δt and χ of these oscillations below. Figure 5.1(b) presents the magnetisation profile of the spin chain in non-equilibrium steady state. This result is similar to figure 2(h) in Buča and Prosen.

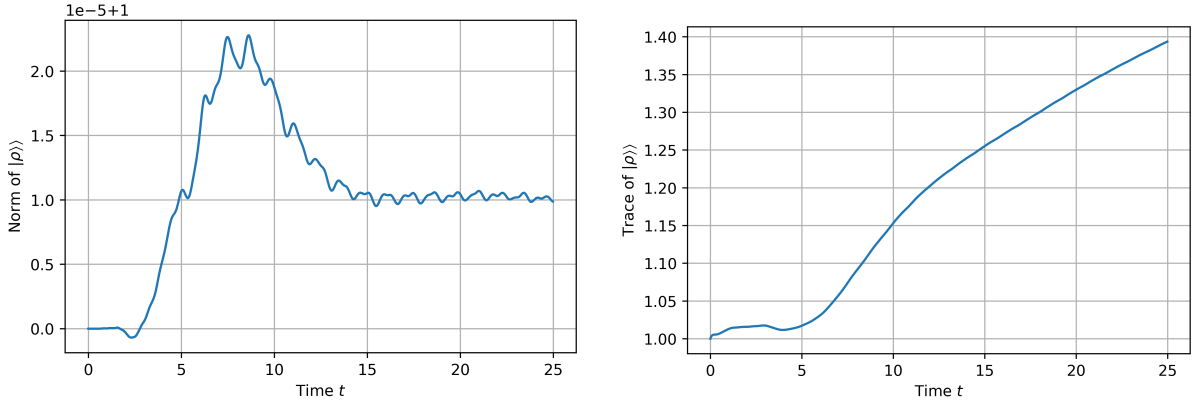

(a) The Euclidean norm of $|\hat{\rho}\rangle\rangle$.

(b) The trace of $|\hat{\rho}\rangle\rangle$.

Figure 5.2: The norm and trace of $|\hat{\rho}\rangle\rangle$ over time for the second-order Trotter approximation method. ($L = 12$, $\Delta t = 0.02$, $\chi = 15$, $\Delta = 1$)

Figure 5.2 shows the Euclidean norm and the trace of the vectorised $|\hat{\rho}\rangle\rangle$. The norm error peaks before $t = 10$ and settles on a value of order 10^{-5} after that. The trace starts increasing quickly after $t = 5$ and does not settle. In section 3.4 we discussed why the trace is in general not preserved. Below, we will further discuss the errors of the norm and the trace, respectively.

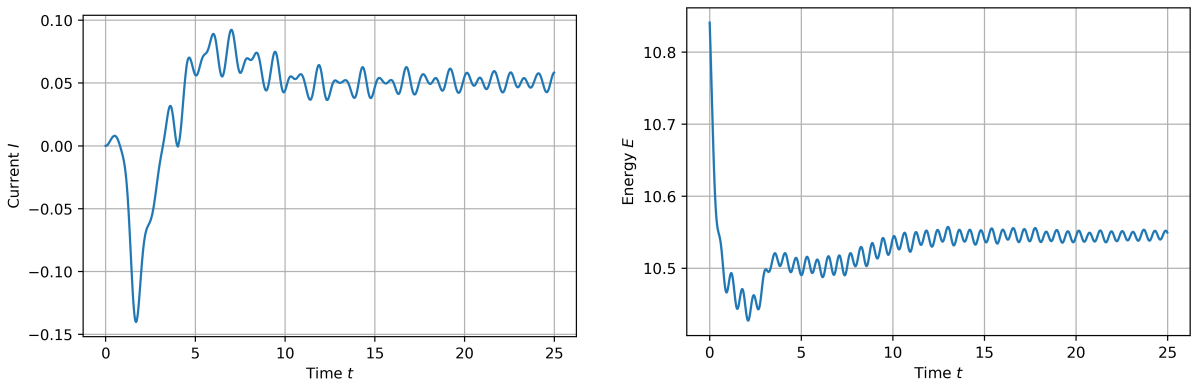

(a) The current I.

(b) The energy E.

Figure 5.3: The current I through the chain and the energy E of the chain over time for the second-order Trotter approximation method. ($L = 12$, $\Delta t = 0.02$, $\chi = 15$, $\Delta = 1$)

Figure 5.3 shows the spin transport, or current, through the chain an the energy of the chain. The current is approximately 0.05 for the non-equilibrium steady state, with fluctuations of order 10^{-2}. The energy of the chain falls between 10.5 and 10.6, and the oscillations have an amplitude of the same order. We shall see below that the amplitude of the oscillations of $\langle \hat{S}_Z \rangle$ are also of this order.

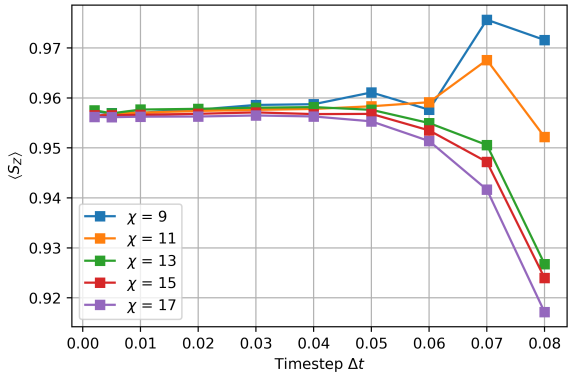

(a) $\langle \hat{S}_Z \rangle$ at site 1 as a function of the time step Δt for different bond dimensions χ.

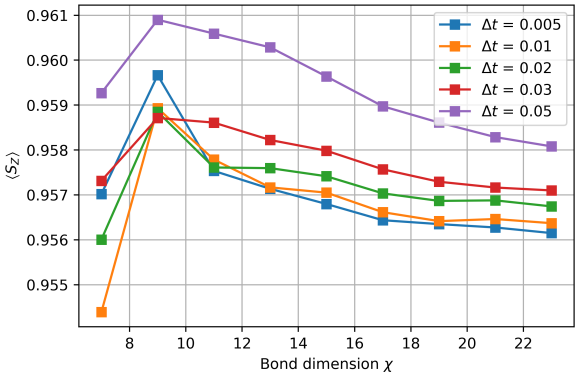

(b) $\langle \hat{S}_Z \rangle$ at site 1 as a function of the bond dimension χ for different time steps Δt.

Figure 5.4: The expectation value of S_Z at site 1 for different time steps Δt and bond dimensions χ for the second-order Trotter approximation method. ($L = 12$, $\Delta = 1$)

Figure 5.4 shows the magnetisation in the z-direction for site 1. The results for the other sites can be found in the appendix in figures B.4 and B.5. We see that the points converge when the time step Δt is small and the bond dimension χ is large. For increasing Δt, $\langle \hat{S}_Z \rangle$ increases as well, if χ is smaller than 19. For decreasing χ, $\langle \hat{S}_Z \rangle$ increases faster than for increasing Δt. It appears that the error of $\langle \hat{S}_Z \rangle$ depends primarily on χ, rather than Δt, especially for sufficiently small Δt and high χ. However, the other sites seem to behave slightly different compared to site 1. The Δt dependence of the error becomes stronger for sites further away from the edges and appears to be linear and takes over the χ dependence. All sites appear to become unstable for $\Delta t > 0.04$. Despite the increased error for the bulk sites and the instability for large Δt, the points do seem to converge for small Δt and high χ.

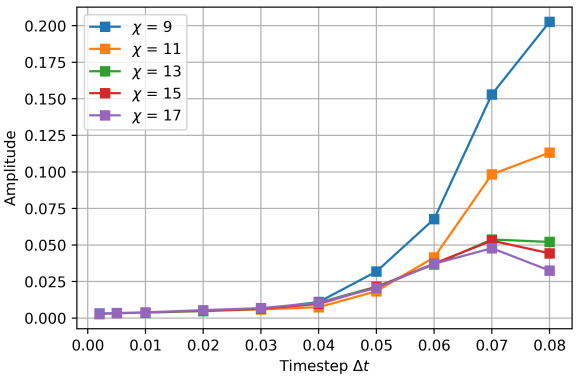

(a) The oscillations as a function of the time step Δt for different bond dimensions χ.

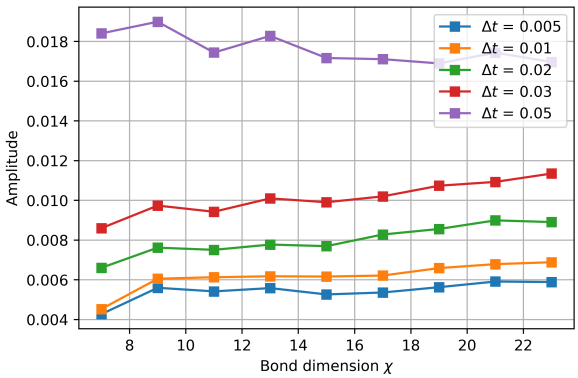

(b) The oscillations as a function of the bond dimension χ for different time steps Δt.

Figure 5.5: Amplitude of the oscillations of $\langle S_Z \rangle$ between $t = 24$ and $t = 25$ for different time steps Δt and bond dimensions χ for the second-order Trotter approximation method. ($L = 12$, $\Delta = 1$)

Figure 5.5 shows the amplitude of the oscillations in $\langle S_Z \rangle$ at $t = 25$, which are present in figure 5.1a. It is clear from this figure that the amplitude depends primarily on the time step Δt and less on the bond dimension χ. This is as expected because time integration methods are known to cause oscillations under certain conditions. If the time step is too large, numerical instability can arise, as we can see here. It is therefore important to choose an appropriate time step. The figure shows signs of instability for $\Delta t \geq 0.05$. We see in figure 5.5(a) that the amplitude decreases with the time step, so

the oscillations disappear for small enough Δt.

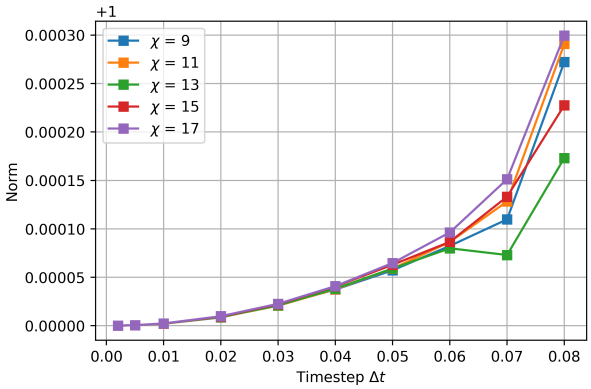

(a) The norm at at $t = 25$ as a function of the time step Δt for different bond dimensions χ.

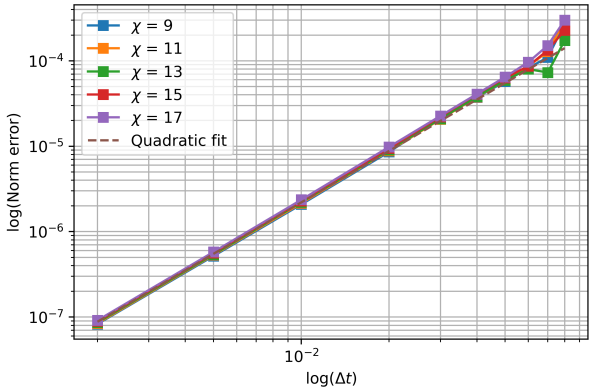

(b) Log-log plot of the norm error at $t = 25$ as a function of the time step Δt for different bond dimensions χ.

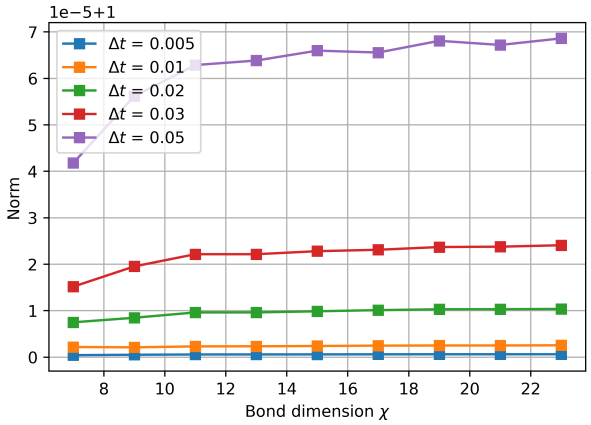

(c) The norm at at $t = 25$ as a function of the bond dimension χ for different time steps Δt.

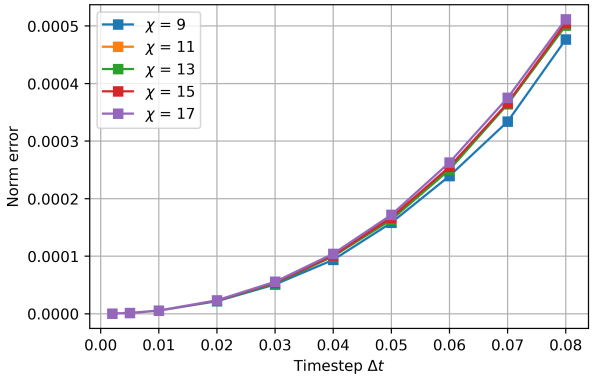

(d) The maximum norm error over all t as a function of the time step Δt for different bond dimensions χ.

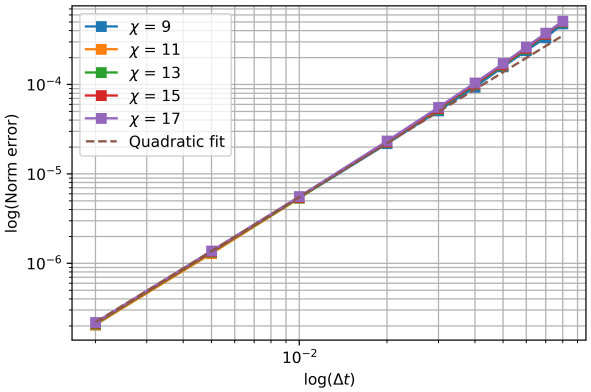

(e) Log-log plot of the maximum norm error over all t as a function of the time step Δt for different bond dimensions χ.

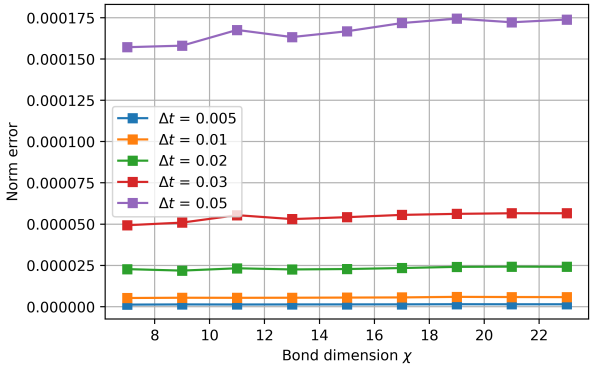

(f) The maximum norm error over all t as a function of the bond dimension χ for different time steps Δt. ($L = 12$, $\Delta = 1$)

Figure 5.6: The Euclidean norm of $|\hat{\rho}\rangle\rangle$ at $t = 25$ for different time steps Δt and bond dimensions χ for the second-order Trotter approximation method. There are two types of errors considering the norm; 1. The error at t = 25 for the approximately non-equilibrium steady state solution, see (a-c). 2. The maximum error over all t, see (d-f).

Figure 5.6 shows the Euclidean norm and the corresponding error of $|\hat{\rho}\rangle\rangle$. The error of the norm both at $t = 25$ and of the maximum over all t is quadratic with the time step Δt, as is evident from the log-log plots. The norm (error) is not highly dependent on the bond dimension χ, but there seems to be an almost negligible increase in the norm for increasing χ. The figures show signs of instability

for $\Delta t > 0.05$.

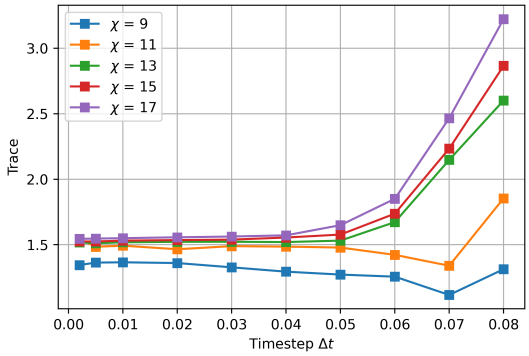

(a) The trace at $t = 25$ as a function of the time step Δt for different bond dimensions χ.

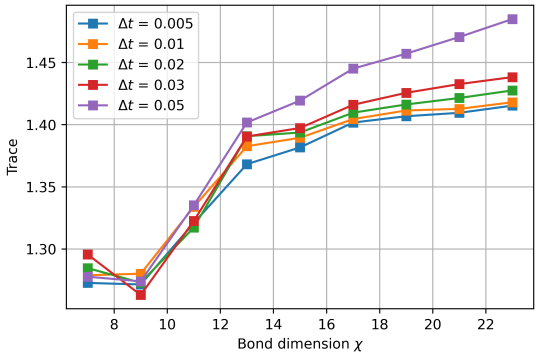

(b) The trace at $t = 25$ as a function of the bond dimension χ for different time steps Δt.

Figure 5.7: The trace of $|\hat{\rho}\rangle\rangle$ at $t = 25$ for different time steps Δt and bond dimensions χ for the second-order Trotter approximation method. ($L = 12$, $\Delta = 1$)

Figure 5.7 shows the trace of $|\hat{\rho}\rangle\rangle$, which is in general, as stated in section 3.4, not preserved. This is exactly what our results show, as the trace converges to a value close to 1.5. For $\Delta t \leq 0.4$, the convergence occurs quickly for decreasing Δt. Interestingly, the trace increases approximately linearly with χ, for $\chi \geq 13$.

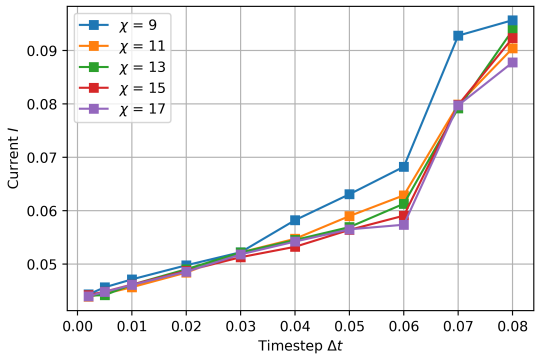

(a) The current I at $t = 25$ as a function of the time step Δt for different bond dimensions χ.

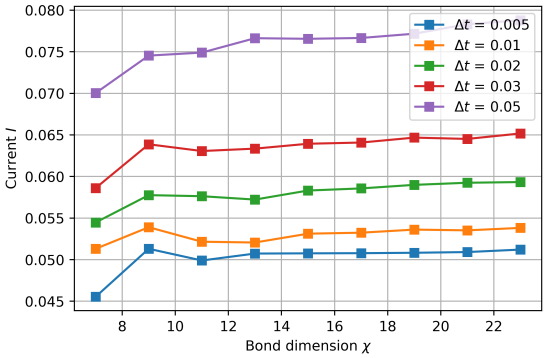

(b) The current I at $t = 25$ as a function of the bond dimension χ for different time steps Δt.

Figure 5.8: The current I through the chain at $t = 25$ for different time steps Δt and bond dimensions χ for the second-order Trotter approximation method. ($L = 12$, $\Delta = 1$)

Figure 5.8 shows the current through the chain for the non-equilibrium steady state. The Δt dependent error is clearly linear for small Δt (< 0.04). The current converges to a value between 0.4 and 0.5 for all $\chi \geq 15$. Similar to the previous figures, there appears to be instability for $\Delta t \geq 0.05$.

5.2. Third-Order High-Dimensional Midpoint Method

In the previous section we analysed the results of the second-order Trotter approximation method. In this section we analyse the simulation using the third-order high-dimensional midpoint method as described in section 4.4. We use the same time step Δt and bond dimension as in the previous section.

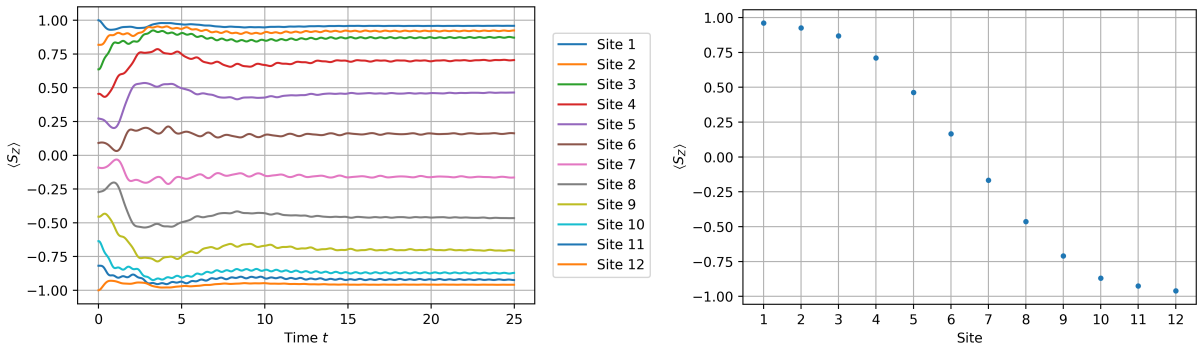

(a) Over the whole time integration period.

(b) For $t = 25$.

Figure 5.9: The expectation value of $\hat{S}_Z$ for each site for the third-order high-dimensional midpoint method. ($L = 12$, $\Delta t = 0.02$, $\chi = 15$, $\Delta = 1$)

In figure 5.1, we see the magnetisation in the z-direction of the XXZ-Heisenberg chain. These results are very similar to the second-order plots. Figure 5.1(a) shows oscillations, which are smaller than before. We analyse the dependence on Δt and χ of the oscillations below. Figure 5.1(b) presents the magnetization profile of the spin chain in non-equilibrium steady state, which is approximately the same as before.

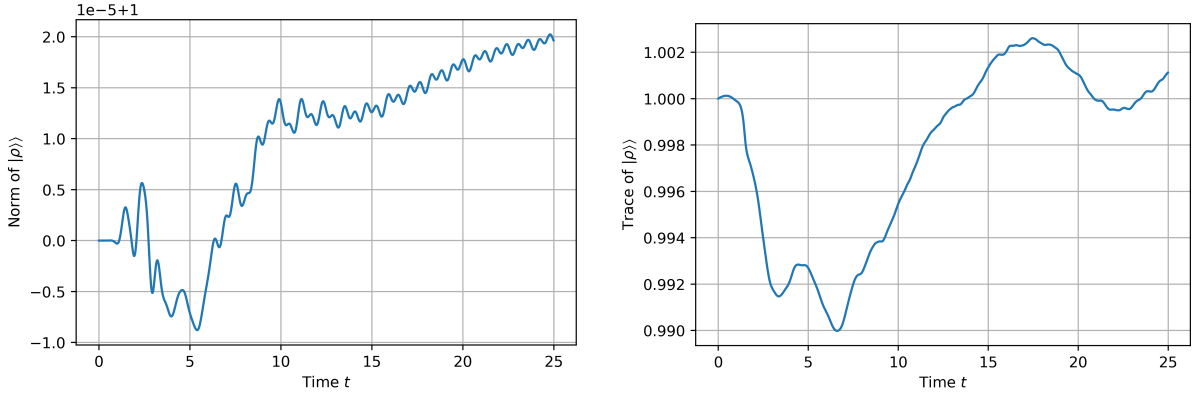

(a) The Euclidean norm of $|\hat{\rho}\rangle\rangle$.

(b) The trace of $|\hat{\rho}\rangle\rangle$.

Figure 5.10: The norm and trace of $|\hat{\rho}\rangle\rangle$ over time for the third-order high-dimensional midpoint method. ($L = 12$, $\Delta t = 0.02$, $\chi = 15$, $\Delta = 1$)

Figure 5.10 shows the Euclidean norm and the trace of the vectorized $|\hat{\rho}\rangle\rangle$. The norm error steadily increases for $t > 15$, whereas before the error peaked before $t = 10$ and settled after that. The trace deviates from one, but not as much as before. For the second-order approximation the trace increased steadily without settling, which is clearly different for the third-order method, which stays closer to the real value one. Below, we will further discuss the errors of the norm and the trace, respectively.

Figure 5.11 shows the spin transport, or current, through the chain an the energy of the chain.

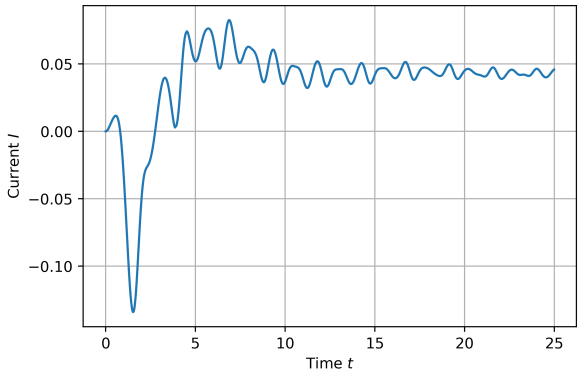

(a) The current I.

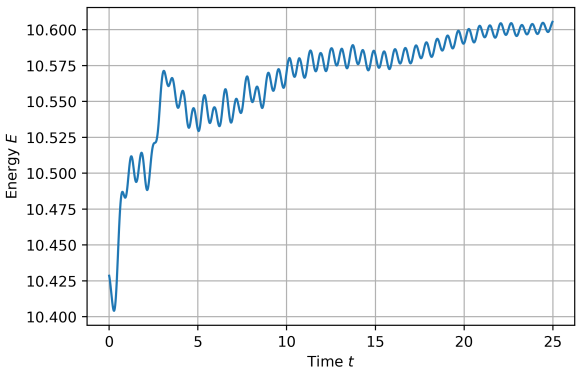

(b) The energy E.

Figure 5.11: The current I through the chain and the energy E of the chain over time for the third-order high-dimensional midpoint method. ($L = 12$, $\Delta t = 0.02$, $\chi = 15$, $\Delta = 1$)

The current falls between 0.04 and 0.05 for the non-equilibrium steady state, which is 0.005 less than for the second-order approximation. The energy of the chain is approximately 10.6, which is 0.05 more than before, and the amplitude of the oscillations is smaller as well.

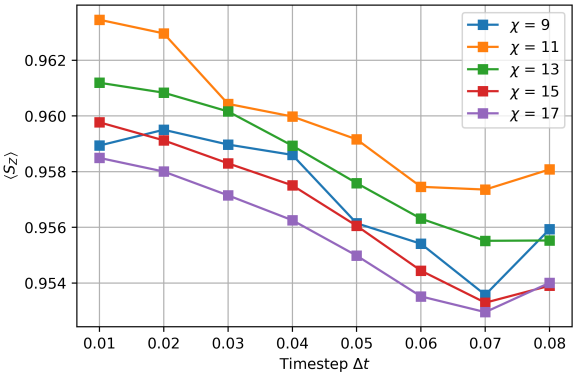

(a) $\langle \hat{S}_Z \rangle$ at site 1 as a function of the time step Δt for different bond dimensions χ.

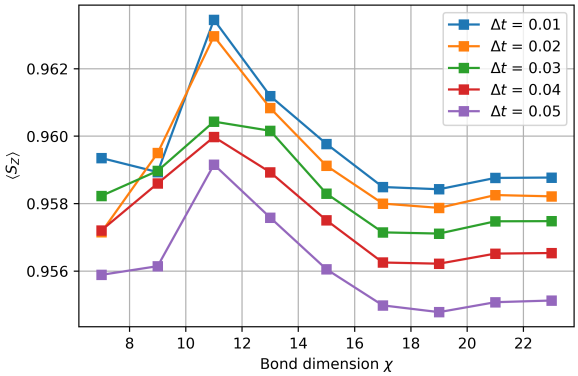

(b) $\langle \hat{S}_Z \rangle$ at site 1 as a function of the bond dimension χ for different time steps Δt.

Figure 5.12: The expectation value of S_Z at site 1 for different time steps Δt and bond dimensions χ for the third-order high-dimensional midpoint method. ($L = 12$, $\Delta = 1$)

Figure 5.4 shows the magnetisation in the z-direction for site 1. The results for the other sites can be found in the appendix in figures B.6 and B.7. The shape of the lines in this figure are completely different than before. We see that the points converge less quickly than for the second-order method, and to a slightly higher value. For increasing Δt, $\langle \hat{S}_Z \rangle$ decreases. For decreasing χ, $\langle \hat{S}_Z \rangle$ first decreases and then increases. The error is mainly determined by our choice for Δt, as long as $\chi \geq 15$. Most of the other sites seem to behave similarly compared to site 1. Despite the larger error, the points do seem to converge, but to slightly higher values.

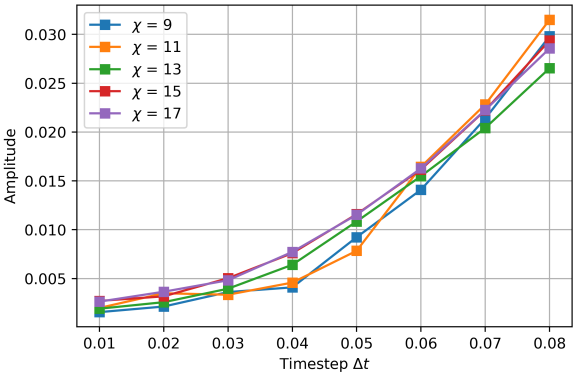

(a) The oscillations as a function of the time step Δt for different bond dimensions χ.

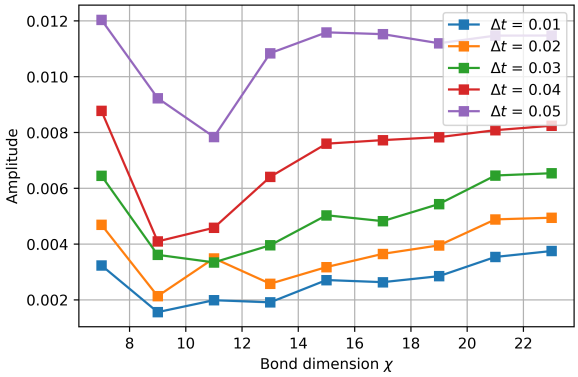

(b) The oscillations as a function of the bond dimension χ for different time steps Δt.

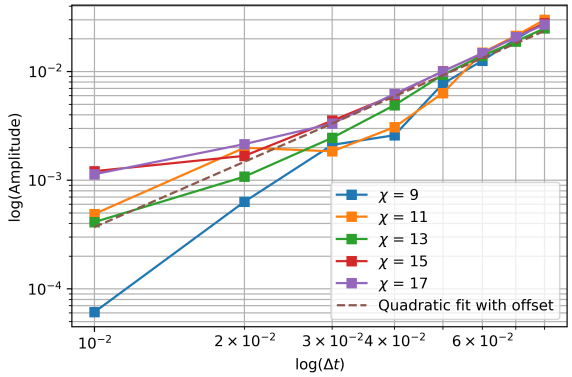

(c) Log-log plot of the oscillations as a function of the time step Δt for different bond dimensions χ.

Figure 5.13: Amplitude of the oscillations of $\langle S_Z \rangle$ between $t = 24$ and $t = 25$ for different time steps Δt and bond dimensions χ, for the third-order high-dimensional midpoint method. ($L = 12$, $\Delta = 1$)

Figure 5.13 shows the amplitude of the oscillations in $\langle S_Z \rangle$ at $t = 25$, which are present in figure 5.9a. It is clear from this figure that the amplitude depends primarily on the time step Δt, which was also the case for the second-order method. However the amplitudes for the third-order method are smaller than for the second-order method. The amplitude appears to be of order $\mathcal{O}(\Delta t^2)$, however, there also is an offset of approximately 0.002. Therefore, the oscillations will probably not fully disappear for small Δt.

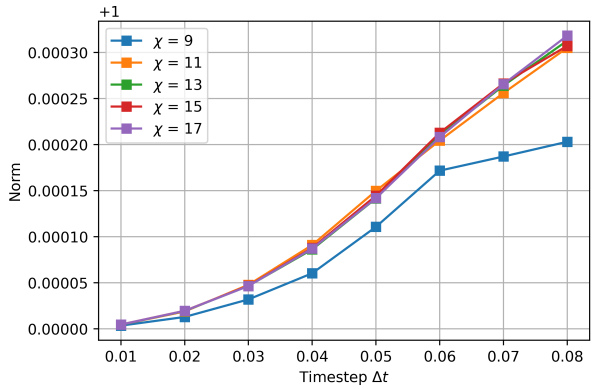

(a) The norm at at $t = 25$ as a function of the time step Δt for different bond dimensions χ.

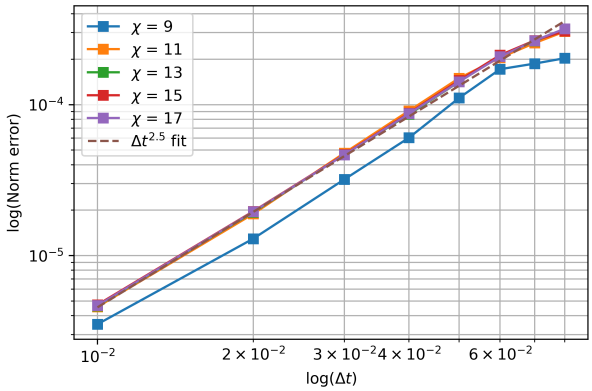

(b) Log-log plot of the norm error at $t = 25$ as a function of the time step Δt for different bond dimensions χ.

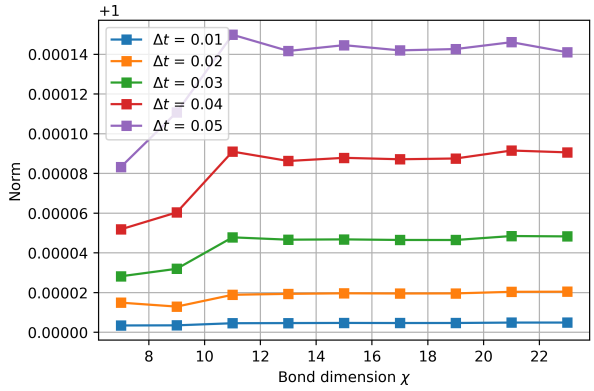

(c) The norm at at $t = 25$ as a function of the bond dimension χ for different time steps Δt.

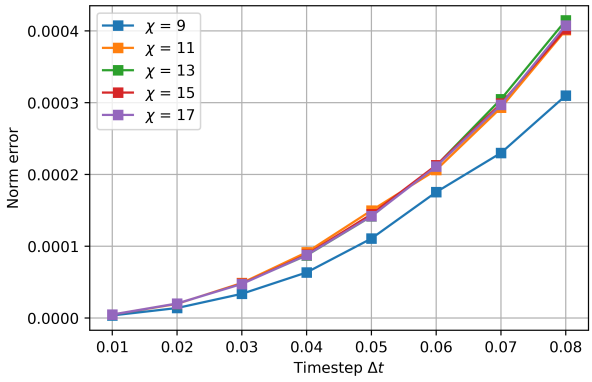

(d) The maximum norm error over all t as a function of the time step Δt for different bond dimensions χ.

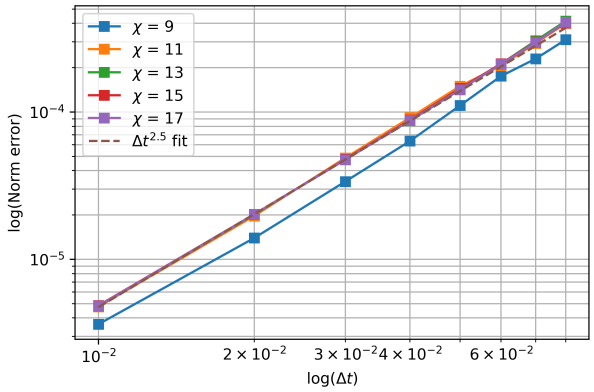

(e) Log-log plot of the maximum norm error over all t as a function of the time step Δt for different bond dimensions χ.

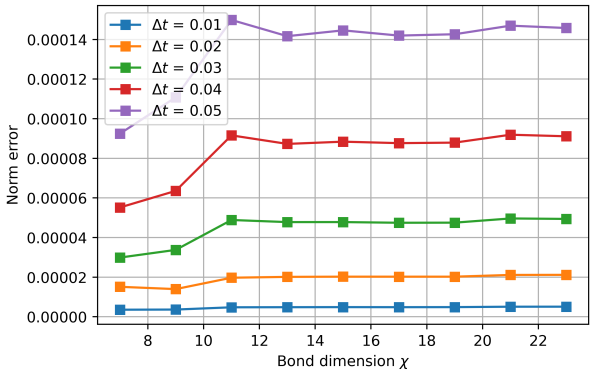

(f) The maximum norm error over all t as a function of the bond dimension χ for different time steps Δt.

Figure 5.14: The Euclidean norm of $|\hat{\rho}\rangle\rangle$ at $t = 25$ for different time steps Δt and bond dimensions χ for the third-order high-dimensional midpoint method. There are two types of errors considering the norm; 1. The error at t = 25 for the approximately non-equilibrium steady state solution, see (a-c). 2. The maximum error over all t, see (d-f). ($L = 12$, $\Delta = 1$)

Figure 5.14 shows the Euclidean norm and the corresponding error of $|\hat{\rho}\rangle\rangle$. These results are very similar to the results obtained with the second-order method. The error of the norm both at $t = 25$ and of the maximum over all t is of the order $\mathcal{O}(\Delta t^{2.5})$, as is evident from the log-log plots. Similarly as before, the norm (error) is not highly dependent on the bond dimension χ.

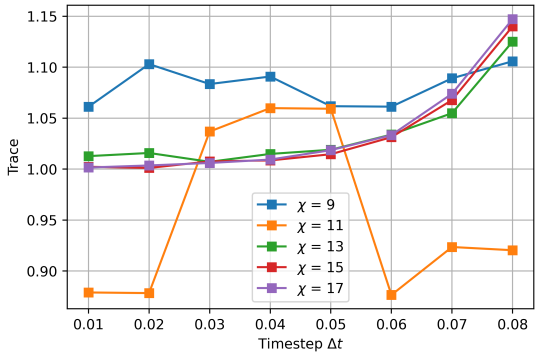

(a) The trace at $t = 25$ as a function of the time step Δt for different bond dimensions χ.

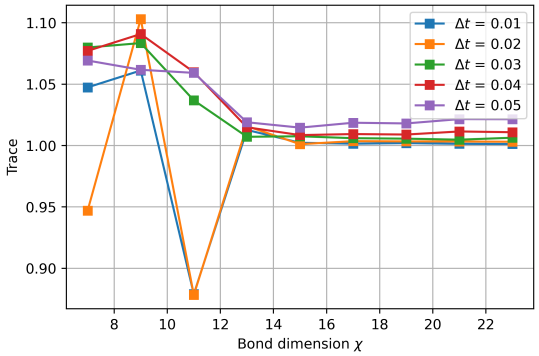

(b) The trace at $t = 25$ as a function of the bond dimension χ for different time steps Δt.

Figure 5.15: The trace of $|\hat{\rho}\rangle\rangle$ at $t = 25$ for different time steps Δt and bond dimensions χ for the third-order high-dimensional midpoint method. ($L = 12$, $\Delta = 1$)

Figure 5.15 shows the trace of $|\hat{\rho}\rangle\rangle$, which is in general, as stated in section 3.4, not preserved, which was also the case for the second-order method. However, these results show that for the third-order method the trace is preserved, for the right choice of Δt and χ. The figure shows that the bond dimension should be at least 15, such that the trace converges to one in Δt.

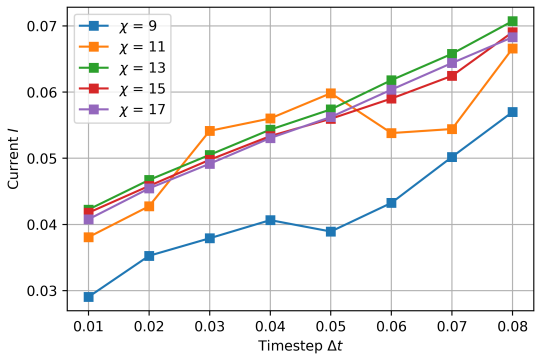

(a) The current I at $t = 25$ as a function of the time step Δt for different bond dimensions χ.

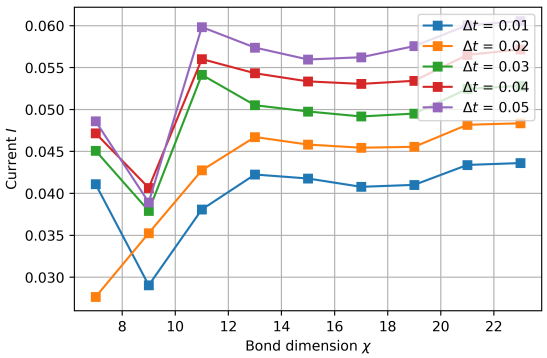

(b) The current I at $t = 25$ as a function of the bond dimension χ for different time steps Δt.

Figure 5.16: The current I through the chain at $t = 25$ for different time steps Δt and bond dimensions χ for the third-order high-dimensional midpoint method. ($L = 12$, $\Delta = 1$)

Figure 5.16 shows the current through the chain for the non-equilibrium steady state. These results are similar to the second-order method, especially for $\chi \geq 13$ and $t \leq 0.06$. The current is linear in Δt, just as before.

6

Conclusion

In this thesis we successfully implemented the Lindblad equation for MPS using operator splitting methods. A second-order scheme was developed by applying a Trotter approximation and a thrid-order scheme by introducing Duhamel's principle and applying the high-dimensional midpoint method. We simulated an XXZ-Heisenberg chain and the CISS effect, using vectorised MPDO's and the TEBD algorithm. The non-equilibrium steady state is of particular interest to us, as it provides information about the long term dynamics of the system.

The simulation of the Heisenberg model showed that the magnetisation profile of the chain in non-equilibrium steady state is similar to the study of Buča and Prosen [10]. The amplitude of the oscillations of the magnetization of sites in the bulk appeared to be linear with the time step Δt, which would suggest a first-order error, instead of a second or third-order error we expected. The amplitude decreased slowly for higher bond dimension χ, but this was dominated by the Δt dependence. There was no correlation visible between Δt and χ. Therefore, Δt mainly determines the size of the error in the magnetisation.

For the second-order method, the relative error of the norm of the vMPDO is of the order 10^{-5}, whereas the relative error of the trace is of the order 10^{0}. Recall from section 3.4 that MPS preserves norm and not trace. Therefore, these results are not surprising. On top of that, figure 5.6 shows that the time evolution scheme of the norm is indeed of order $\mathcal{O}(\Delta t^2)$. For the third-order method, the norm error is of the order 10^{-4}, one order larger than the second-order method, but the relative error of the trace is of order 10^{-2} for small enough Δt and large enough χ, which is a major improvement.

Interesting to note is that the norm error increases slightly for higher χ. This is explained by the fact that the error in the norm depending directly on χ is very small, but that the increasing complexity for the higher bond dimensions causes increasing errors. For the second-order method, the error in the trace includes a constant between 0.5 and 0.6, which does not exist for the third-order method.

The current through the chain is linearly dependent on the stepsize Δt, converging to a value in around 0.04, depending on the method. It is very intersting that the choice for Δt has a significant effect on the measured current, as the current depends linearly on Δt. The error depending on χ is similar to the norm error.

For a time step Δt of 0.05 or larger, the time-evolution becomes numerically unstable. Some properties, such as the oscillations in $\langle \hat{S}_Z \rangle$ and the current appear to be linearly dependent on Δt, whereas the norm error is of the order $\mathcal{O}(\Delta t^2)$ and $\mathcal{O}(\Delta t^2)$, depending on the method. Most properties did not show a strong dependency on the bond dimension χ, especially for $\chi \geq 15$. We therefore conclude that the choice for Δt mainly determines the accuracy of the simulation.

The second-order Trotter approximation method is more accurate for the norm and magnetisation profile. The third-order high-dimensional midpoint method is significantly more accurate

for the trace and has smaller oscillation amplitudes. The third-order method did not show any third-order behaviour, but rather $\mathcal{O}(\Delta t^{2.5})$ for the norm, and quadratic order for the oscillation amplitudes. This result raises doubts about the actual order of the method. Nevertheless, we recommend the third-order method, as it preserves trace, and performs (almost) as well as the second-order method for the other properties.

An interesting extension of the model is to increase the order of the time-evolution scheme. As mentioned before, we proposed a nested Runge-Kutta method, which can even be easily adapted for higher order schemes by swapping RK4 with another RK method. The current algorithm is not very efficient, which will not be a problem for RK4, but can become problematic when applying higher order Runge-Kutta methods. A more efficient algorithm should be developed when increasing the approximation order.

For this thesis, there was no opportunity to make use of super computers, so the possible chain lengths, time steps, bond dimensions and approximation orders we could consider were limited. It would be very interesting to extend this research by studying longer chains, smaller time steps, higher bond dimensions and higher approximation orders.

In this thesis, we assumed that the interactions are local, allowing us to split the Hamiltonian into smaller pieces for efficient time-evolution. Not all quantum systems have these local interactions. Instead of splitting the Hamiltonian, an MPDO of the time-evolution operator could be implemented. Jaschke et al. [33] and Hubig et al. [32] provide a solid basis on MPO's.

References

[1] M. Ates. [manuscript in preparation]. 2024.

[2] H. Bethe. Zur Theorie der Metalle. I. Eigenwerte und Eigenfunktionen der linearen Atomkette. *Zeitschrift für Physik*, 71:205–226, 1931.

[3] B. Bidégaray, A. Bourgeade, and D. Reignier. Introducing Physical Relaxation Terms in Bloch Equations. *Journal of Computational Physics*, 170:603–613, 2001.

[4] B.P. Bloom, Y. Paltiel, R. Naaman, and D.H. Waldeck. Chiral induced spin selectivity. *Chem. Rev.*, 124:1950–1991, 2024.

[5] L. Bonnes and A.M. Läuchli. Superoperators vs. trajectories for matrix product state simulations of open quantum system: A case study. 2014.

[6] C.J. Brasil, F.F. Fanchini, and R. de Jesus Napolitano. A simple derivation of the lindblad equation. *Rev. Bras. Ensino Fís.*, 35:1–11, 2013.

[7] H.-P. Breuer and F. Petruccione. *The theory of open quantum systems*. Oxford university press, Oxford, first edition, 2002.

[8] J.C. Butcher. On runge-kutta processes of high order. *Journal of the Australian Mathematical Society*, 4:179–194, 1964.

[9] J.C. Butcher. On the attainable order of runge-kutta methods. *Mathematics of computation*, 19: 408–417, 1965.

[10] B. Buča and T. Prosen. A note on symmetry reductions of the Lindblad equation: transport in constrained open spin chains. *New J. Phys.*, 14:073007, 2012.

[11] Y. Cao and J. Lu. Structure-preserving numerical schemes for lindblad equations, [Unpublished manuscript]. 2021.

[12] A.M. Childs, Y. Su, M.C. Tran, N. Wiebe, and S. Zhu. Theory of Trotter error with commutator scaling. *Phys. Rev. X*, 11:011020, 2021.

[13] S.R. Clark, J. Prior, M.J. Hartmann, D. Jaksch, and M.B. Plenio. Exact matrix product solutions in the Heisenberg picture of an open quantum spin chain. *New J. Phys.*, 12:025005, 2010.

[14] A.R. Curtis. An eighth order runge-kutta process with eleven function evaluations per step. *Numerische Mathematik*, 16:268–277, 1970.

[15] A.J. Daley, C.Kollath, U.Schollwöck, and G.Vidal. Time-dependent density-matrix renormalization-group using adaptive effective Hilbert spaces . *J. Stat. Mech.*, 2004, 2004.

[16] M. Van Damme, R. Vanhove, J. Haegeman, F. Verstraete, and L. Vanderstraeten. Efficient MPS methods for extracting spectral information on rings and cylinders. *Phys. Rev. B*, 104:115142, 2021.

[17] J.R. Dormand and P.J. Prince. A family of embedded runge-kutta formulae. *Journal of Computational and Applied Mathematics*, 6:19–26, 1980.

[18] J. Eisert, M. Cramer, and M.B. Plenio. Colloquium: Area laws for the entanglement entropy. *Rev. Mod. Phys.*, 82:277, 2010.

[19] F. Evers, A. Aharony, N. Bar-Gill, O. Entin-Wohlman, P. Hedegård, O. Hod, P. Jelinek, G. Kamieniarz, M. Lemeshko, K. Michaeli, V. Mujica, R. Naaman, Y. Paltiel, S. Refaely-Abramson, O. Tal, J. Thijssen, M. Thoss, J.M. van Ruitenbeek, L. Venkataraman, D.H. Waldeck, B. Yan, and L. Kronik. Theory of chirality induced spin selectivity: Progress and challenges. *Advanced Materials*, 34:2106629, 2022.

[20] J. Fransson. Chirality-induced spin selectivity: The role of electron correlations. *The Journal of Physical Chemistry Letters*, 10:6967–7305, 2019.

[21] M. Geyer, R. Gutierrez, V. Mujica, and G. Cuniberti. Chirality-induced spin selectivity in a coarse-grained tight-binding model for helicene. *J. Phys. Chem. C*, 123:27230–41, 2019.

[22] M. Geyer, R. Gutierrez, and G. Cuniberti. Effective Hamiltonian model for helically constrained quantum systems within adiabatic perturbation theory: application to the Chirality-Induced Spin Selectivity (CISS) effect. *J. Chem. Phys.*, 152:214105, 2020.

[23] T. Giamarchi and C. Lhuillier. Phase diagrams of the two-dimensional Hubbard and t-J models by a variational Monte Carlo method. *Phys. Rev. B*, 43:12943–51, 1991.

[24] A. Gilchrist, D.R. Terno, and C.J. Wood. Vectorization of quantum operations and its use, [Unpublished manuscript]. 2011.

[25] D.J. Griffiths and D.F. Schroeter. *Introduction to Quantum Mechanics*. Cambridge University Press, third edition, 2018.

[26] B. Göhler, V. Hamelbeck, T.Z. Markus, M. Kettner, G.F. Hanne, Z. Vager, R. Naaman, and H Zacharias. Spin selectivity in electron transmission through self-assembled monolayers of double-stranded DNA. *Science*, 331:894–897, 2011.

[27] M.B. Hastings. An area law for one dimensional quantum systems. *J. Stat. Mech.*, 08:P08024, 2007.

[28] W. Heisenberg. Zur Theorie der Ferromagnetismus. *Z. Phys.*, 49:619–636, 1928.

[29] M.F. Herman, E.J. Bruskin, and B.J. Berne. On path integral monte carlo simulations. *J. Chem. Phys.*, 76:5150–5155, 1982.

[30] R.A. Horn and C.R. Johnson. *Matrix analysis*. Cambridge University Press, second edition, 1994.

[31] J. Hubbard. Electron correlations in narrow energy bands. *Proc. R. Soc. A.*, 276:237–257, 1963.

[32] C. Hubig, I.P. McCulloch, and U. Schollwöck. Generic construction of efficient matrix product operators. *Phys. Rev. B*, 95:035129, 2017.

[33] D. Jaschke, S. Montangero, and L.D. Carr. One-dimensional many-body entangled open quantum systems with tensor network methods. *Quantum Sci. Technol.*, 4:013001, 2019.

[34] P. Jordan and E. Wigner. Über das Paulische Äquivalenzverbot. *Zeitschrift für Physik*, 47(9): 631–651, 1928.

[35] M. Karbach and G. Müller. Introduction to the Bethe ansatz I. *Computers in Physics*, 11:36–43, 1997.

[36] M. Karbach, K. Hu, and G. Müller. Introduction to the Bethe ansatz II. *Computers in Physics*, 12: 565–573, 1998.

[37] G.Y. Kulikov and S.K. Shindin. Adaptive nested implicit runge–kutta formulas of gauss type. *Applied Numerical Mathematics*, 59:707–722, 2009.

[38] O.J. Laurent. Lobatto methods. In: B. Engquist. *Encyclopedia of Applied and Computational Mathematics*, page 817–826, 2015.

[39] X. Li and C. Wang. Simulating Markovian open quantum systems using higher-order series expansion. 2023.

[40] S. Liang. Monte Carlo calculations of the correlation functions for Heisenberg spin chains at T=0. *Phys. Rev. Lett.*, 64:1597–1600, 1990.

[41] G. Lindblad. On the generators of quantum dynamical semigroups. *Commun.Math. Phys.*, 48: 119–130, 1976.

[42] E.Y. Loh Jr., J.E. Gubernatis, R.T. Scalettar, S.R. White, D.J. Scalapino, and R.L. Sugar. Sign problem in the numerical simulation of many-electron systems. *Phys. Rev. B*, 41:9301, 1990.

[43] H. Lu, C. Xiao, R. Song, T. Li, A.E. Maughan, A. Levin, R. Brunecky, J. J. Berry, D.B. Mitzi, V. Blum, and M.C. Beard. Highly distorted chiral two-dimensional tin iodide perovskites for spin polarized charge transport. *J. Am. Chem. Soc.*, 142:13030–40, 2020.

[44] E. Mascarenhas, H. Flayac, and V. Savona. Matrix-product-operator approach to the nonequilibrium steady state of driven-dissipative quantum arrays. *Phys. Rev. A*, 92:022116, 2015.

[45] I.P. McCulloch. From density-matrix renormalization group to matrix product states. *J. Stat. Mech.*, 2007:10014, 2007.

[46] C. Moler and C. Van Loan. Nineteen dubious ways to compute the exponential of a matrix, twenty-five years later. *SIAM Review*, 45(1), 2003.

[47] S. Naskar, V. Mujica, and C. Herrmann*. Chiral-induced spin selectivity and non-equilibrium spin accumulation in molecules and interfaces: A first-principles study. *J. Phys. Chem. Lett.*, 14: 694–701, 2023.

[48] M. Nielsen and I. Chuang. *Quantum computation and quantum information*. Cambridge University Press, 2000.

[49] L. Oppenheim and K. Michaeli. Incoherent chiral-induced spin selectivity. 2022.

[50] R. Orús. A practical introduction to tensor networks: Matrix product states and projected entangled pair states. *Annals of Physics*, 349:117–158, 2014.

[51] R. Penrose. Applications of negative dimensional tensors. in: D.j.a. welsh. *Combinatorial Mathematics and its Applications*, page 221–244, 1971.

[52] D.H. Waldeck R. Naaman. Chiral-induced spin selectivity effect. *J. Phys. Chem. Lett.*, 3:2178–2187, 2012.

[53] K. Ray, S.P. Ananthavel, D.H. Waldeck, and R. Naaman. Asymmetric scattering of polarized electrons by organized organic films of chiral molecule. *Science*, 283:814–816, 1999.

[54] A.G. Redfield. The theory of relaxation processes. *Advances in Magnetic and Optical Resonance*, 1:1–32, 1965.

[55] P.J. Reynolds, J. Tobochnik, and H. Gould. Diffusion quantum monte carlo. *Comput. Phys.*, 4: 662–668, 1990.

[56] M. Riesch and C. Jirauschek. Analyzing the positivity preservation of numerical methods for the Liouville-von Neumann equation. *Journal of Computational Physics*, 380:290–296, 2019.

[57] J.A.D. Sandretto and A. Chapoutot. Validated explicit and implicit runge-kutta methods. *Reliable Computing*, 22:56–77, 2016.

[58] U. Schollwöck. The density-matrix renormalization group. *Rev. Mod. Phys.*, 77, 2004.

[59] U. Schollwöck. The density-matrix renormalization group in the age of matrix product states. *Annals of Physics*, 326:96–192, 2011.

[60] E. Schrödinger. An undulatory review of the mechanics of atoms and molecules. *The Physical Review*, 28(6):1049–1070, 1926.

[61] J. Steinbach, B.M. Garraway, and P.L. Knight. High-order unraveling of master equations for dissipative evolution. *Phys. Rev. A*, 51(4):3302–3308, 1995.

[62] M. Suzuki. General theory of fractal path integrals with applications to many-body theories and statistical physics. *J. Math. Phys.*, 32(2):400–407, 1991.

[63] J.M. Thijssen. *Computational Physics [Unpublished].* Cambridge University Press, third edition.

[64] J.M. Thijssen. *Computational Physics.* Cambridge University Press, second edition, 2007.

[65] F. Verstraete and J.I. Cirac. Renormalization algorithms for quantum-many body systems in two and higher dimensions. 2004.

[66] F. Verstraete and J.I. Cirac. Matrix product states represent ground states faithfully. *Physical Review B*, 73:094423, 2006.

[67] F. Verstraete, J.J. García-Ripoll, and J.I. Cirac. Matrix product density operators: Simulation of finite-temperature and dissipative systems. *Phys. Rev. Lett.*, 93(20):207204, 2004.

[68] F. Verstraete, D. Porras, and J.I. Cirac. DMRG and periodic boundary conditions: a quantum information perspective. *Phys. Rev. Lett.*, 93:227205, 2004.

[69] F. Verstraete, V. Murg, and J.I. Cirac. Matrix product states, projected entangled pair states, and variational renormalization group methods for quantum spin systems. *Advances in Physics*, 57: 143–224, 2008.

[70] G. Vidal. Efficient simulation of one-dimensional quantum many-body systems. *Phys. Rev. Lett.*, 93:040502, 2004.

[71] A.H. Werner, D. Jaschke, P. Silvi, M. Kliesch, T. Calarco, J. Eisert, and S. Montangero. Positive Tensor Network Approach for Simulating Open Quantum Many-Body Systems. *Phys. Rev. Lett.*, 116:237201, 2016.

[72] S.R. White. Density matrix formulation for quantum renormalization groups. *Phys. Rev. Lett.*, 69:2863, 1992.

[73] S.R. White and R.M. Noack. Real-space quantum renormalization groups. *Phys. Rev. Lett.*, 68: 3487, 1992.

[74] M.M. Wilde. *Quantum Information Theory*. Cambridge University Press, second edition, 2017.

[75] R. Winkler. *Spin–Orbit Coupling Effects in Two-Dimensional Electron and Hole Systems*. Springer, first edition, 2003.

[76] S. Wolff, A. Sheikhan, and C. Kollath. Numerical evaluation of two-time correlation functions in open quantum systems with matrix product state methods: a comparison. *SciPost Physics Core*, 3:010, 2020.

A

Violation of Positive Semi-Definiteness for the Euler Method

We will present an example in which the Euler method does not preserve the positive semi-definiteness of the density operator.

Consider the Lindblad equation:

$$\frac{d\hat{\rho}}{dt} = -\mathrm{i}[\hat{H},\hat{\rho}] + \sum_k \left(\hat{L}_k\hat{\rho}\hat{L}_k^\dagger - \frac{1}{2}\{\hat{L}_k^\dagger\hat{L}_k,\hat{\rho}\}\right)$$

We will use the explicit Euler method to discretise this equation:

$$\hat{\rho}(t+\Delta t) = \hat{\rho}(t) + \Delta t\left(-\mathrm{i}[\hat{H},\hat{\rho}(t)] + \sum_k \left(\hat{L}_k\hat{\rho}(t)\hat{L}_k^\dagger - \frac{1}{2}\{\hat{L}_k^\dagger\hat{L}_k,\hat{\rho}(t)\}\right)\right)$$

Consider a two-level system with the following:

$$\hat{\rho} = \begin{pmatrix}1 & 0\\ 0 & 0\end{pmatrix}, \qquad \hat{H} = \begin{pmatrix}0 & 1\\ 1 & 0\end{pmatrix}, \qquad \hat{L} = \begin{pmatrix}0 & 1\\ 0 & 0\end{pmatrix}, \qquad \Delta t = 0.1.$$

Now we calculate the $\hat{\rho}(t+\Delta t)$:

$$-\mathrm{i}[\hat{H},\hat{\rho}] = -\mathrm{i}\begin{pmatrix}0 & 1\\ 1 & 0\end{pmatrix}\begin{pmatrix}1 & 0\\ 0 & 0\end{pmatrix} + \mathrm{i}\begin{pmatrix}1 & 0\\ 0 & 0\end{pmatrix}\begin{pmatrix}0 & 1\\ 1 & 0\end{pmatrix} = \begin{pmatrix}0 & i\\ -\mathrm{i} & 0\end{pmatrix}$$

$$\hat{L}\hat{\rho}\hat{L}^\dagger = \begin{pmatrix}0 & 1\\ 0 & 0\end{pmatrix}\begin{pmatrix}1 & 0\\ 0 & 0\end{pmatrix}\begin{pmatrix}0 & 0\\ 1 & 0\end{pmatrix} = \begin{pmatrix}0 & 0\\ 0 & 0\end{pmatrix}$$

$$\frac{1}{2}\{\hat{L}^\dagger\hat{L},\hat{\rho}\} = \frac{1}{2}\left(\begin{pmatrix}1 & 0\\ 0 & 0\end{pmatrix}\begin{pmatrix}1 & 0\\ 0 & 0\end{pmatrix} + \begin{pmatrix}1 & 0\\ 0 & 0\end{pmatrix}\begin{pmatrix}1 & 0\\ 0 & 0\end{pmatrix}\right) = \frac{1}{2}\begin{pmatrix}1 & 0\\ 0 & 0\end{pmatrix}$$

$$\begin{aligned}\hat{\rho}(t+\Delta t) &= \begin{pmatrix}1 & 0\\ 0 & 0\end{pmatrix} + 0.1\left(\begin{pmatrix}0 & \mathrm{i}\\ -\mathrm{i} & 0\end{pmatrix} + \begin{pmatrix}0 & 0\\ 0 & 0\end{pmatrix} - \frac{1}{2}\begin{pmatrix}1 & 0\\ 0 & 0\end{pmatrix}\right)\\ &= \begin{pmatrix}0.95 & 0.1\mathrm{i}\\ -0.1\mathrm{i} & 0\end{pmatrix}\end{aligned}$$

To check if $\hat{\rho}(t+\Delta t)$ is positive semi-definite, we need to ensure that all its eigenvalues are non-negative. The eigenvalues of $\hat{\rho}(t+\Delta t) = \begin{pmatrix} 0.95 & 0.1\mathrm{i} \\ -0.1\mathrm{i} & 0 \end{pmatrix}$ can be calculated as:

$$\begin{vmatrix} 0.95-\lambda & 0.1\mathrm{i} \\ -0.1\mathrm{i} & -\lambda \end{vmatrix} = 0,$$

$$\lambda = \frac{1}{2}\left(0.95 \pm \sqrt{0.95^2 + 4 \times (-0.1\mathrm{i}) \times 0.1\mathrm{i}}\right),$$

$$\lambda_1 = 0.960, \qquad \lambda_2 = -0.010.$$

One of the eigenvalues is negative, meaning that $\hat{\hat{\rho}}(t+\Delta t$ is not positive semi-definite. We conclude that the Euler method does not preserve positive semi-definiteness.

B

Additional figures

B.1. Hubbard Model

Figures B.1 and B.2 visualise the application of all operators in a Hubbard model. Figure B.2 is an extension of figure B.1, including the operators associated with the SOC coupling.

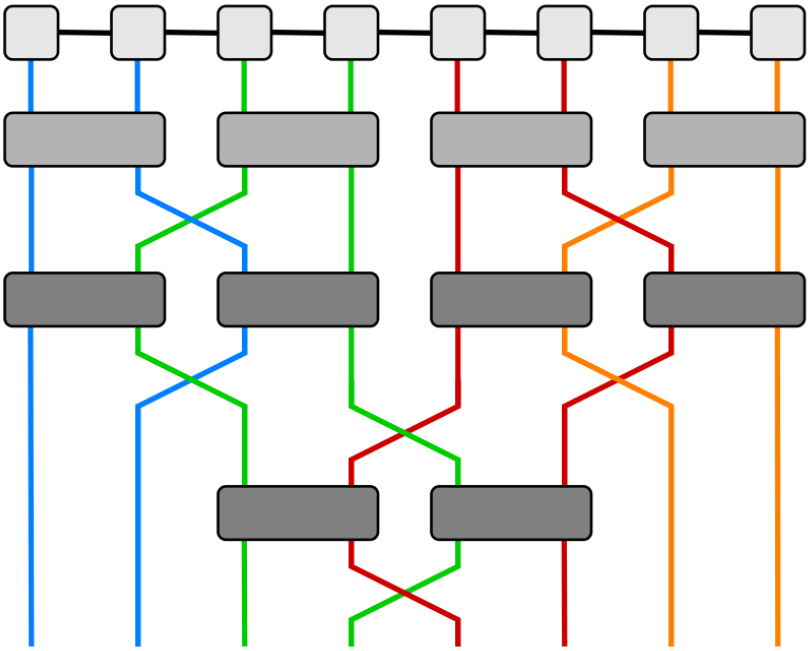

Figure B.1: The general Hubbard model for a quantum chain of length 4. Two lines of the same colour represent the up and down state at one site. The Coulomb interaction is light grey, and the hopping interaction is dark grey. From [1]. Reprinted with permission.

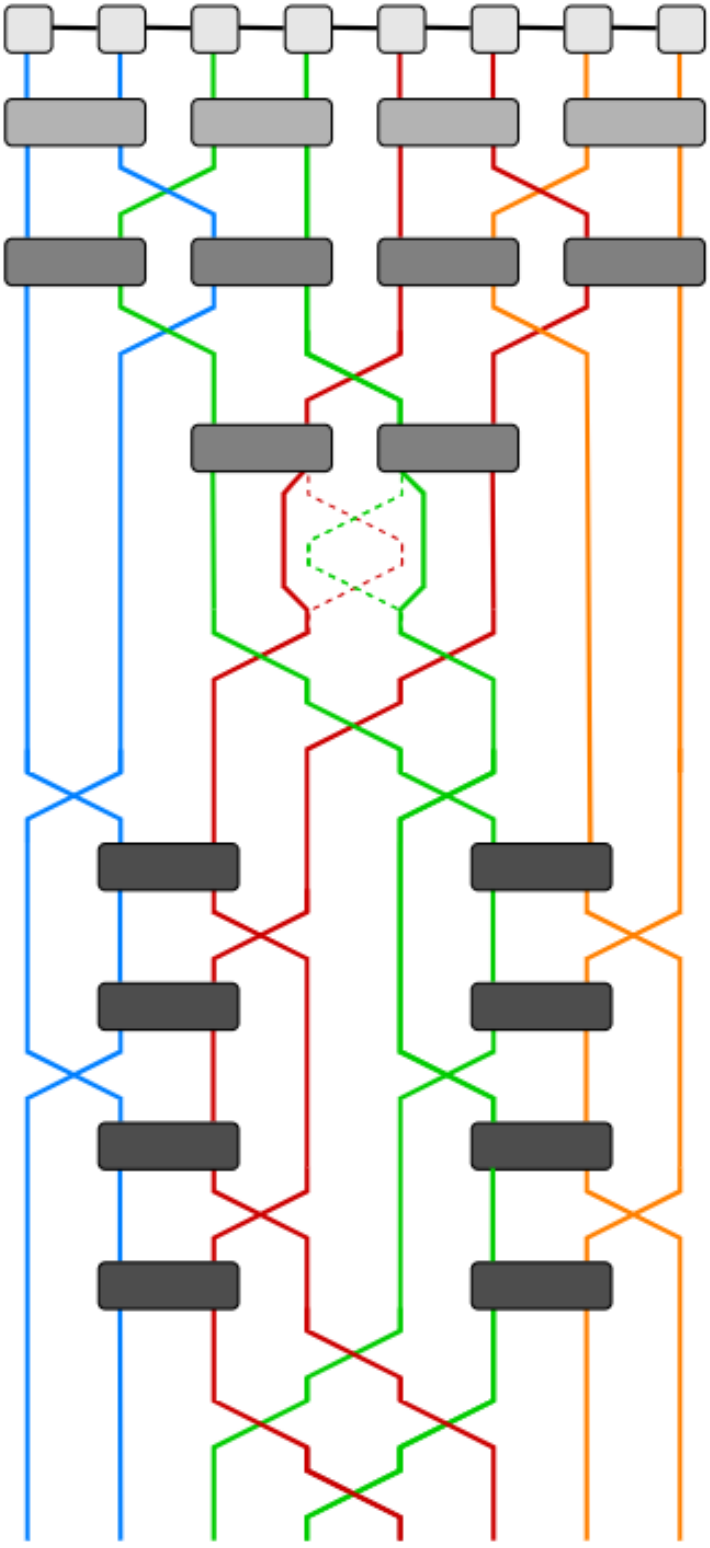

Figure B.2: The Hubbard model for a quantum chain of length 4 with spin-orbit coupling. Two lines of the same colour represent the up and down state at one site. The Coulomb interaction is light grey, the hopping interaction is dark grey, and the spin orbit coupling is black. From [1]. Reprinted with permission.

B.2. Simulation Results

We present extra figures of the simulations in addition to the results showed in chapter 5. Figure B.3 shows the result of the second-order Trotter approximation method with time step $\Delta t = 0.001$, instead of $\Delta t = 0.02$. Figures B.4 and B.5 show the magnetisation profile for each site of the chain for the Trotter approximation. Figures B.6 and B.7 show the magnetisation profile for each site of the chain for the third-order high-dimensional midpoint method.

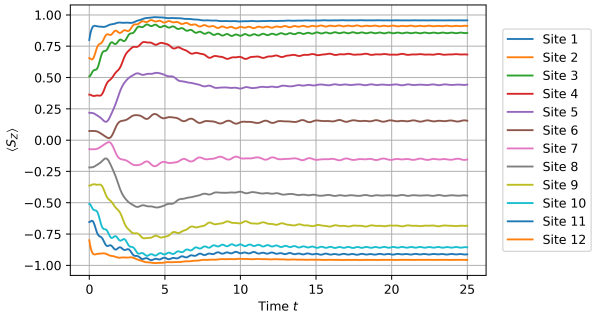

(a) $\langle \hat{S}_Z \rangle$ for each site over time.

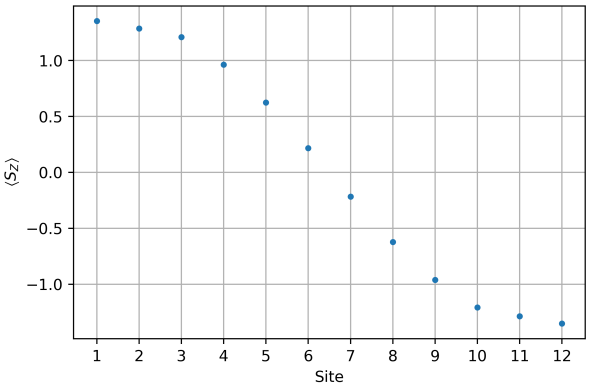

(b) $\langle \hat{S}_Z \rangle$ for each site at $t = 25$.

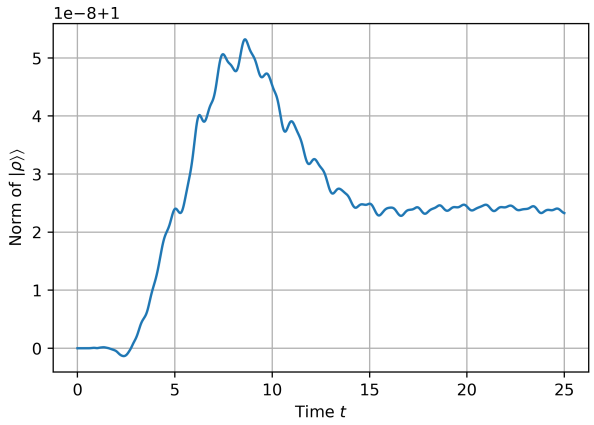

(c) The norm of $|\hat{\rho}\rangle\rangle$ over time.

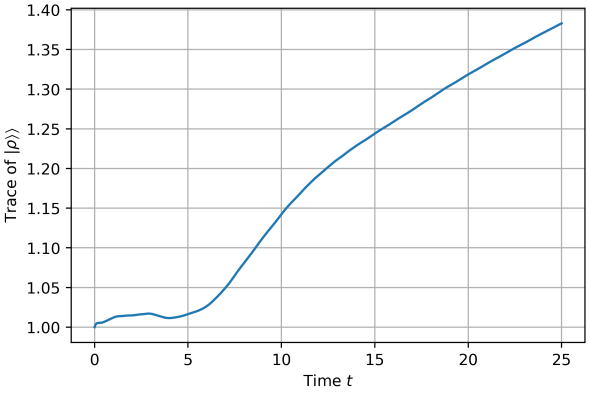

(d) The trace of $|\hat{\rho}\rangle\rangle$ over time.

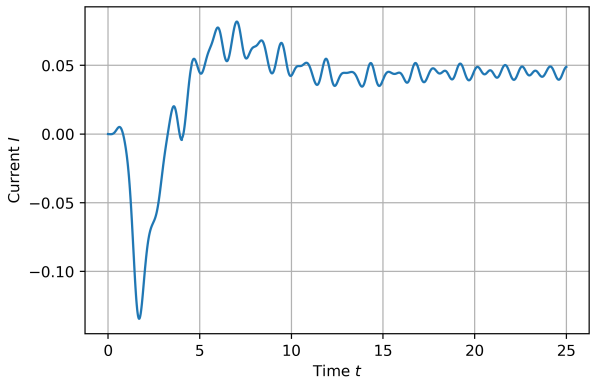

(e) The current through the chain over time.

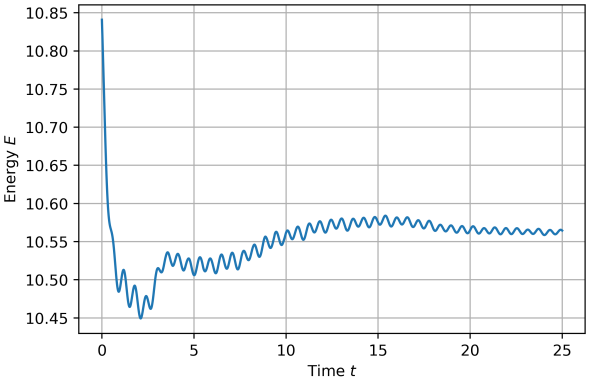

(f) The energy of the chain over time.

Figure B.3: Simulation of the XXZ-Heisenberg chain ($L = 12$, $\Delta t = 0.001$, $\chi = 15$, $\Delta = 1$)

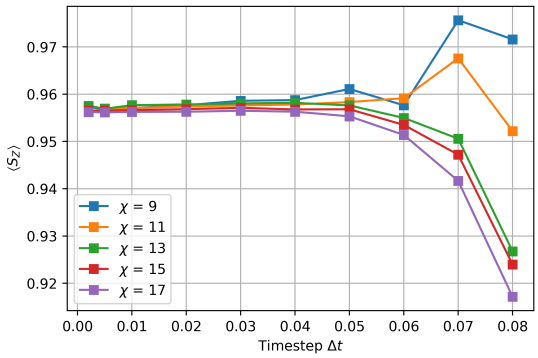

(a) Site 1 (and 12)

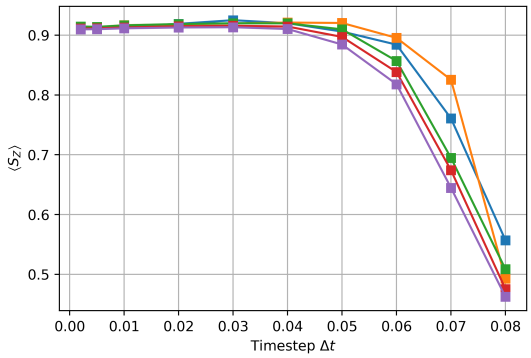

(b) Site 2 (and 11)

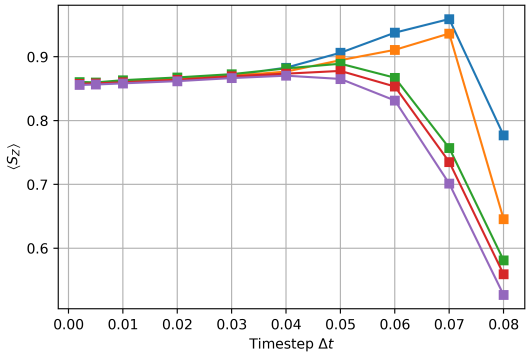

(c) Site 3 (and 10)

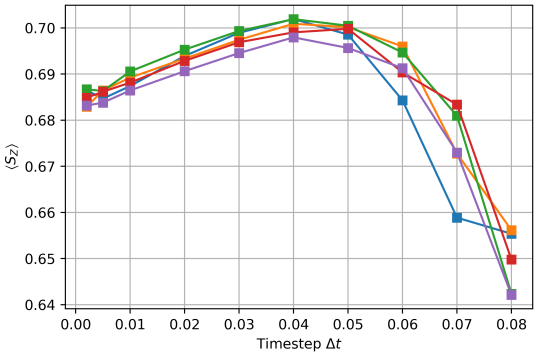

(d) Site 4 (and 9)

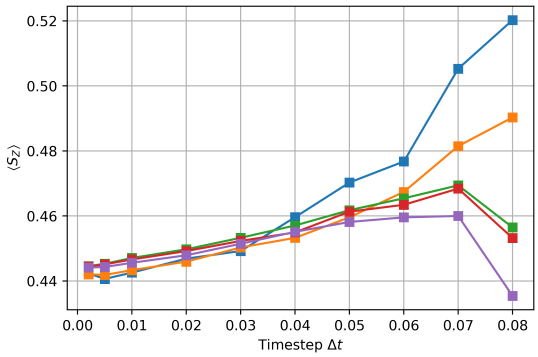

(e) Site 5 (and 8)

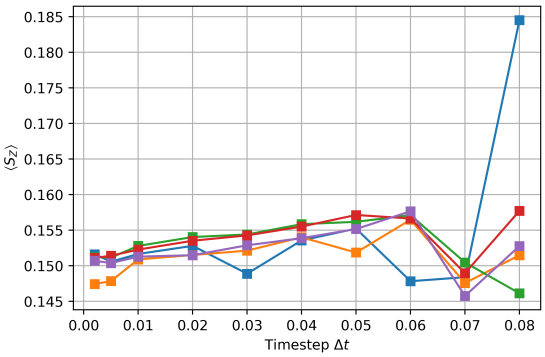

(f) Site 6 (and 7)

Figure B.4: The expectation values of S_Z at sites 1 through 6 as a function of Δt for different χ for the second-order Trotter approximation. The expectation values for the sites 7 through 12 are analogous, but negative, as the solution is symmetric, see 5.1a. ($L = 12$, $\Delta = 1$)

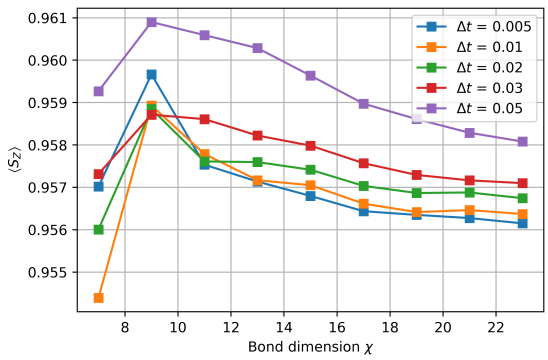

(a) Site 1 (and 12)

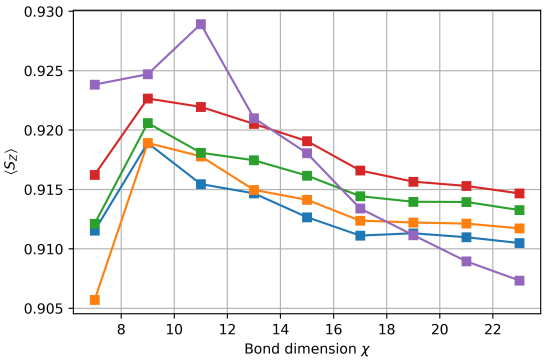

(b) Site 2 (and 11)

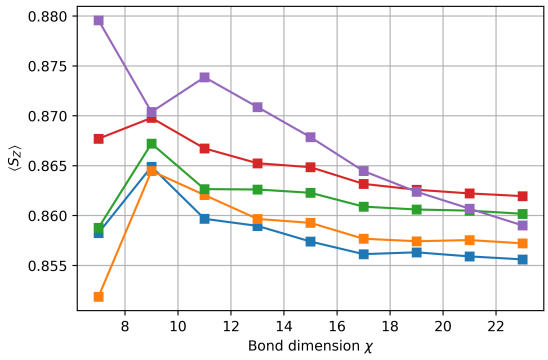

(c) Site 3 (and 10)

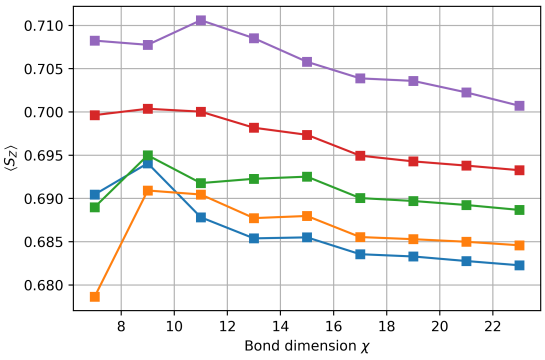

(d) Site 4 (and 9)

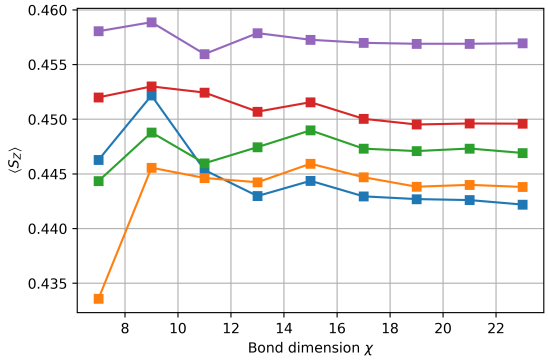

(e) Site 5 (and 8)

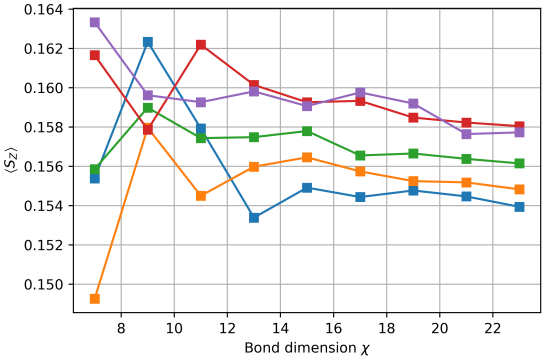

(f) Site 6 (and 7)

Figure B.5: The expectation values of S_Z at sites 1 through 6 as a function of χ for different Δt for the second-order Trotter approximation. The expectation values for the sites 7 through 12 are analogous, but negative. ($L = 12$, $\Delta = 1$)

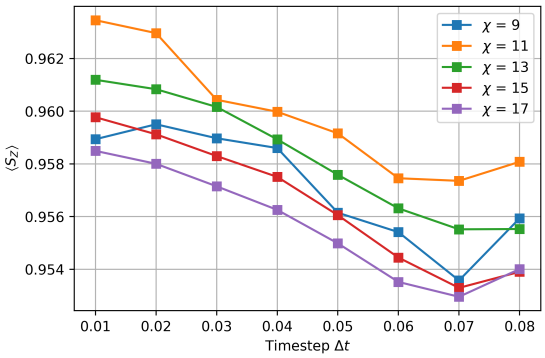

(a) Site 1 (and 12)

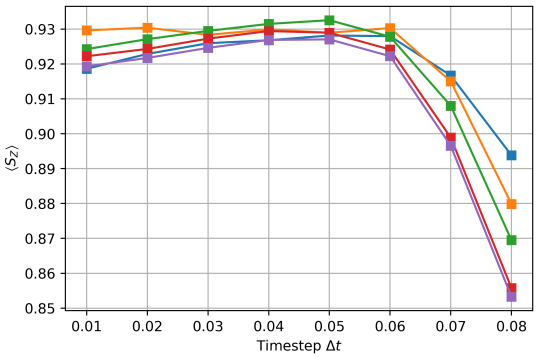

(b) Site 2 (and 11)

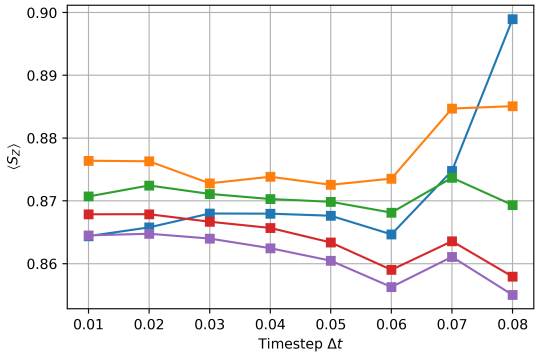

(c) Site 3 (and 10)

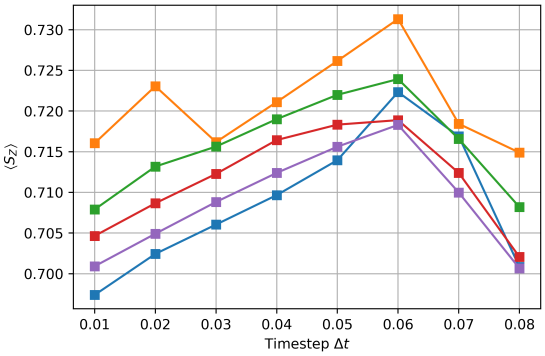

(d) Site 4 (and 9)

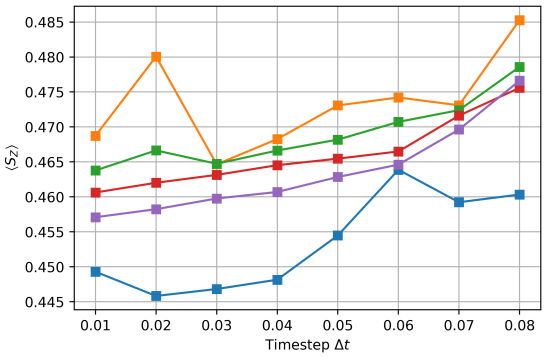

(e) Site 5 (and 8)

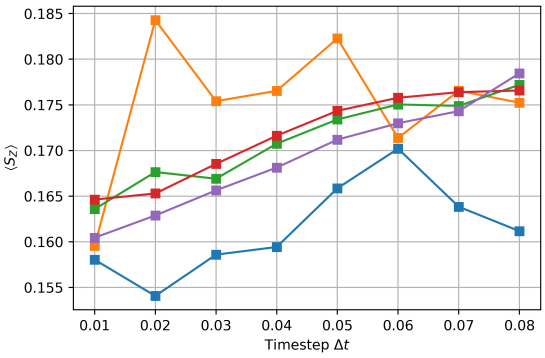

(f) Site 6 (and 7)

Figure B.6: The expectation values of S_Z at sites 1 through 6 as a function of Δt for different χ for the third-order high-dimensional midpoint method. The expectation values for the sites 7 through 12 are analogous, but negative, as the solution is symmetric, see 5.9a. ($L = 12$, $\Delta = 1$)

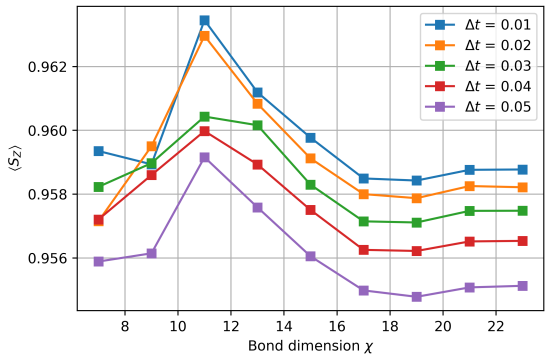

(a) Site 1 (and 12)

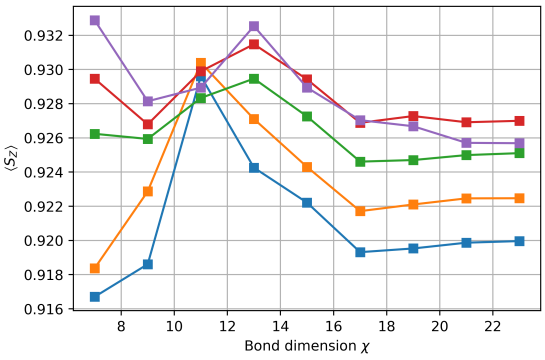

(b) Site 2 (and 11)

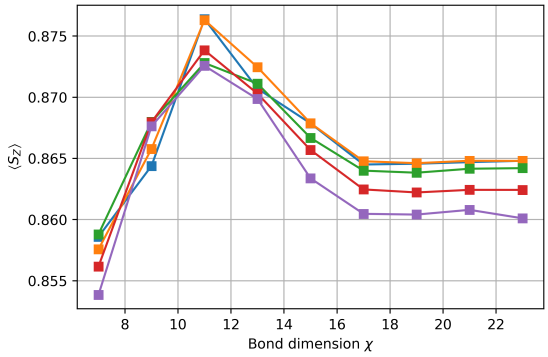

(c) Site 3 (and 10)

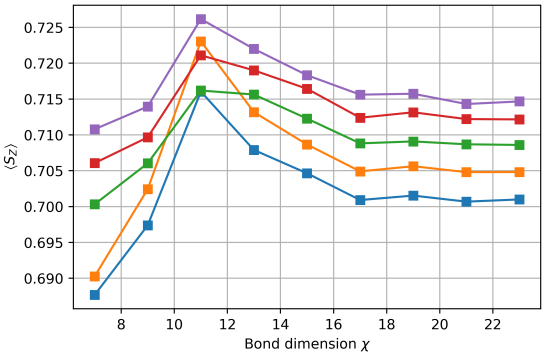

(d) Site 4 (and 9)

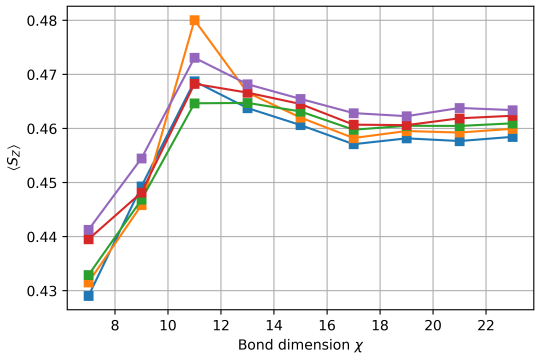

(e) Site 5 (and 8)

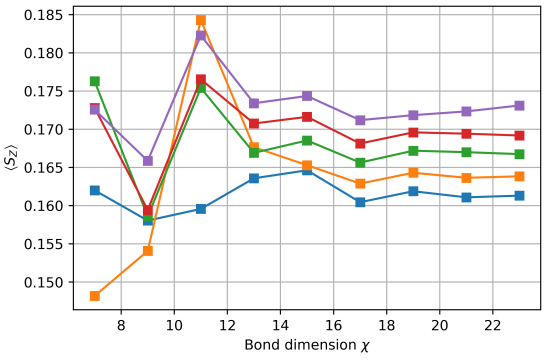

(f) Site 6 (and 7)

Figure B.7: The expectation values of S_Z at sites 1 through 6 as a function of χ for different Δt for the third-order high-dimensional midpoint method. The expectation values for the sites 7 through 12 are analogous, but negative. ($L = 12$, $\Delta = 1$)